TOWARDS a STRONTIUM BASED STATIONARY OPTICAL LATTICE CLOCK

by

QASIM HASSAN UBAID

A thesis submitted to
the University of Birmingham
for the degree of
Doctor of Philosophy

Ultracold Atoms Group
School of Physics and Astronomy
College of Engineering and Physical Sciences
University of Birmingham

September 2018

Abstract

Optical atomic clocks have proven to be the most stable clocks with the lowest systematic uncertainty which has now reached a record level of $(9 \cdot 4 \times 10^{-19})$. Thus optical clocks now surpass the best fountain Cs atomic clocks by three orders of magnitude which opens the prospect of using optical clocks as frequency standards for timekeeping in the near future.

This thesis describes the progress that has been made towards a stationary optical lattice clock based on strontium atoms, and reports the results of an ongoing characterization.

An experimental apparatus was designed and built to efficiently slow, cool, and trap the strontium atoms which represent the heart of the strontium optical lattice clock discussed in this thesis. The novel aspects of the experimental development described in the thesis comprise a frequency doubling cavity for producing 461 nm laser light employed for cooling and trapping the strontium atoms in the first stage cooling. This cavity provided sufficient power for cooling and trapping the strontium atoms for up to 300 mW of 461 nm laser light. Furthermore, a new design of Zeeman slower based on spherical permanent magnets was produced, built and characterized. The slower is compact, tunable, easy to assemble and maintain, and cost-effective as the permanent magnets do not require any power supply or water cooling. It is suggested that this kind of Zeeman slower constitutes an ideal solution for portable optical clock systems. A blue magneto-optical trap was realized for the first time with such a Zeeman slower. With about 30 mW of a 461 nm laser, up to 6×10^8 atoms were captured.

Acknowledgments

First and foremost I would like to express my thanks and appreciation to the Higher Committee for Education Development/office of prime minister/Iraq for offering me the scholarship and for the financial support. Secondly, I would like to thank my supervisor Prof. Dr. Kai Bongs for giving me the opportunity to work with such an amazing group, and for his professional supervision. I would like to express my thanks to my Co-Supervisor: Dr. Yeshpal Singh for his guidance through my study. I would like also to thank: Dr.Ole Kock and Dr. Joshua Hughes for introducing me to the field, Dr. Markus Gellesch, Dr. David Morris, Dr. Jonathan Jones, Dr. Yogeshwar Kale, Dr. Alok Singh, and Dr. Shengnan Zhang for proofreading this thesis. Of course, I would express my thanks, for all my lab. mates: Marco Menchetti, Wei He, Sruthi Viswam, Jonathan Bass thank you all for building a collaborative team. My thanks extend to all Cold Atoms Group. For the great work, they provided I wish to thank Steve Brooks and the workshop team. I would like to thank my family especially my brothers and my sister for their support. I would like to thank my wife for head and time free to pursue my Ph.D. study. Finally, my endless gratitude to my mother for her encouragement, love, and prayer.

Contents

List of Figures

List of Tables

Chapter 1

Introduction to Optical Atomic Clocks

The International System of Units (SI) has seven base units, the fundamental units of physics: ampere, candela, kelvin, kilogram, metre, mole and second, in terms of which all physical quantities can be expressed. The measurement of time, is of great importance to the SI system since several of the basic units (such as kilogram and ampere) are, today, expressed in terms of the second. The accuracy of the measurement of time as measured by atomic clocks is, today, about one part in 10^{16}. However, atomic clocks, based on microwave transitions are nearing the limit of their accuracy, and new developments based on optical transitions with higher operating frequencies have made it possible to measure the second with an even higher accuracy; one in 10^{18} [13, 14].

Initially time was related to the duration of the day, and at the International Meridian Conference held in Washington, USA, in 1884, the second was defined as 1/86400 of the mean solar day. But with the earth's rotation slowing down due to tidal friction, the unit of time changes slightly with each passing year. Although

mechanical devices were of increasing accuracy; pendulum oscillations, quartz clocks, and so on, they were all calibrated against the earths period of rotation.

In 1955 the UK National Physical Laboratory established the first practical caesium atomic clock and time measurement shifted from the astronomical second to atomic time. In 1967, the General Conference on Weights and Measures defined the second in terms of the transition between the two hyperfine levels of the ground state of the caesium-133 atom.

The measurement of time has played an essential part in human development, with the development of clocks over centuries always corresponding to the level of science and technology. However, what is a clock? A clock is a machine that measures time. In its purest form, it consists of two main parts as illustrated in Figure 1.1:

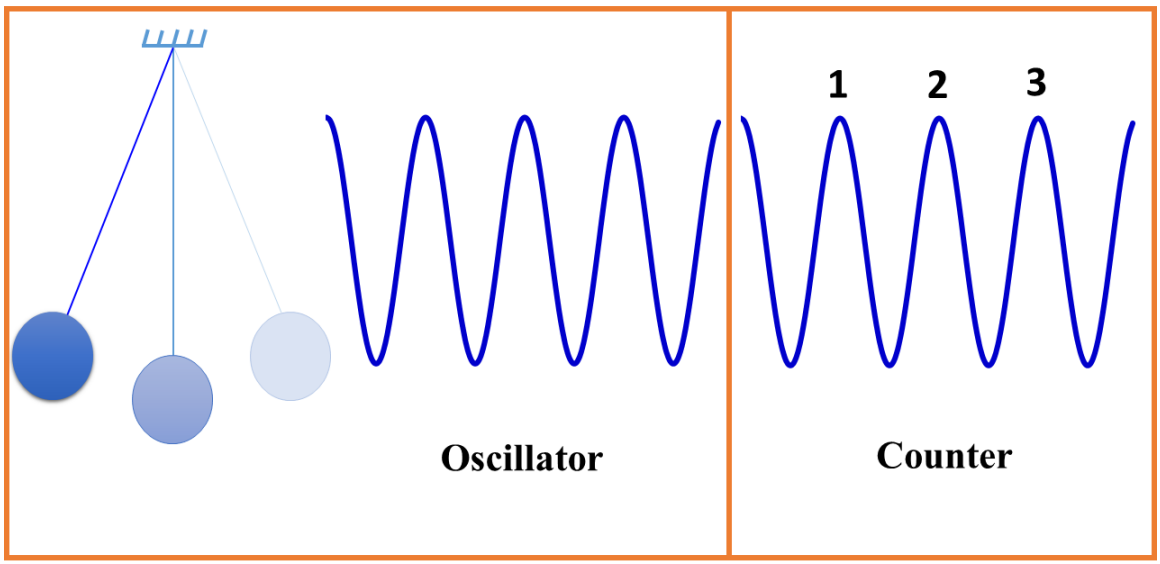

Figure 1.1: The concept work of a clock. The clock in its pure form consists of two main parts: Oscillator: phenomena that repeat itself with the same duration of periods in a regular way and a counter to measure these oscillations.

Oscillator: any physical phenomena that repeat itself periodically can be used to

measure time. It could be a pendulum in a clock, an electric oscillator in a watch, a computer or phone, or a laser in an optical atomic clock. The important thing for the oscillator is to mark the time required to complete each cycle, t_{cycle}.

Counter: the part of the clock responsible for tracking the measured "clock time" by counting the number of cycles N that have been completed and convert them to minutes and hours according to $t_{clock} = N.t_{cycle}$ [15].

In addition to the oscillator and counter, there is another part which is very useful for the performance of the clock: it is the frequency reference. This is used to check the accuracy of the clock and ensure it does not "drift" over time.

1.1 Brief History of Time keeping

Timekeeping history goes back to the beginning of humanity's existence. The change in seasons caused by the rotation of the earth around the sun is the basis on which our ancestors counted years. The spinning of the earth on its axis is the measure of a day, and even today many people feel intrinsically, that the position of the sun in the sky tells us what the time is. The movement of the moon around the earth is another example of how ancient people measured time. They observed the full moon phase and used that to count the synodic months (more usually referred to as lunar months) that have, on average, 29.5 days. For thousands of years the celestial bodies were used to tell time, and that heritage continued in the definition chosen for the second by the General Conference on Weights and measures in 1967 [16].

The impact of technology on social behaviour meant that people needed to measure increasingly shorter time intervals. First, they observed the shadow of a stick or wall, the position of which depended on the location of the sun in the sky. By linking

the position of the shadow to different parts of the day, the first sundial clock was invented [17]. Sundial clocks can measure in hours but are not suitable to measures time intervals shorter than that. An obvious failing of sundials is that they are not accessible during the night nor on cloudy days.

For these reasons, and because of the growth of trade and commerce, other types of chronometers were invented. Water clocks, for example, meant that time measurement was independent of the sun or other celestial bodies. These clocks work by the observation of how long it takes for a cistern to be filled or how long it takes for a cistern to be emptied, and could be calibrated using a sundial. This clock was invented to work during the night, so that, for example, participants could be woken for a religious ceremony, or it could be used to determine the time allowed for a presentation or duration of a debate in court.

Water clocks were improved by adding a means of determining the water level - a sight glass, say - and that allowed one to measure time [18]. More sophisticated mechanisms allowed shorter lengths of time to be measured. For example, the addition of mechanical parts to a water clock so that when the water filled cup-shaped device, the device tipped and pushed a lever which, in turn moved a geared wheel to show the time. (earliest water clock was over 3,000 years ago in Egypt or Mesopotamia) The major drawback was non-constant flow rates.

There were many developments of the water clock, such as replacing the water with fine sand, leading to a sandglass (also known as an hourglass) clock which was more compact, easier to use and was suitable for use on ships, and which allowed the captain to determine his longitude with reasonable accuracy [19].

The hourglass was replaced by mechanical clocks with a better periodicity in its oscillator, which meant an increase in precision. A movement that demonstrated much

greater precision was the pendulum clock, first demonstrated by Christiaan Huygens in 1656 A.D. The period of the pendulum, T, is the time it takes to complete one cycle, for the pendulum to swing from one point and return to the same point, $T \sim (l/g)^{1/2}$, where l is the length of the pendulum and g is the acceleration due to gravity at the point of operation of the pendulum. Compensation mechanisms have been developed to avoid the effects of temperature and humidity on the pendulum; and by the end of the nineteenth century the Siegmund Riefler clock achieved an accuracy of a 1×10^{-2} seconds a day [20].

Navigation has always driven the need for better clocks, in order to obtain more precision in determining longitude to prevent the loss of ships. In the 18th centenary, the British government announced a prize for solving the problem. True, the pendulum clock was sufficiently accurate but unfortunately, it cannot operate satisfactorily at sea because it requires to be static to work satisfactorily. After 50 years of development, John Harrison produced a clock which could hold time with an error of 0.2 seconds per day based on a "balance-spring" mechanism.

In the 1920s the pendulum clocks were succeeded by quartz crystal oscillators, which were based on the phenomenon of piezoelectricity discovered by P Curie in 1880 [21]. If you apply an electric field to a quartz crystal, the crystal changes shape. Similarly, if a quartz crystal is subject to pressure or a bending moment it will generate an electric field. By suitably arrangement of mechanical and electrical forces, the crystal can be made to vibrate at a resonant frequency which remains more or less constant and used to operate an electronic clock display. The invention of the quartz crystal clock by the American scientist Warren A Marrison in 1929 immediately brought an improvement in time measurement by an order of magnitude.

Most commonly, crystals resonate at about 32768 Hz, which corresponds to 2^{15} Hz.

This number is convenient since the signal at this frequency can be simply divided using binary frequency dividers down to 1 Hz. The magnitude of the frequency is a trade-off between optimizing the size of the crystal, and the power consumption of the accompanying resonant electronic circuit.

Quartz clocks have no mechanical gears or escapements to disrupt the frequency of operation, but even so, they remain reliant on mechanical vibration, the frequency of which is critically dependent on the exact dimensions of the crystal and its temperature. Thus, no two crystals can produce precisely the same frequency. Today, the timekeeping of quartz clocks has been bettered by atomic clocks both in absolute accuracy and in their synchronicity with similar clocks.

1.2 Atomic Clock

The revolutionary discovery of quantum mechanics in the last century opened a new era in physics, and has led to the possibility of a new type of oscillator. These oscillators are atoms and molecules and have the property of being much more accurate and precise oscillators than with all previously known references such as celestial bodies and mechanical devices. [22].

According to quantum theory, electrons in an atom occupy quantized energy levels. They cannot make a transition between two different energy levels E_1 and E_2 unless they absorb or emit energy equal to the difference in energy between the two levels in the form of electromagnetic radiation with precise frequency ν_o:

$$\nu_o = \frac{E_2 - E_1}{h}. \tag{1.1}$$

Where h is Planck's constant.

If the energy levels in an atomic system are insensitive to perturbation from ex-

ternal sources, then the natural frequency, ν_o, for a particular transition can be used as a reference for another laboratory generated radiation with stabilized frequency, ν, and compared against the natural frequency. With the addition of a counter to keep track of the stabilized oscillator, the structure of the atomic clock is completed as can be seen in Figure 1.2

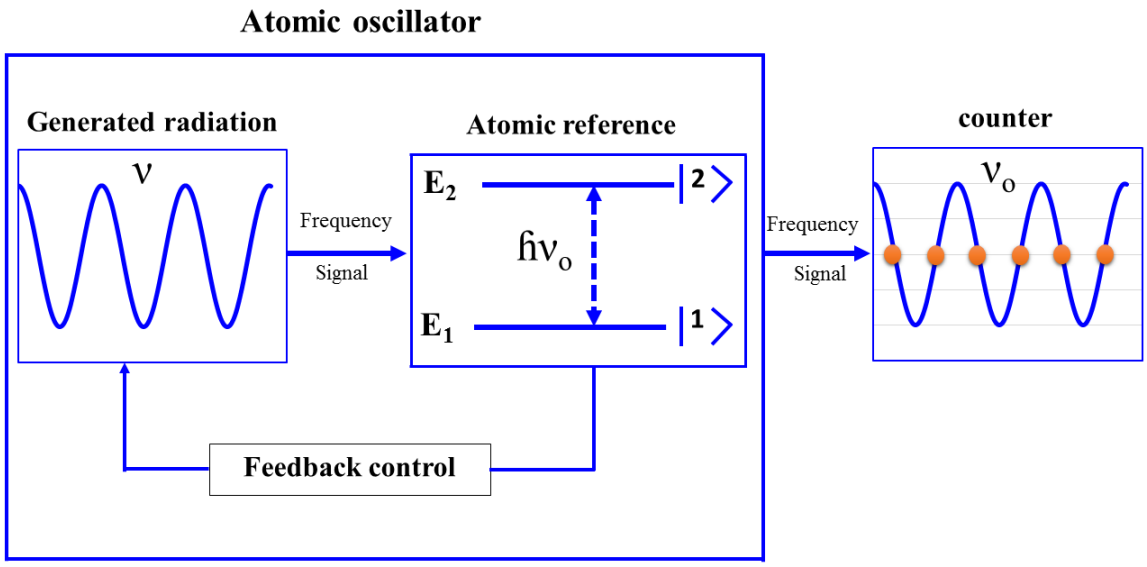

Figure 1.2: Schematic of the mechanism of an atomic clock. The frequency of an oscillator (laboratory generated), ν, is compared to the frequency of an atomic reference, ν_o. The difference in frequency between the two is used to correct the fluctuation in the oscillator frequency through a feedback loop, locking the frequency of the radiation source to the atomic transition frequency. By counting the numbers of oscillations, we can "tell the time".

One of the crucial advantages of using atoms is that the frequency reference is reproducible. As all ^{133}Cs atoms (for instance) are identical, they maintain the same properties and, in principle, two completely independent atomic clocks can give the same measurements of time if they use the same species of atoms - without the need for calibration. This is in contrast with other references such as pendulums or quartz

crystals, which cannot be replicated precisely, and will be affected by both their position on the globe and their age. In conclusion, if a particular atom was defined and its clock transition was also defined, this clock transition can work as a frequency standard.

With this in mind, the second was defined in 1967 in the International System of Units (SI) based on the ^{133}Cs atomic clock as follow:

"the duration of 9,192,631,770 periods of the radiation corresponding to the transition between the two hyperfine levels of the ground state of the caesium 133 atom [16].

However, in reality, the atomic frequency resonance ν_o is affected by external perturbations such as Doppler, Zeeman, Starck and collisional shift. In such cases, the atomic clock can accumulate errors in its ticking rate, either by increasing or decreasing the measured time intervals relative to the actual value.Therefore, when defining the second it must be understood that the atomic resonance ν_o is free from any external perturbations. This requires isolating the ^{133}Cs atoms completely from their environment with zero velocity (no Doppler or recoil shift). This velocity corresponds to the ideal condition of absolute zero temperature.

In reality, because the atoms cannot be entirely isolated from external perturbations, the perturbations have to be measured separately and characterized so that one can estimate the total systematic frequency offset ϵ. This can be used to compensate for these perturbations which ultimately enables restoring the accuracy of the atomic clock. However, some residual uncertainty in the estimation will remain and cannot be compensated for, leading to timing errors. Moreover, the oscillator frequency, ν will not match the resonance frequency of the atoms ν_o perfectly. As a result, the clock can acquire time-dependent frequency instability $y(t)$, the average of which can trend towards zero for long-term measurements. But it can lead to errors in short-

term measurements. Adding all these effects together, the frequency of the clock can be written as [10] :

$$\nu(t) = \nu_o(1 + \epsilon + y(t)). \tag{1.2}$$

From Equation 1.2 it can be seen that two quantities characterize the atomic clock performance:

- **The relative systematic uncertainty**: sometimes referred to as the relative (in)accuracy of an atomic clock. It characterizes how well the measured frequency compared with the ideal frequency. Generally speaking, the accuracy of an atomic clock depends on how well the atoms have been isolated from perturbations during their interrogation by the clock laser and detection of their frequency (systematic errors).

- **The instability**: it represents the statistical noise from operation of the clock, which related to the averaging time, τ, necessary to give the frequency measurements a certain level of precision. The higher the precision required, the longer the averaging time, e.g. the longer the averaging time the smaller the value of the statistical fluctuation $y(t)$ [23]. The instability is typically given in terms of fractional frequency instability, which is limited by quantum projection noise (see section 1.3).

Besides instability and uncertainty, characterizing the performance of an atomic clock requires a third quantity: the absolute uncertainty or absolute (in)accuracy. The frequency comparison has to be relative to an ideal ^{133}Cs clock (the present frequency standard). If a Cs clock is used its absolute frequency and systematic frequency are the same, but atomic clocks based on other atomic species have to be compared to

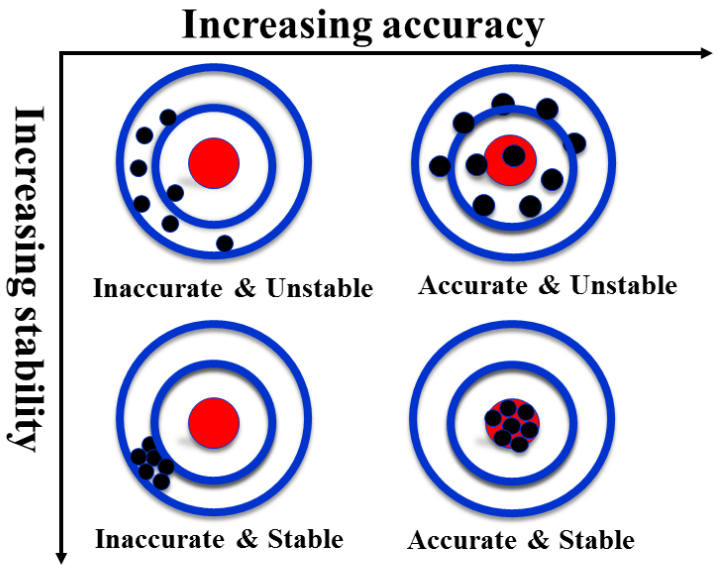

Figure 1.3: The performance of atomic clocks can be characterized by two quantities: accuracy and stability. In general, accuracy represents how close the measured frequency, ν , is to the fundamental frequency of the atomic species, ν_o; The measured frequency can be determined by summing all the parameters that cause the frequency to shift from its natural (real) value. Stability, refers to the ability to obtain the same or similar results when repeating the same measurement. It represents the noise in the measurements; a measure of stability can be determined by how long it takes to average out the statistical fluctuation. From the Figure, one can see that, accurate measurements are stable over a long time, whereas, a stable measurement is not necessarily accurate.

an ideal ^{133}Cs clock and this can introduce relative uncertainty.

The significant development in electronics that has happened since the middle of the last century resulted in the first measured frequency of atomic transition based on nitrogen inversion in ammonia molecules, [24] which lies in the microwave region of the electromagnetic spectrum. However, as the accuracy was in the same order of magnitude as astronomical measurements it was not accepted as a standard. In 1955, L. Essen and J. V. Parry from the UK National Physical Laboratory (NPL),

demonstrated the first atomic clock based on ^{133}Cs [25], that had an accuracy that was better than the astronomical reference by two orders of magnitude. Caesium was selected because it has many useful properties that make it suitable to work as a frequency reference. Cesium is considered a relatively heavy element with 133 atomic mass units (amu), which means it moves with a speed ≈ 130 m/s at room temperature compared with ≈ 1600 m/s for the hydrogen, for instance. Thus, Cs atoms will spend more time interacting with the microwave field in the interrogation region compared with hydrogen. Moreover, the hyperfine transition in Cs is relatively high ≈ 9.2 GHz compared with ≈ 6.8 GHz for the rubidium.

The initial uncertainty of this atomic clock was 10^{-10} when invented. During the last 50 years, the level of uncertainty has been improved significantly, decreasing by roughly one order of magnitude every ten years to reach a current value of $\sim 2\times10^{-16}$ [26–28].

1.3 Optical Atomic Clocks

Conventional atomic clocks have already achieved a high level of both accuracy and stability. The question is, why there is a need to develop optical atomic clocks. One reason given is the quantum projection noise (QPN) limit, which is considered a fundamental limit for all atomic clocks [29, 30]. Even when the frequency of the clock laser (ν) and the frequency of the atomic resonance (ν_o) are precisely identical, quantum projection noise still exists because of the superposition between the ground and excited states of atoms. The QPN leads to fluctuations in the clock measurements which, in turn, affect the stability of the atomic clock, typically given in terms of fractional frequency instability. Therefore, to increase the stability of the atomic

clock, one needs to reduce the value of the quantum projection noise. The QPN value for a particular atomic transition can be estimated by [31] :

$$\sigma_y(\tau) \approx \frac{1}{Q}\frac{\sqrt{T_{cyc}}}{\sqrt{N_{atoms}}\sqrt{\tau}}. \tag{1.3}$$

Where Q is the quality factor of a transition, T_{cyc} is the time of one clock cycle, N_{atoms} is the number of interrogated atoms and τ is the time required for averaging data. The quality factor of a transition is given by :

$$Q = \frac{\nu_o}{\Delta\nu}. \tag{1.4}$$

Where ν_o is the natural frequency of the atomic transition and $\Delta\nu$ is the observed linewidth of that transition.

The importance of the quality factor comes from the fact that the atoms cannot absorb or emit electromagnetic radiation of given frequencies unless these frequencies are within the linewidth of the transition. Therefore, atoms with high-frequency transition and narrow linewidth are preferred. Moving from the microwave to optical transitions can decrease the value of the QPN because the quality factor for optical transitions is higher by more than 10^4, compared with the microwave transitions. That can increase the stability of the clock by the same order of magnitude if all the other parameters do not change. It can be compared to using a ruler to measure a length. A ruler with centimeter divisions can measure the length with a precision of around half a centimeter; whereas a ruler with millimeter divisions can measure a length with a precision of around half a millimeter, a ten times higher resolution. The same analogy can apply when increasing the Quality factor for the clock transition. From Equation 1.3 one can see that QPN is inversely proportional to the square root of the number of interrogated atoms with clock laser and also the square root of the averaging time (QPN $\propto \frac{1}{\sqrt{N_{atoms}}\sqrt{\tau}}$). The optical atomic clocks also benefit from a high

number of atoms confined in the optical lattice. For 10,000 atoms, the QPN was found to be less than 10^{-17} for one second [32]. The greater number of atoms interrogated in the optical atomic clock compared to the atomic fountain clock reduced the QPN.

Although the idea of using optical transitions as a frequency standard has been around for some time, many essential technological developments were necessary for its realization as a clock. The first requirement were lasers capable to probing the atomic reference. The first laser was realized in 1960, five years after the first atomic clock. The second challenge was to reduce the Doppler effect to a sufficiently low level, which was achieved by cooling and trapping the atoms in 1987. The first suggestion to use lasers to cool atoms was proposed in the mid-70's by Hänsch and Schawlow [33], in order to produce an extremely accurate and stable clock. The final obstacle to an optical clock was the ability to count the oscillation of an optical frequency, some 10^5 times higher than the frequency of the microwave transition. One solution was to convert the frequency to the microwave region by using an optical frequency converter chain. The first measurements of the optical transition were carried out using the frequency chain, but it was a very complex and bulky technique, and not very reliable [34]. A much simpler and more reliable solution was presented in 1999-2000 when T. Hänsch invented the frequency comb [35]. With this invention it is now possible to measure the frequency with an accuracy some 10^6 times more precise than previous spectroscopic determinations. This has revolutionized the performance of optical atomic clocks, reducing their complexity and size by enabling direct measurement of optical transitions.

Optical atomic clocks are the latest generation of atomic clocks that utilize an optical transition to realize the frequency standard and have already outperformed the best microwave atomic clocks in their stability. The optical atomic clock consists

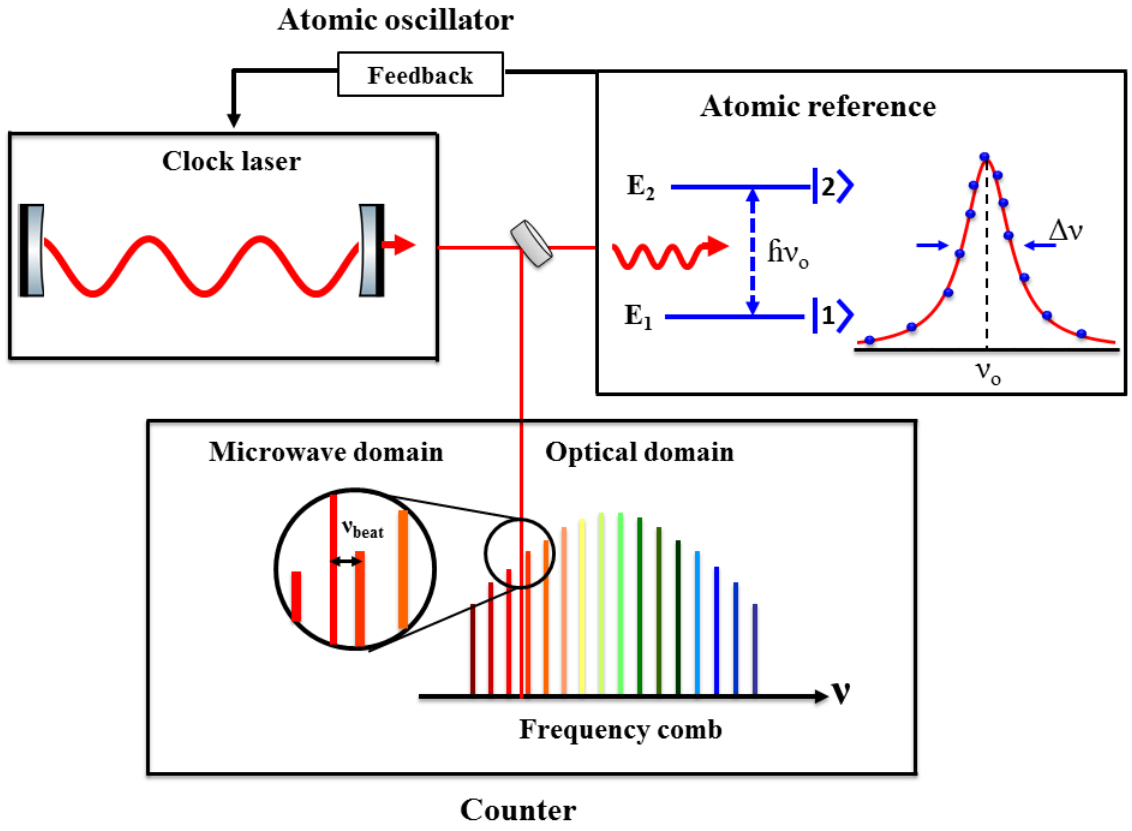

Figure 1.4: Architecture of an optical atomic clock. The panel on top left: an ultra-stable laser is locked to optical atomic transition so that the clock laser frequency follows the atomic transition frequency with the aid of electronic feedback. The panel on top right: the atomic reference transition has a high-quality factor. The bottom panel: to be readable the output clock laser frequency is converted to the microwave region by beating it with one tooth of a frequency comb teeth.

of three main parts as shown in Figure 1.4 : an ultra-stable laser, which serves as a local oscillator, an atomic species to be used as a reference and, an optical frequency comb that is used as a counter, or one can think of it as an "optical gear". After cooling the atoms, they are trapped in an optical lattice, then they are interrogated by a clock laser. The absorption signal is recorded by a detector and compared with the clock laser, and fluctuations in the laser corrected by using a servo loop. The optical frequency comb consist of a passively mode-locked laser that generates a train

of ultra-short pulses ($\sim 10^{-15}$ s) equally separated in time by the repetition rate of the laser $\tau = 1/f_{rep}$. The output of the comb in the frequency domain consists of a series of delta function "teeth" separated by the reputation rate frequency. The output frequency of the optical transition is converted to an electronically readable signal by taking the beat note between it and the nearest tooth in the comb. The first use for the optical frequency comb to measure an absolute optical frequency was in 2000 [36]. The optical frequency comb used to measure the output frequency for optical clocks relative to C_c and other optical clocks, as illustrated in Fig.1.5. The frequency comb has improved frequency standards by contributing to the rapid development, in accuracy and stability of atomic clocks, reaching a value of $\sim 2\times10^{-16}$, after which the Cs atomic fountain retired having reached its limit. However, two types of optical atomic clocks (single ion clocks and neutral atom in optical lattice clocks) continue, each one trying to outdo the other.

1.3.1 State-of-the-art Optical Atomic Clock

Optical atomic clocks can be classified according to the type of the interrogated particles: ions or neutral atoms. The optical atomic clocks that exploit ions were developed first. As ions are charged particles, it is relatively easy to control their motion, and hence they can be cooled and trapped efficiently with a minimal level of perturbations. The lifetime of the confined ion is usually long; and can reach several months. However, the strong interactions between ions limit the number of ions that can be contained in a trap; typically the trap will contain one or a few ions. According to Equation 1.3), this type of optical clock requires a relatively long time to reach a low level of fractional frequency instability. However, alone laser-cooled ion in a rf electromagnetic trap is considered to be close to the ideal of an environment which is

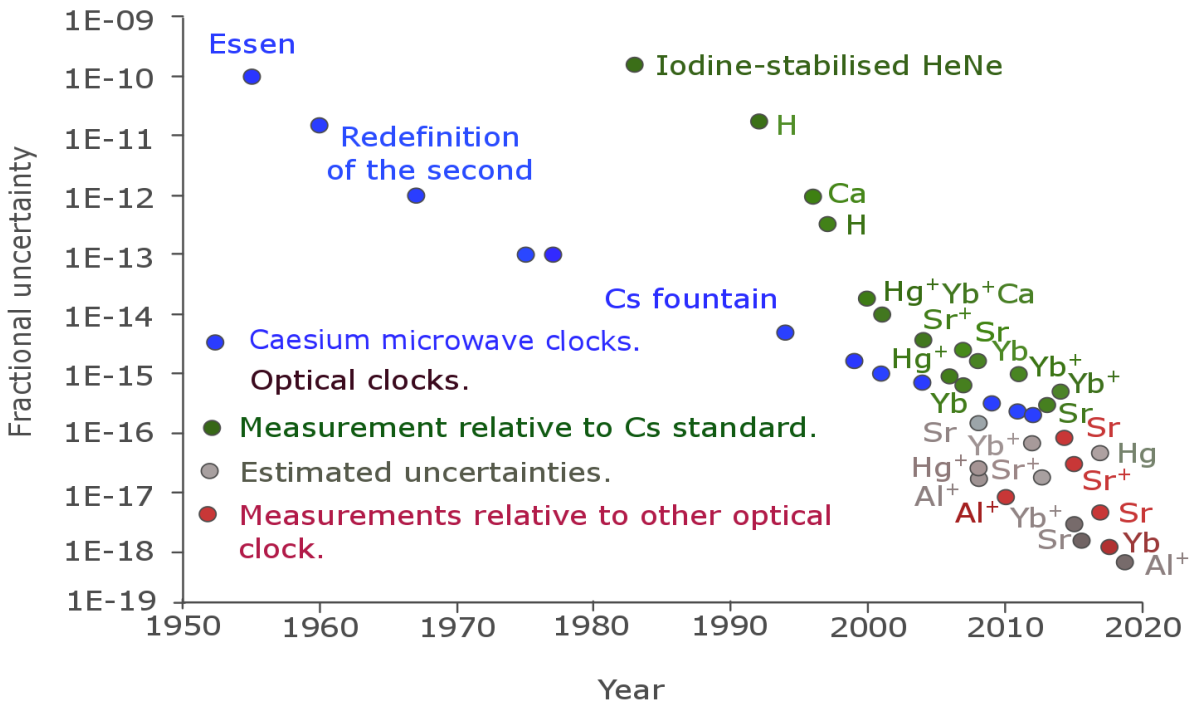

Figure 1.5: Illustration of the timeline for atomic clock development since they were invented in 1955. The new generation of optical atomic clocks (ions and optical lattice) are also presented, with their accuracy. As the Cs atomic clock still retains the definition of SI second, the accuracy of any clock has to be relative to the Cs clock. However, optical atomic clocks that have already surpassed the Cs standard, have their accuracy and stability compared to other optical atomic clocks [1, 2].

free of perturbations. Many ions optical clocks are being developed based on different atomic species: Al^+ [37], Ca^+ [38,39], Sr^+ [40,41], In^+ [42], Yb^+ [43–46], and Hg^+ [47]. The Yb^+ ion clock at Physikalisch-Technische Bundesanstalt (PTB), Germany was holding the best-reported systematic uncertainty of 3×10^{-18} [45] but very recently a new record have come in Al^+ with a systematic uncertainty of 9.4×10^{-19} [48].

On another hand, optical lattice clocks utilize large numbers of neutral atoms $\approx 10^3 - 10^6$ confined in a tight trap to be interrogated. In contrast to ions, the interaction between the neutral atoms is weak. Due to weak atom-light interaction, it becomes more difficult to trap such a large number of atoms. Interrogating such a

large number of atoms gives the opportunity to increase the stability of the optical lattice clocks.

Optical lattice clocks based on alkaline earth (-like) atoms are receiving significant attention because of their desirable atomic structure. They provide an allowed active transition that can be used for fast and efficient cooling. Also, they have intercombination transitions (transitions between singlet and triplet state forbidden by the selection rule) that can be used for further cooling, particularly the doubly forbidden ($^1S_0$-$^3P_0$) transition in the isotope that has nuclear spin. The ($^1S_0$-$^3P_0$) transition is crucial for clocks because it lies in the optical region of the spectrum, and its linewidth is very narrow.

One of the obstacles facing optical lattice clocks is the AC Stark shift which arises due to the interactions between an electric field of a laser and induced electric dipole on atoms. Katori proposed to trap strontium atoms in a light-shift trap to tackle the inhomogeneous AC Stark shift problem. Atoms confined in a "magic wavelength" [49, 50] can observe a semi-equal shift for both atomic states of the clock laser. Therefore, it is possible to measure the clock laser frequency in relatively unperturbed states.

Today, several optical lattice clocks are being developed worldwide, mostly based on Sr [51–56], Yb [57–61], and Hg [62, 63]. Strontium and ytterbium optical lattice clocks have reported total systematic uncertainty of 2.1×10^{-18} and 1.4×10^{-18} respectively [13, 14].

As the definition of the SI second still depends on the Cs atom, any clock has to be compared against the Cs atomic clock. That could cause a problem for the optical atomic clocks that have outperformed the best Cs atomic clock. The proposed solution to overcome this limit is to perform direct frequency comparisons between optical clocks. This approach allows the achievement of much higher stability: Sr

[64, 65], Al^+ [37]. Although many optical atomic clocks have been estimated to have uncertainty lower than the Cs fountain clock (indicated by the gray dots in Fig. 1.5) : Yb^+ [44, 45], Sr^+ [41], Al^+ [37], Sr [14, 65, 66] a few optical clocks were able to reproduce uncertainty below 10^{-16} (the red dots in Fig. 1.5) Sr^+ [67], Al^+ [68], Sr [14, 52, 58, 64].

1.3.2 Applications of Optical Atomic Clock

Probably one of the most common and well-known uses for the atomic clock is the Global Navigation Satellite System (GNSS). In the Global Positioning System (GPS) for example, 20 to 30 satellites orbit the earth, each satellite has an atomic clock on board, and all these clocks are synchronized with each other and with stationary clocks on Earth. The satellites transmit a signal containing information about their position and the time. The distance between the satellite and receiver can be determined by comparing the time between sending and receiving the signal. To fully determine the position of the receiver, information from four satellites is required. Improving the accuracy of the atomic clock by going to optical transitions could lead to determining the position more accurately.

By using sophisticated receivers, object position could be determined with accuracies of 1 cm [69]. This improvement will not just improve navigation, but will also help in such useful fields as geology and meteorology. Recently, the satellite signal was used for remote sensing of water vapor in the atmosphere [70, 71]. Accurate timing of signals could be used to synchronize electricity grids to reduce energy losses, or networks for mobile phones, computer networks used for trade and commerce.

Another application of optical atomic clocks is relativistic geodesy (sometimes called chronometric geodesy) [72, 73]. The theory of general relativity predicts that

time is affected by gravitational potential with a dilation in time. An optical clock with an accuracy in the 10^{-18} range, should be able to detect this effect. In this case, the precise measurement of differences in time can be implemented by using two optical clocks at different gravitational potentials.

Due to their high accuracy and stability, optical atomic clocks could be utilized to investigate the fundamentals of physics. For instance, one could measure the stability of fundamental constant, like an electron to proton mass ratio [37, 74], and the fine structure constants where some physicists suspect that the value of these constants may drift with time. According to this context, it is possible to utilize the optical clock to test the gravitational redshift of Einsteins equivalence principle [75] by sending an optical clock into space as suggested in the STE - QUEST project [76].

Finally, the progressive development in the performance of optical atomic clocks could lead to redefining the SI second. The Work Group of Frequency Standard (WGFS) have already recommended: secondary representations of the second that could realize the SI second in parallel to the Cs primary standard. According to WGFS recommendations, several existing optical transitions are appropriate as a frequency standard. In 2006, the first five representations were accepted officially by the International Committee for Weights and Measures (CIPM). Nine years later, the recommended list was updated to include more secondary representations of the second [77, 78].

1.4 Thesis Layout

In addition to this chapter, this thesis contains another five chapters. These are arranged as follows:

Chapter 2 **:** Introduces the basic theory of laser cooling and trapping of neutral atoms. It explains the use of strontium in optical lattice clocks.

Chapter 3 **:** Focuses on the experimental setup designed and constructed to produce the ultra-cold strontium atoms.

Chapter 4 **:** Is dedicated to describing the design, build, and characterization of a new type of Zeeman slower based on spherical permanent magnets.

Chapter 5 **:** Presents the built monolithic frequency doubling cavity to produce the 461 nm laser. The blue laser is crucial for the strontium optical lattice clock. It is used to slow, cool, and trap the strontium atoms in the first stage cooling. In addition it is used to probe the strontium atoms in the optical lattice.

Chapter 6 **:** Provides conclusions and recommendations for possible future work.

Chapter 2

Laser Cooling and Trapping of Neutral Atoms

Neutral atoms have the capability to be a frequency reference, but that depends on the ability to control both of their internal and external degrees of freedom; as well as the ability to access to their natural spectral features without causing any perturbation effect such as frequency shift and bandwidth broadening. The desired environment to make precision measurements requires a sample of atoms to be at rest in the laboratory reference frame which corresponds to the absolute temperature of the atomic sample reaching the zero kelvin limit. In turn, at Room temperature ($T \approx 300$ K) atoms move with a most probable speed v_0 given by:

$$v_o = \sqrt{\frac{2k_B T}{M}}. \tag{2.1}$$

Where k_B is the Boltzmann constant and M is the atomic mass. From Eq. 2.1 we can see that atoms moving with a given speed in the laboratory frame, which is equivalent to specifying the temperature of the atoms, can mean many undesirable effects : First of all, a sample of atoms that move towards an interrogation laser beam

sees the angular frequency ($\omega_o = 2\pi\nu_o$) of the laser field as blue shifted according to the Doppler effect, given by :

$$\omega = \omega_0 + \vec{k} \cdot \vec{v}, \tag{2.2}$$

where ω represents the measured angular frequency in the laboratory reference frame, $\vec{k}$ is the wave vector of the laser field, and $\vec{v}$ is the velocity of the moving atoms. Furthermore, atoms with velocity $\vec{v}$, that cross a laser beam probe with diameter d perpendicularly, can limit the atom-light interaction time τ which leads to transit - time broadening given by :

$$\Delta\nu_{tt} = \frac{1}{\tau} = \frac{v}{d}. \tag{2.3}$$

Thereby reducing the Quality factor of the transition ($Q = \nu_o/\Delta\nu$). Finally, a thermal gas of atoms with a specific temperature has a Maxwell - Boltzmann velocity distribution given by :

$$f(v)dv = \frac{1}{\sqrt{\pi}v_o} \exp(\frac{-v^2}{v_o^2})dv. \tag{2.4}$$

Where v_o is the most probable velocity, $f(v)dv$ indicates the proportion of atoms that have a velocity in the range v to $v+dv$. In the presence of an interrogation laser field, the frequency response from each velocity class of the thermal atoms will be given by the Doppler shift, Eq. 2.2. Therefore, the resultant total frequency response will form a Gaussian shape Doppler broadening (full width at half maximum) equal to :

$$\frac{\Delta\nu_D}{\nu_o} = 2\sqrt{\ln 2} \cdot \frac{v_o}{c}. \tag{2.5}$$

From the arguments above, we can see that cooling the atoms by reducing their motion close to "standing still" is a prerequisite for many reasons: First, access the natural line width of an atomic transition without causing any shifts or broadening. Secondly, to allow high quality factor spectroscopy; Finally, because the ultimate

goal of the experiment is to trap the atoms in a potential trap employing an optical lattice of depth $\sim 20\ \mu$K, it is essential to prepare the atoms by slowing them (in one dimension) then cooling them (in three dimensions).

Neutral atoms are insensitive to stationary electric fields. Thus they are difficult to manipulate. However, the rapid development in laser field technology has added an extra tool to control the motion of the atoms through atom-light interactions with two types of optical forces: a scattering force (dissipation) force and dipole trap (conservative) force [79, 80].

2.1 Dissipation (Scattering) Force

The dual nature of light enables it to exhibit both of particle and wave properties. A photon, has Energy $E = \hbar\omega$ and carries momentum, $\vec{P}_{ph} = \hbar\vec{k}$ where $\hbar$ is the reduced Plank's constant $(h/2\pi)$, $\omega = 2\pi\nu$ is the light angular frequency of the light wave, $\vec{k}$ is the light wave vector; $|\vec{k}| = k = 2\pi/\lambda$. Where λ and ν are the light wavelength and frequency respectively.

Let us assume a simplified structure of an atom consisting of just two levels: ground state $|g\rangle$ and excited state $|e\rangle$, and it has a momentum $(\vec{P}_{at} = m\vec{v})$, where m, $\vec{v}$ is the mass and velocity of the atom respectively. The atom can absorb a resonant photon with frequency ω_{abs}, which excites it from ground to excited state. Conservation of linear momentum dictates that the atom will receive a momentum impulse $\hbar\vec{k}$. Thus, momentum of the atom changes to $\vec{P}_{at} = m\vec{v} + \hbar\vec{k}$. After some time (during which the atom cannot absorb any photons) determined by the lifetime of the excited state, $\tau = 1/\Gamma$. Where $\Gamma = 2\pi\gamma$, and γ is the natural linewidth of the transition, the absorbed photon will be emitted either by stimulated or spontaneous emission. The

direction of the spontaneously emitted photon is totally random as illustrated in Fig. 2.1

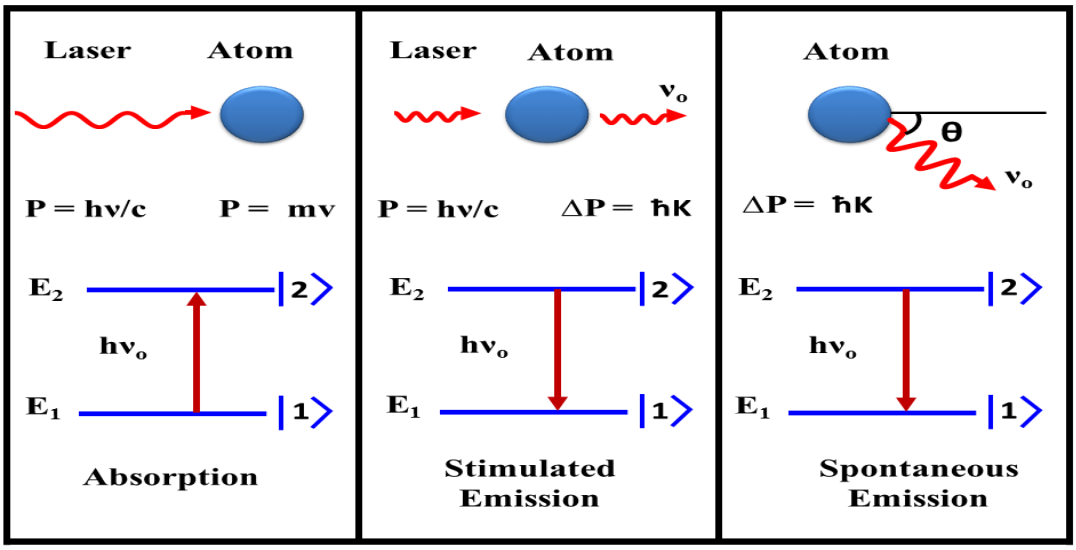

Figure 2.1: Atom-light interaction. An atom moves towards a laser beam, it can absorb a resonant photon and be excited. It will emit the absorbed photon either by stimulated or spontaneous emission. The spontaneously emitted photon travels in a random direction. After many cycles of absorption, stimulated and spontaneous emission, there will be a change in momentum due to the spontaneous emission which leads to scattering force.

The stimulated emitted photons are ignored because they are in the same direction as the laser beam. Therefore, after many cycles (N_{scat}) of atomic absorption and emission (spontaneous and stimulated) the momentum acquired by the atom is non zero :

$$\Delta\vec{P}_{total} = \sum_{n=1}^{N_{scat}} \hbar\vec{k}(1 - \cos\theta_n) \simeq N_{scat}\hbar\vec{k}. \tag{2.6}$$

Where θ_n represents the angle of the n-th spontaneously emitted photon. On average the net impulse from the spontaneous emitted photons tends to zero, thus $\sum_n \cos\theta_n \to 0$, N_{scat} is the number of photons scattered.

So, the resulting force, sometimes refers to it by dissipation force, is :

$$\vec{F}_{scat} = (\text{photon momentum}) \times (\text{scattering rate}). \tag{2.7}$$

Γ_{scat} represents the rate at which momentum is acquired by the atom due to absorption of a photon. The scattering rate $\Gamma_{scat} \equiv N_{scat}/\Delta t$, is the rate at which the photons are absorbed. $\vec{F}_{scat}$ depends on natural linewidth, γ, and angular frequency ω_o of an atomic transition in addition to the intensity, I, and angular frequency ω_L of the laser :

$$\Gamma_{scat} = \frac{\Gamma}{2} \frac{s_o}{1 + s_o + 4\frac{\delta^2}{\Gamma^2}}. \tag{2.8}$$

Where $s_o = I/I_{sat}$ is the saturation parameter, I_{sat} is saturation intensity of the transition and δ is the laser frequency detuning from resonance $\delta = \omega_L - \omega_o$.

$$I_{sat} = \frac{\pi h c \Gamma}{3\lambda^3}. \tag{2.9}$$

Therefore, the scattering force can be expressed as :

$$\vec{F}_{scat} = \hbar \vec{k} \frac{\Gamma}{2} \frac{s_o}{1 + s_o + 4\frac{\delta^2}{\Gamma^2}}. \tag{2.10}$$

2.1.1 Zeeman Slowing

The scattering force can slow down an atomic beam produced by an atomic source. The maximum force that can be exerted on the atomic beam is achieved when the frequency of both the laser beam and the atoms is identical, limiting the force to $F_{max} = \hbar k \Gamma/2$. Therefore, the maximum deceleration experienced by the atoms is:

$$a_{max} = \frac{F_{max}}{M} = \frac{\hbar k}{M} \frac{\Gamma}{2}. \tag{2.11}$$

Where M is the atomic mass. A counterpropagating beam of atoms that moves with velocity v can absorb a resonant laser light if its angular frequency ω_L equal to

$$\omega_L = \omega_o - k \cdot v,$$

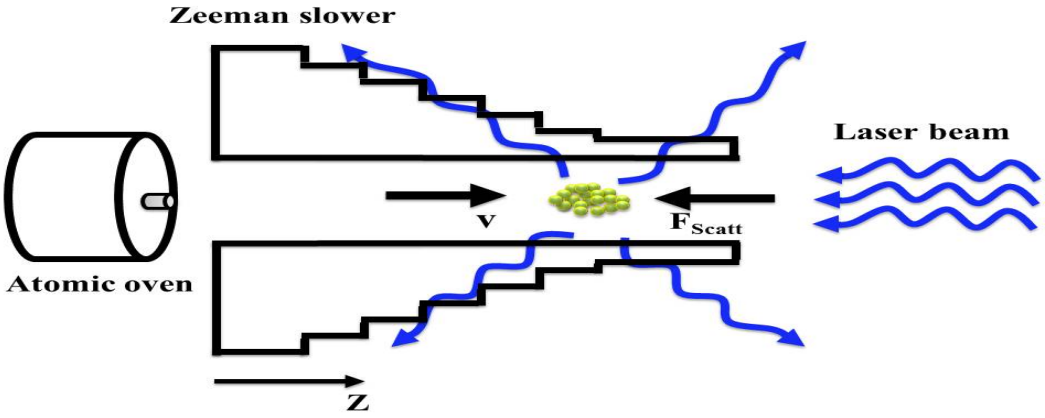

Figure 2.2: Schematic illustration of the Zeeman slowing mechanism. An inhomogeneous magnetic field can shift the atom's energy levels (according to the Zeeman Effect) to compensate for Doppler shift so that it keeps the atoms in resonance with the laser field.

As the atoms absorb the laser light repeatedly and get slowed down, the Doppler shift $(k \cdot v)$ is changed, and the atoms are no longer in resonance with the laser. The question now is how to keep the atoms and the laser in resonance?. Two techniques have been implemented to solve this problem: the first solution was to adjust (sweep) the laser frequency and that is called chirp cooling [81]. The second technique, which is more popular, is that of William Phillips and his co-works [82]. It relies on the Zeeman Effect, shifting the atom's energy levels can compensate for the change in the Doppler Effect when the atom slowed down. As shown in Fig. 2.2 an atomic beam travels along the axis of a tapered solenoid, the magnetic field, which varies with position, perturbs the energy levels of the atom so that the transition frequency matches the constant laser frequency; hence the magnetic field has to obey the condition:

$$\omega_o + \frac{\mu\mu_B B(z)}{\hbar} = \omega_L + k \cdot v. \tag{2.12}$$

Where μ is the magnetic moment, and μ_B is the Bohr magneton.

For constant deceleration, from an initial velocity v_o at z=0, the final velocity which is a function of position is given by:

$$v(z) = v_o\sqrt{1 - \frac{z}{L_o}}. \tag{2.13}$$

Where L_o is the stopping distance, and is equal to:

$$L_o = \frac{v_o^2}{2a}. \tag{2.14}$$

Where a is the deceleration of the atoms.Therefore, the desired magnetic field profile can be found from eq.4.3 and eq.2.13 :

$$B(z) = B_o\sqrt{1 - \frac{z}{L_o}} + B_{bias}. \tag{2.15}$$

For $0 \leq z \leq L_o$, where

$$B_o = \frac{\hbar k_L v_o}{\mu} \ , \ B_{bias} = \frac{\hbar(\omega_L - \omega_o)}{\mu}.$$

The decrease in the velocity of atom ($\frac{\mu B_o}{\hbar k}$) corresponds to a certain change in the magnetic field (B_o). Fig. 2.3 shows two profiles of the magnetic field used with Zeeman slowing, these vary with the position of the atoms in the the slower, generated by a typical Zeeman slower, with properly designed solenoids. The configuration with magnetic field ($B_{bias} > 0$) is described by Eq. 4.3, but the configuration with inverted magnetic field ($B_{bias} < 0$) has more practical advantages. first, the maximum value of the magnetic field is less which means either less current or fewer turns are needed. secondly, since the current flows in the both direction through the coils of the inversion slower, the magnetic fields from the two coils tend to cancel out.

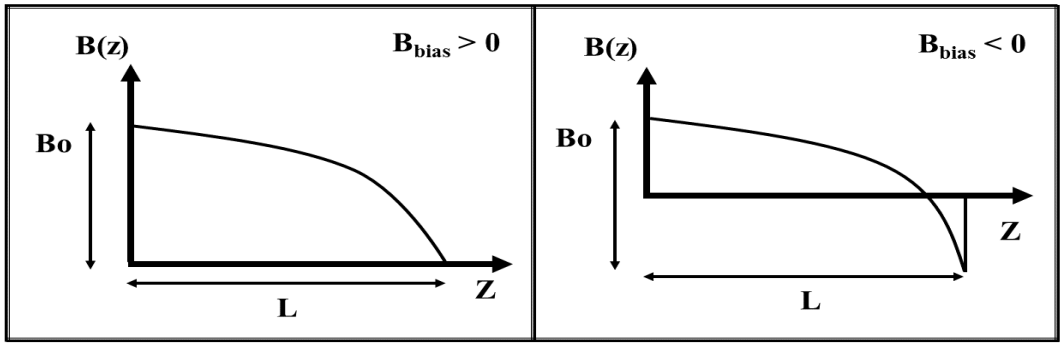

Figure 2.3: Configurations of the magnetic field for Zeeman slowing that generated by solenoid when the $B_{bias} > 0$ and when the $B_{bias} < 0$.

2.1.2 Optical Molasses

In a previous section, section 2.1, the concept of laser cooling was introduced through atom-light interaction. We have seen how a single laser beam can slow down a counter propagating atomic beam [82]. However, in reality, atoms in a gas move in all directions. Laser cooling is required along all the three Cartesian axes to reduce the mean square velocity of the atoms in order to reduce their temperature. In 1975 H*ä*nsch and Schawlow proposed (in a simplified 1D configuration) to use two counter-propagating laser beams that had same frequency [33]. This frequency was set to be slightly below the atomic resonance frequency. When the atom moves in the positive z direction it will experience the frequency of the laser beam traveling in the opposite direction (beam F_2) as closer to atomic resonance frequency (blue shifted). Thus it should absorb more photons from this laser beam than the beam traveling in the same (beam F_1) direction, as illustrated in Fig. 2.4. In this configuration, a moving atom will experience a scattering force caused by the "detuning" of the laser frequency, and

utilizing the Doppler Effect.

On the other hand, the atom will be less likely absorb from the other laser beam (beam F_1) because the beams frequency will be "seen" as shifted further away from the atomic resonance frequency (red shifted) [83]. Thus we see that the atom is subjected to different forces depending on its direction of movement, when it moves to the negative z direction; it will absorb more energy from laser beam (beam F_1) because its frequency is Doppler shifted closer to the atomic resonance. Overall, the atom will experience a force that opposes its velocity and slows down its motion as following [84]:

$$\begin{aligned}\vec{F}_{molasses} &= \vec{F}_{scatt}(\omega_L - \omega_o - k\vec{v}) - \vec{F}_{scatt}(\omega_L - \omega_o + k\vec{v}) \\ &\backsimeq \vec{F}_{scatt}(\omega_L - \omega_o) - k\vec{v}\frac{\partial \vec{F}}{\partial \omega} - [\vec{F}_{scatt}(\omega_L - \omega_o) + kv\frac{\partial \vec{F}}{\partial \omega}] \\ &\backsimeq -2\frac{\partial \vec{F}}{\partial \omega}k\vec{v}.\end{aligned} \tag{2.16}$$

The velocity of the atom and hence the Doppler shift is assumed to be low compared with decay rate ($kv \ll \Gamma$). The imbalance in the forces arising due to the Doppler Effect can be written as :

$$\vec{F}_{molasses} = -\alpha\vec{v}. \tag{2.17}$$

The result is a frictional or damping force exerted on the atom which is similar to the force experienced by a particle moving in a viscous fluid, and it is from this analogy, that the terms "optical molasses" has come. In 1985; Steven Chu et al. first demonstrated the optical molasses cooling [85]. This damping force requires a positive value for the damping coefficient (α), that the laser frequency detuning from the atomic resonance has to be ($\delta_L < 0$) (red shifted), and the damping coefficient will be:

$$\alpha = 2k\frac{\partial \vec{F}}{\partial \omega} = 4\hbar k^2 \frac{I}{I_{sat}} \frac{2\delta/\Gamma}{[1 + (2\delta/\Gamma)^2]^2}. \tag{2.18}$$

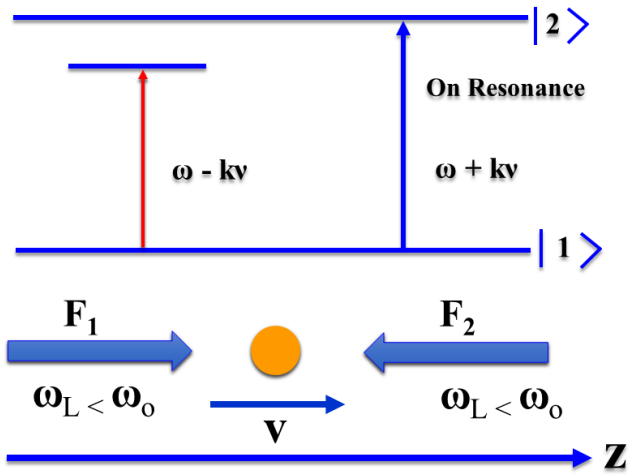

Figure 2.4: A schematic of the optical molasses mechanism (in 1 Dimension). If there is a pair of laser beams (F_1 and F_2) with same frequency point towards each other, and that frequency is tuned to be slightly below the atomic resonance frequency, an atom that moves in the + z will absorb more photons from the beam opposite to its velocity direction (beam F_2) because it "sees" the frequency of this beam is being closer to the atomic resonance frequency according to the Doppler Effect. The atom then experiences a damping force $= -\alpha\vec{v}$ decelerating it. The opposite happens when it moves in the - z, direction, it will absorb more from (beam F_1) [3].

This treatment of optical molasses is valid when the laser intensity is much less than the saturation intensity ($I/I_{sat} \ll 1$). The configuration of optical molasses in 1 dimension as introduced above, can be generalized by adding another two pairs of counter-propagating laser beams along the other Cartesian axes, to obtain laser cooling in three dimensions as shown in Figure 2.5. Because the imbalance in the optical molasses forces relies on the Doppler Effect, this technique is called "Doppler cooling".

The atom's temperature due to the optical molasses cooling will depend on the balance between the cooling and heating rates. The heating rate arises from random

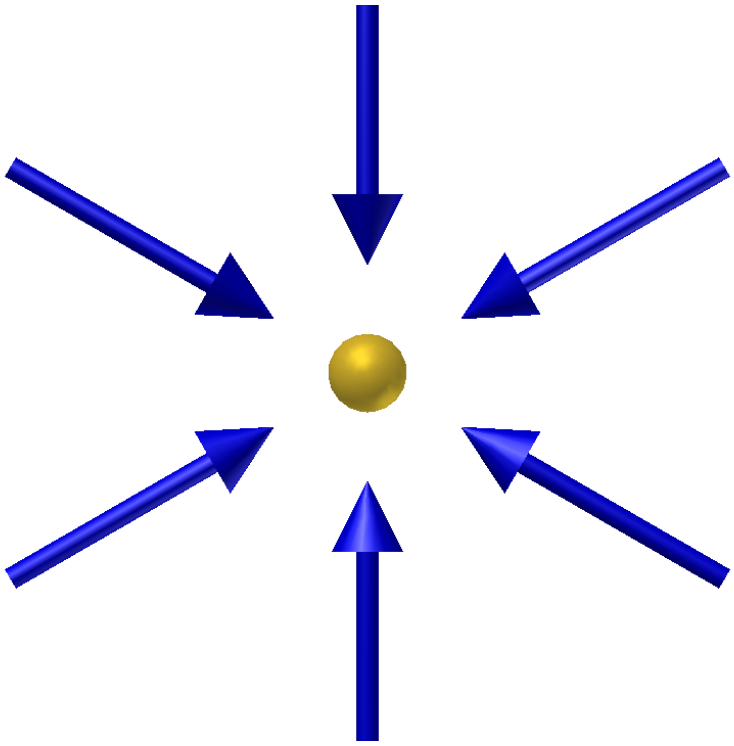

Figure 2.5: schematic of laser configuration for three-dimensional optical molasses.

absorption and emission processes in the scattering force. The atoms always gain recoil energy, once from the absorption and the again from the emission. So the final temperature is given by:

$$T_D = \frac{\hbar\Gamma}{2k_B}. \tag{2.19}$$

This relation describes the lowest temperature that achievable with the simplified two-level atoms in optical molasses, and it is called the "Doppler limit" [83]. Atoms that have degenerate sublevels can be cooled beyond the Doppler limit by utilizing an additional cooling mechanism known as Sisyphus cooling [86–88]. This sub - Doppler cooling also has a limit set by the energy of recoil gained by a single photon emission, $E_r = \hbar^2 k^2 / 2M$, leading to:

$$T_r = \frac{\hbar^2 k^2}{M k_B}. \tag{2.20}$$

Which represents the lowest achievable temperature with sub - Doppler cooling [89,

90].

2.1.3 Magneto-Optical Trap

The optical molasses technique is an effective way to cool neutral atoms down to temperatures in the μK. The atoms accumulate in the area where the three orthogonal counter-propagating laser beams overlap. These atoms diffuse out from the accumulation area after some time; typically several seconds for beams of 1 cm radius. this is due to their residual velocity from the recoil heating, and is acquired from absorption and emission of the scattering force. Therefore, to trap these atoms robustly, a restoring force is required. Fortunately, the configuration of the optical molasses can be turned into a trap by adding a magnetic field gradient with the correct choice of laser beams polarization. The result is a new technique called Magneto-Optical Trap (MOT) [91, 92]. Two coils in anti-Helmholtz configuration generate a magnetic field, where the same magnitude current flows in opposite directions in the coils so that the quadrupole magnetic field is cancelled out in the center of the trap (B = 0) and grows linearly with distance away from it. The operational principle of the magneto-optical trap (in one dimension) is explained with the aid of Fig. 2.6, for an atom that has a simple transition from J = 0 $\Rightarrow$ J = 1. According to the Zeeman Effect, the quadrupole magnetic field shifts the sub-energy levels ($\Delta M_J = 0, \pm 1$) of the J = 1 state linearly with the atom's position. The Zeeman shift with the selection rules give rise to an imbalance in the scattering force of the laser beams that confine the atom in the trap center (where $z = 0$) as follows. Assume an atom is diffusing away from the trap center in the +z direction along the z-axis. The $\Delta m_J = -1$ transition will be closer to resonance with the laser, as the laser frequency was already detuned towards the red before applying the magnetic field (B = 0). Selection rules dictate that the

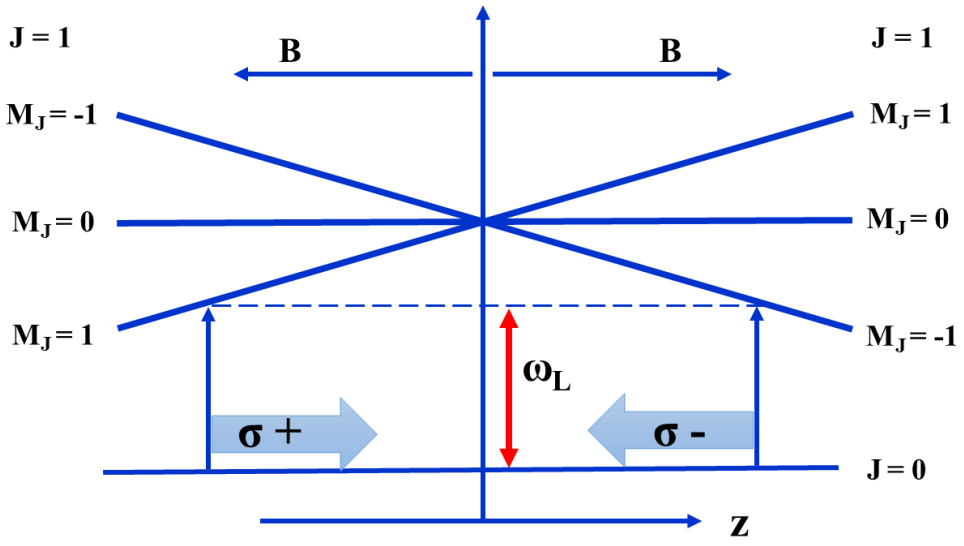

Figure 2.6: The magneto-optical trap mechanism (in 1 Dimension) for an atom with J = 0 ⇒ J= 1 transition. In the presence of a magnetic field gradient generated by anti-Helmholtz configuration, the sub-energy levels vary linearly depending on the atom's position according to the Zeeman Effect. When two counter-propagating beams with circular polarization shine towards the atom there is an imbalance in the scattering force from laser beams that keep the atom on the center of the trap.

atom absorbs more photons from the beam that excite the σ^- transition which leads to the scattering force that pushes the atom back towards the center of the trap. The opposite applies to an atom moves towards -z direction, the $\Delta m_J = +1$ transition will be closer to resonance with the laser, so the selection rules lead to more photons being absorbed from the beam that excites the σ^+ transition. Thus the scattering force pushes the atom back towards $z = 0$ [93]. The force experienced by the atom in the MOT can be expressed as [3]:

$$\begin{aligned}\vec{F}_{MOT} &= \vec{F}^{+}_{scatt}(\omega_L - k\vec{v} - (\omega_o + \beta z)) - \vec{F}^{-}_{scatt}((\omega_L + k\vec{v} - (\omega_o - \beta z)) \\ &\backsimeq -2\frac{\partial \vec{F}}{\partial \omega}k\vec{v} + 2\frac{\partial \vec{F}}{\partial \omega_o}\beta z.\end{aligned} \tag{2.21}$$

Where the $(\omega_o + \beta z)$ and $(\omega_o - \beta z)$ terms respectively represent the resonant absorption frequency for the $\Delta m_J = +1$ and $\Delta m_J = -1$ transitions respectively that arises from

Zeeman shift at z :

$$\beta z = \frac{g\mu_B}{\hbar}\frac{dB}{dz}z. \tag{2.22}$$

Where the $g = g_j$ is the Landé g-factor and μ_B is Bohr magneton. As the force (in the MOT) depends on the detuning of the laser frequency from the atomic resonance frequency $\delta = \omega - \omega_o$; we can write $(\partial F/\partial\omega_o = -\partial F/\partial\omega)$, leading to:

$$\begin{aligned} \vec{F}_{MOT} &= -2\frac{\partial\vec{F}}{\partial\omega}(k\vec{v} + \beta z) \\ &= -\alpha\vec{v} - \frac{\alpha\beta}{k}\ z. \end{aligned} \tag{2.23}$$

Atoms that enter the MOT fall under the influence of two forces simultaneously: a damping force in velocity (as in optical molasses) that give rise to cooling, and a restoring force that pushes the cooled atoms towards the trap center causes taping. The Zeeman Effect causes an imbalance in the scattering force which leads to a restoring force with a constant of proportionality $\alpha\beta/k$. Under certain operational conditions both of the Zeeman shift and the atom velocity are small $\beta z \ll \Gamma, kv \ll \Gamma$ respectively.

The one dimension magneto-optical trap configuration can be extended into three dimensions by adding another two orthogonal pairs of laser beams, exactly as in optical molasses, taking into consideration the polarization sequence. Fig. 2.7 is a schematic showing the geometry of the three-dimensional MOT. This configuration of the trap is robust and reliable. The number of atoms in a MOT exceeds that in an optical molasses because the Zeeman Effect shifts the atomic energy levels allowing capture of faster atoms. The capture velocity for an magneto-optical trap depends on the radius, r, of the laser beams and can be estimated as:

$$v_c = \sqrt{2ra_{eff}}.$$

With a_{eff} being the effective deceleration experienced by the atom when the intensity

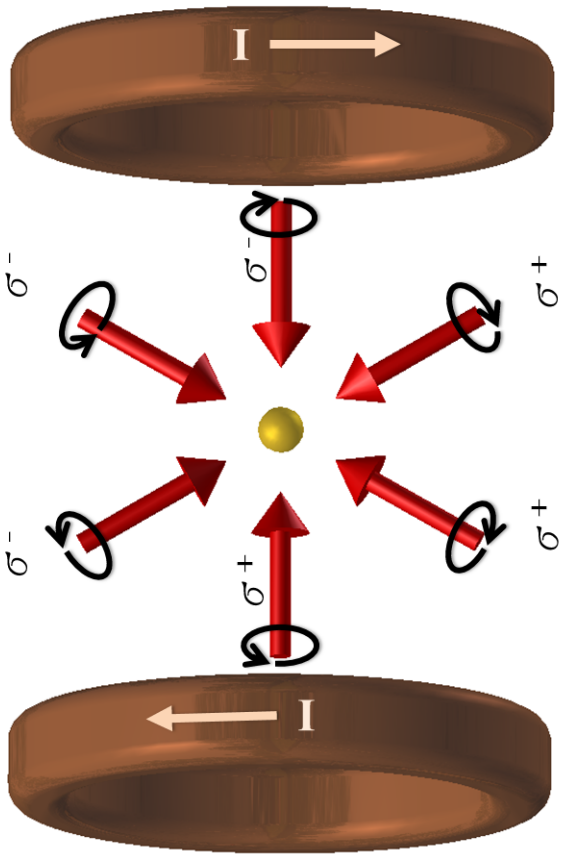

Figure 2.7: Schematic of a three-dimensional magneto-optical trap configuration formed by three orthogonal counter-propagating laser beams (as with optical molasses). With the correct choice of circular polarization, the beams overlap at the center of a pair of coils. The quadrupole magnetic field is zero at the center and grows linearly in every direction [4].

of the laser equals the saturation intensity, if the influence of fluctuations in scattering force included :

$$a_{eff} = \frac{1}{2}a = \frac{a_{max}}{4},$$

a_{max} is given by Eq. 2.11, therefore the final capture velocity of the MOT will be :

$$v_c = \sqrt{\frac{\hbar k}{M}\frac{\Gamma}{4}r}. \tag{2.24}$$

The temperature of the atoms in the magneto-optical trap is higher than the temperature of the atoms in optical molasses for two reasons. If the MOT contains a large

number of atoms so there is a high atomic density, then there will be multiple scattering events; an atom can reabsorb a resonant photon emitted from another atom. In addition, the Zeeman Effect breaks down the sub-Doppler mechanism due to the strong magnetic field that interrupts the energy level degeneracy.

2.2 Strontium Atoms

To be selected as an optical frequency reference an element must have special features. The most importantly it must exhibit a high-quality factor (Q) transition in the optical domain that can be interrogated with an available laser. Moreover, this transition must be insensitive to any external perturbations caused by magnetic or electric field. The element should also provide an efficient and rapid cycling transition to prepare the ultracold atoms through the laser cooling and trapping. Rapid cycling transition is vital to cool and trap the thermal atoms in a short time. As mentioned in section 2.1 when an atom absorbs a resonant photon it receives a momentum impulse $\hbar k$, so the motion of the atom reduces by the recoil velocity:

$$v_r = \frac{\hbar k}{m}. \tag{2.25}$$

The same thing will happen when the atom emits a photon by spontaneous emission. Usually, the recoil velocity is small, however, if the repetition rate is high, the velocity of the atom can reduce significantly. For instance, the strontium recoil velocity for $^1\mathrm{S}_0$-$^1P_1$ transition at 461nm is 9.88 mm/s, but the $\Gamma{\approx}1{\times}10^7$ 1/s for same transition. Therefore, scattering many photons can reduce the velocity of the strontium atom from hundreds of m/s to approximately "standing still" in a fraction of second. Although the Doppler limit for the rapid cycle transition is high, a second cooling transition can be used to reduce the atom temperature to the a degree that can with it confine the atom in the optical lattice. Furthermore, rapid cycle transition could improve the stability of the clock by reducing the cycling time of measurements T_{cyc} as given in equation 1.3.

According to these requirements, only a few elements satisfy the operation conditions of an optical lattice clock . The alkaline-earth metals and alkaline-earth met-

als like neutral atoms due to their suitable energy level structure appear to be the most promising candidates for optical lattice clock applications. They have attracted considerable attention by research groups around the words who have investigate theirs characterization, the atoms investigated include Mg [94,95], Ca [96], Sr [58,97], Yb [98, 99] and Hg [100].

The electronic structure of these elements ends with two valance electrons in the outer shell, therefore, their energy levels are separated into two groups: singlet with total spin ($\Delta s = 0$) when the electrons are anti-parallels, and triplet with the total spin ($\Delta s = 1$) for parallel electrons. The selection rule dictates that transitions between the singlet and triplet states are forbidden. However, spin-orbit coupling provides a finite lifetime for these transitions to occur, so the resulting transitions also called "intercombination lines" are very narrow in linewidth which makes them very suitable for metrological applications. Among the alkaline-earth metals and alkaline-earth-like elements, strontium possesses most of these useful features, as can be seen in Tables 2.1, and 2.2. Strontium is highly reactive; it forms compounds with silicates, oxygen, water, and nitrogen, but does not react with the sapphire. Therefore, using sapphire windows is essential when one working with strontium [101].

Strontium has four natural isotopes, three of them are bosonic, and the other one is fermionic, their properties are listed in Table 2.3. The nuclear spin for the even (bosonic) isotopes is zero, with total angular momentum ($J = 0$). These particles are considered a perfect scalar, due to the lack of the hyperfine sub - levels which increase their insensitivity to an external magnetic field. This point is significant for high precision measurements. Furthermore, the absence of nuclear spin simplifies the energy level structure. Thus these isotopes provide excellent verification of the laser cooling theory based on a two levels systems [102]. However, the simplified bosonic

Atomic species	Z	λ_1(nm)	γ_1 (MHz)	λ_2(nm)	γ_2 (kHz)	λ_3(nm)
^{9}Be	4	235	89	455	$\approx 10^{-3}$	
^{24}Mg	12	285	79	457	0.048	458
^{40}Ca	20	423	34	657	0.37	657
^{88}Sr	38	461	32	689	7.4	698
^{138}Ba	56	554	20	791	50	
^{174}Yb	70	399	28	556	180	578
^{199}Hg	80	185	119	253	1.3×10^{3}	265

Table 2.1: Values of relevant parameters for optical lattice clock operation (wavelength and linewidth for first and second cooling stage transitions, in addition to the clock laser wavelength) for stable alkaline-earth and alkaline-earth-like atoms [8–10].

Atomic species	λ_{Clock}(nm)	γ_{Clock} (Hz)	$\lambda_{Repump1}$ (nm)	$\lambda_{Repump2}$ (nm)	Opt. pump (nm)	λ_{magic}(nm)
Sr	698	1mHz	707.2	679.3	2603	813.4
Yb	578	10mHz	770.2	649.1	1388	759.4
Hg	265	100 mHz	546.1	404.6	759.4	360

Table 2.2: The clock laser, repumpers, and magic wavelength for Sr, Yb, and Hg atomic species [11].

structure can limit the lowest temperature achievable by laser cooling due to the lack of the hyperfine structure.

Fig. 2.8 shows the strontium energy levels diagram with the $Russel - Saunders$ notation of $^{2S+1}L_J$ where S is the total spin quantum number, L is the orbital angular momentum and J is the total angular momentum of the electron. Strontium attracts particular attention due to the $^{1}S_0 - ^{3}P_0$ "Intercombination line", this transition is

Isotopes	Relative atomic mass	Nuclear spin	Natural abundant
88	87.905 6143(24)	0	82.58 (1) %
86	85.909 2624(24)	0	9.86 (1) %
87	86.908 8793(24)	9/2	7.0 (1) %
84	83.913 425(4)	0	0.56 (1) %

Table 2.3: The Strontium Natural Isotopes (NIST data) [12].

forbidden by the selection rules ($\Delta S = 0$ and $J = 0 \Rightarrow J = 0$). The ^{88}Sr has a simple structure due to the absence of the nuclear spin ($I = 0$). It also has the highest abundance among the strontium isotopes. These reasons make it easier to start with ^{88}Sr to develop an optical lattice clock based on strontium. The lack of hyperfine structure makes the ^{1}S$_0$-^{3}P$_0$ transition immune to both: magnetic field (no first-order Zeeman shift), and vector light shift (tenser light shift is cancelled in the lattice). However, the lack of hyperfine structure implies that the ^{1}S$_0$-^{3}P$_0$ transition is strictly forbidden by the spin and total angular momentum selection rule. Applying an external magnetic field (≈10 G) [103] or intense light probe leads to exciting this transition. In such a situation, there will be a second-order Zeeman shift or a light-light probe shift. Implementing a hyper-Ramsey type of interrogation protocol could relieve these issues because it is insensitive to the shift caused by probe light [45], whereas, because the hyperfine mixing the ^{87}Sr has a linewidth of ∼1 mHz. This extremely narrow transition in the optical domain, at 698 nm is accessible by solid-state laser and, recently, by diode lasers [104, 105].

In addition to the clock transition $^1S_0 - ^3P_0$, strontium has another two transitions that used to obtain the cold atomic sample. The $^1S_0 - ^1P_1$ is a strongly allowed transition because it is between singlet states it has a natural linewidth of 32 MHz at

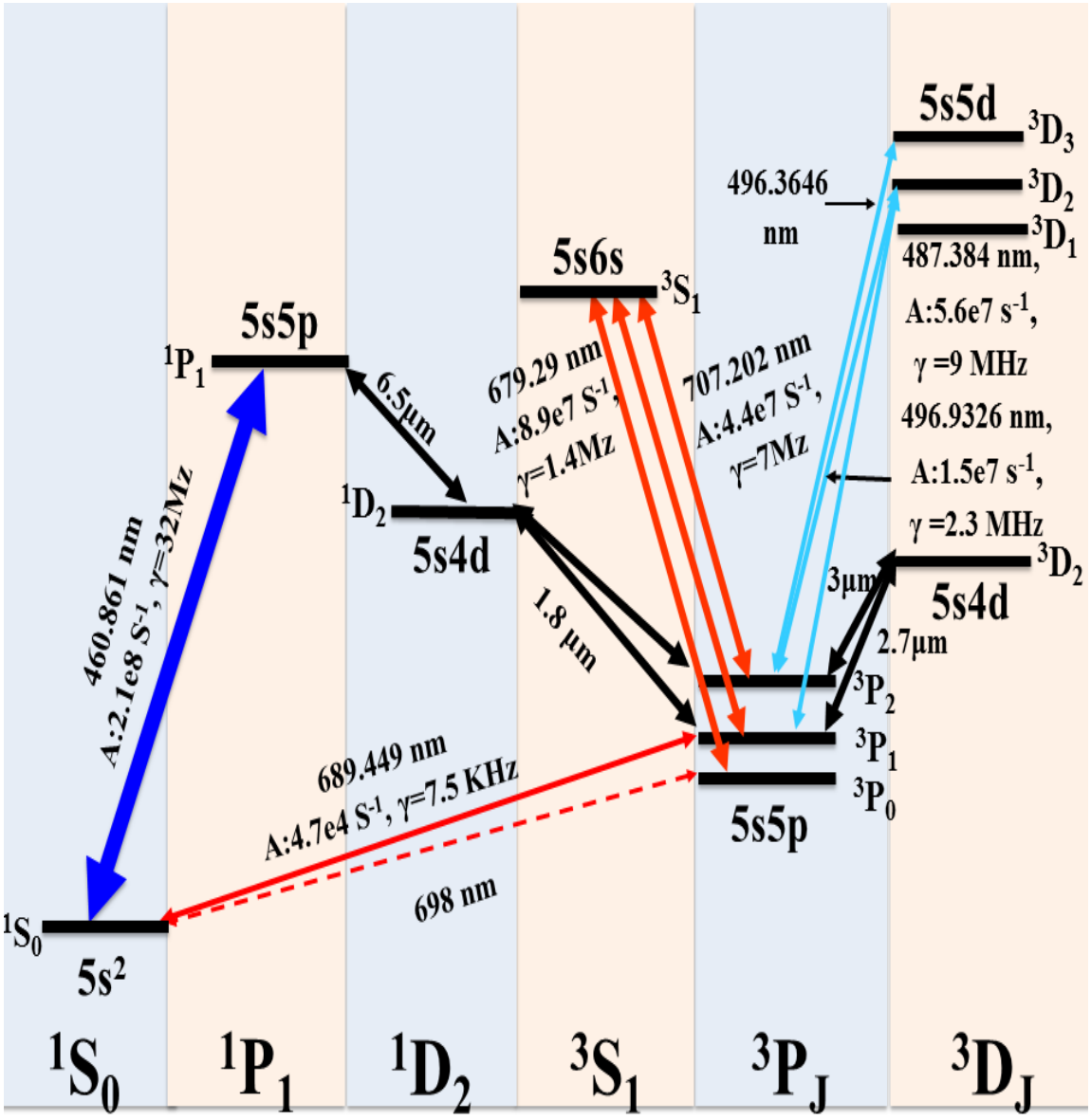

Figure 2.8: Strontium energy levels diagram.

461nm. This transition is used to slow the atomic beam and trap the slowed atoms in the MOT. Atoms trapped in the blue MOT are cooled to a temperature in the order of a few mK. The final temperature of the atoms in the first stage cooling is determined by the Doppler limit, Eq. 2.19, which depends on the natural linewidth of the transition. The ${}^1S_0 - {}^1P_1$ is not entirely a closed transition, the majority of electrons that reach the ${}^1P_1$ state, will decay back to the ground state with branching $2 \cdot 10^{-5}$ will decay to the ${}^1D_2$ state. From this state electrons can either decay to ${}^3P_1$ with probability 66% then to the ground state or decay to the ${}^3P_2$ metastable state with probability 33% but these electrons can not decay to the ground state immediately. They have to re-pumped to the ${}^3P_1$ state in order to decay to the ground state. Thus there are three schemes in which repumping lasers can be used:

${}^3P_2 - {}^3D_2$: In this scheme electrons in the ${}^3P_2$ state are re-pumped to the $5s5d^3D_2$ state, so that they can then decay back to the ground state via the ${}^3P_1$ state. This setup requires a laser with wavelength = 495 nm, but there was no such laser available at this wavelength which mean a frequency doubling system had to be built.

${}^3P_2 - {}^3S_1$: This scheme requires the use of two lasers. The first laser with a wavelength of 707 nm to pump the atoms from ${}^3P_2$ to ${}^3S_1$ state, from here electrons decay to all ${}^3P_J$ states. If they decay to the ${}^3P_2$ state the same 707 nm laser will re-pump them. If they decay to the ${}^3P_1$ state, they can decay to the ground state. The final possibility is if they decay to the ${}^3P_0$ state and here a 679 nm laser is required to re-pump them to the ${}^3S_1$ state.

A final option is to use a 3μm laser to re-pump the atoms from the ${}^3P_2$ to the $5s4d^3D_2$ state, and then atoms can decay to ${}^3P_1$ and from there to the ground state [106].

The final transition we have to mention is the ${}^1S_0 - {}^3P_1$ intercombination line,

Transition	λ	T_D	T_r	I_{sat}	a_{max}
$^1S_0 - ^1P_1$	461 nm	770 μk	1.03 μk	42.7 mW/cm^2	$\approx 10^6\ m/s^2$
$^1S_0 - ^3P_1$	689 nm	180 nk	460 nk	3 mW/cm^2	160 m/s^2

Table 2.4: The relevant parameters for Strontium cooling and trapping in the first and second cooling stages.

with a natural line width of 7.4 kHz. This transition is used to further cool the strontium atoms in the Red MOT to temperatures typically a few μK. Remarkably, the Doppler temperature limit for this transition (T_D = 180 nK) is lower than the recoil temperature T_r = 460 nK set by the photon recoil energy temperature Eq. 2.20. This temperature represents the lowest achievable temperature with laser cooling [107–111]. Table 2.4 shows the relevant parameters for the Blue and Red MOT.

The main disadvantage of working with alkaline-earth metal (like) atoms in general and strontium, in particular, is that their vapour pressure is low. Compared with alkali elements to obtain the same atomic vapour that Cs and Rb (for example) have under vacuum conditions at the room temperature, metallic strontium have to be heated to around 400 °C see Fig. 2.9. Therefore, a vapour cell cannot be used to cool and trap the strontium atoms. Firstly, strontium known to react with silicates in the glass to form an opaque layer that blocks the optical access - one solution to this problem (as explained above) is to use sapphire windows. An alternative solution is to use a buffer gas to isolate the window from the atomic vapour as described in [112], but that increases the background pressure, affecting the efficiency of the laser cooling by thermalizing the cooled atoms especially when the atoms transfer to the optical lattice to probe their spectroscopy by a clock laser. The final drawback of using a vapour cell is due to the a large shift in the clock transition due to black

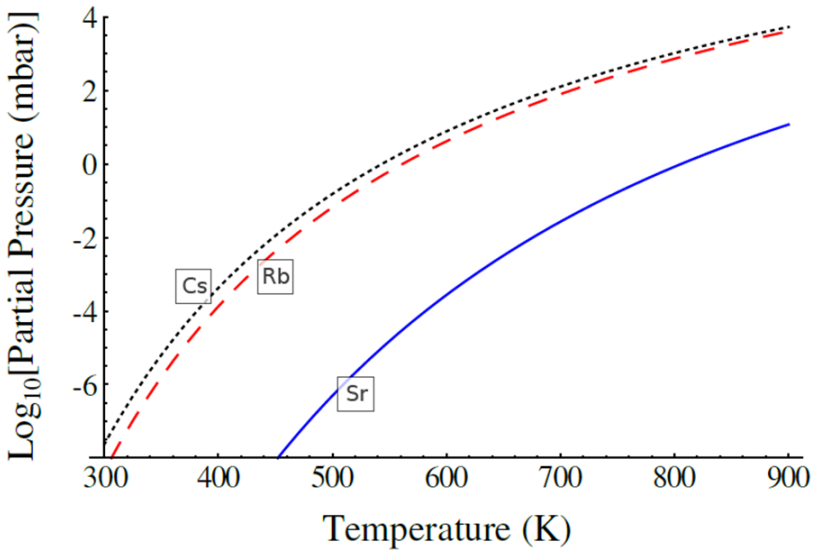

Figure 2.9: Strontium vapour pressure compared with alkali atoms, Cs and Rb [5].

body radiation. At high temperatures (600 °C) the black body radiation quenches the metastable state by driving the 2.6μm transition from $^3D_1$ that decays back to the ground state through $^3P_1$ leading to quenching the clock transition from $\sim$ 132s to $\sim$ 100ms [113].

Chapter 3

Experimental Setup

This chapter will describe the experimental setup constructed at the University of Birmingham as an essential part of the programme towards realizing a strontium optical lattice clock. In particular, it will focus on describing the experimental apparatus that I designed and built in order to produce ultra-cold strontium atoms which represent the heart of the clock. The experimental apparatus consisted of two parts: the "vacuum system" and the "atomic package" joined together through a differential pumping tube. The atomic package was composed of the science chamber and a magnetic field generator, which are the anti-Helmholtz coils in addition to compensation coils. Fig.3.1 shows the two main sections of the experimental apparatus, without the compensation coils, as indicated by the dashed rectangles.

3.1 Vacuum System

Laser cooling and trapping with neutral atoms requires a vacuum system. An atom will not be cooled if it is kept in an environment in which it is impacted by other atoms. Each time the atom receives a "kick" from a laser photon, it will interact

with surrounding atoms or molecules and gain energy, raising its temperature. To minimize the presence of background gases in order to cool and trap the strontium atoms requires at least a high vacuum (HV) (1×10^{-6} mbar). Whereas, an Ultra-high vacuum (UHV) (1×10^{-9} mbar) or lower is required to capture the greatest number of atoms or reach the lowest temperature. The material from which the vacuum system was constructed was stainless steel, except the science chamber which was made out of titanium, and the atomic source which contained some aluminum and alumina.

Here I gives an overview of the whole vacuum system that I have designed and assembled to cool and trap the strontium atoms, and below I will introduce each subsystem in detail. Fig. 3.1 is a CAD drawing that illustrates the vacuum system which consists of two main sections: The atomic source at the one end and the science chamber at the other end.

The vacuum parts were joined using a DN 35 CF flange with fully annealed copper gaskets. The two regions are connected through a differential pumping tube. As the vapour pressure of strontium is low, the strontium has to be heated to around 400 °C in order to produce strontium atomic vapour. An atomic oven was used for this purpose.

The science chamber region was responsible for slowing, cooling, and trapping the strontium atoms by means of the magneto-optical trap. The system is pumped by two types of vacuum pumps : three ion pumps (from Gamma Vacuum) and one getter pump (from Saes CapaciTorr group). The ion pumps are two 25S and one 3S Titan with pumping speed 25 l/s and 3 l/s respectively.

The first 25S ion pump was in the atomic oven section. It was connected to the vacuum system through a four-way cross together with a valve and the other 25S ion pump placed at the start of the science chamber area and joined to it through a

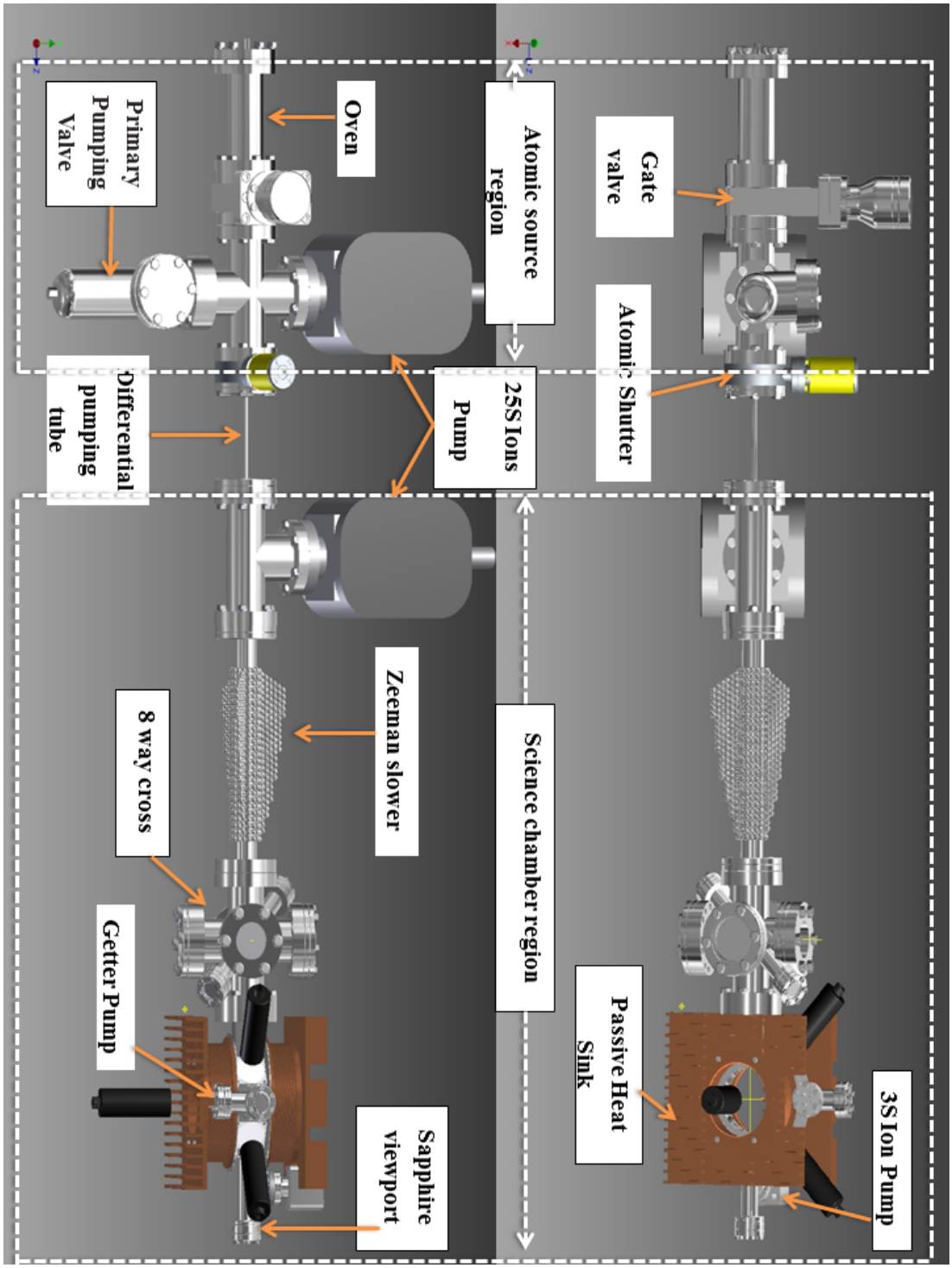

Figure 3.1: CAD drawing of the designed and built vacuum system in two views. Left : top view, Right : side view, with the labeling of each component. The two main sections of the vacuum setup are indicated by the dashed rectangles.

DN 35 CF "T" pipe (both the ion pumps are placed before and after the differential pumping tube). The 3S ion pump and the getter pump were attached to the science chamber directly through standard DN 16 CF "T" pipe so that the optical access for the Zeeman slower beam and clock laser beam kept clear.

The pressure of the system was monitored using two Gamma Vacuum digital controllers: a large pump controller for both 25S ion pumps and small pump controller for the 3S pump. The CF 16 MK2 capaciTorr pump which uses non evaporative getter materials, needed to be activated by applying 5 A for 45 min. Although, these types of pumps had developed about two decades ago, I built a vacuum cell consisting of a valve, four-way cross, and the getter pump to evaluate its performance. The getter pump is attached to the four-way cross for more than a month. The pressure was monitored and the result summarized in the graph shown in Fig.3.2. The graph demonstrate that getter pump was working effectively, the pressure was reduced from $\approx 1.4\times10^{-7}$ mbar to $\approx 2\times10^{-8}$ mbar.

The Zeeman slower was positioned after the differential pumping tube to increase the loading efficiency of the magneto-optical trap by slowing the strontium atoms that evaporated from the atomic oven. The Zeeman slower was followed by an eight-way cross that could be used as a two-dimensional magneto-optical trap for additional cooling and collimating the atomic beam. Despite being part of the system, it has not yet been used.

To get rid of impurities/gases, the system was baked at around 200 °C several days while connected to the molecular turbo pump through the primary pumping. This did not apply to the science chamber. The melting point of indium is about 156 °C, so I was careful not to increase its temperature above 100 °C, as will be explained later. The ion pumps should not switched on unless the pressure is in the order of

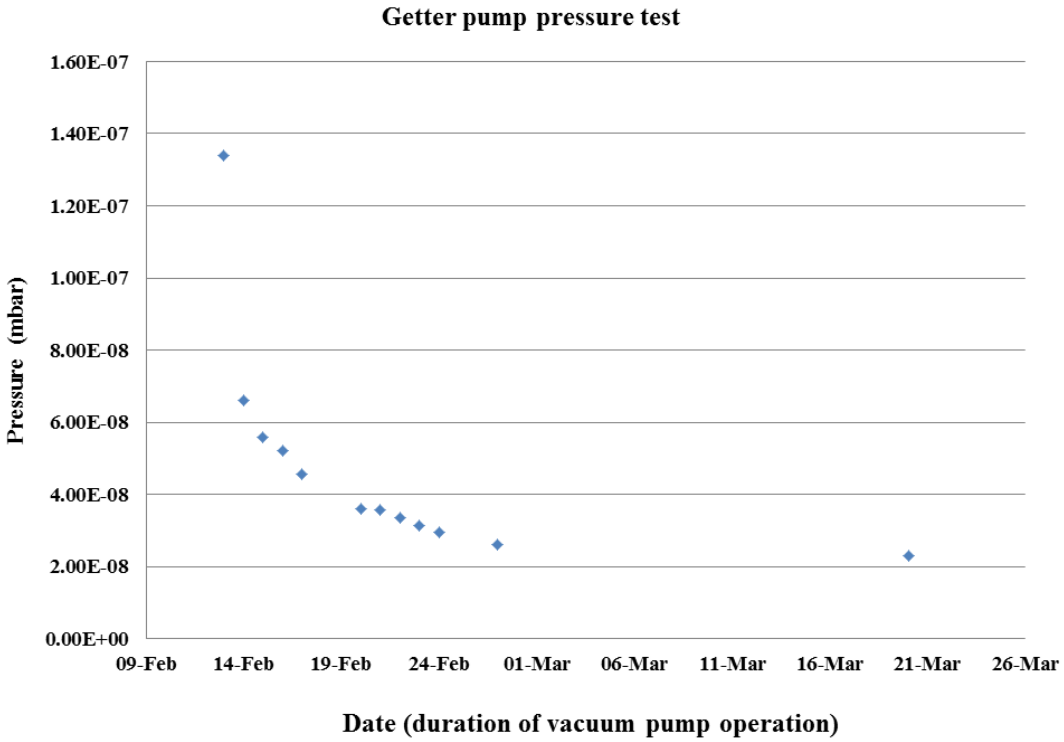

Figure 3.2: The getter pump was tested by attaching it to a small vacuum setup consist of a four-way cross and valve. The pressure monitored for more than one month.

1×10^{-6} mbar or less.

3.1.1 The Atomic Source

The strontium atomic vapour was generated by heating the metallic strontium to ≈400 °C in a vacuum. Two types of atomic sources are widely used for the production of strontium atomic beam: dispensers and atomic ovens. Although dispensers are available commercially, the atomic oven is preferable for the following reasons:

Lifetime: The lifetime of the oven is much longer than that of dispenser due to their capacity. The capacity of a dispenser varies between 100 mg to 500 mg [114] which is estimated at one year's continuous operation, whereas the capacity of the atomic oven in our setup is around 6 g which could provide 10 years continuous

operation [115].

Collimation of the atomic beam: The atomic oven provides better collimation of the atomic beam due to the presence of capillaries. A less divergent the atomic beam means more atoms reach the MOT. In contrast, the atoms leave from the dispenser more as a fountain, which means a small fraction reach the MOT.

Power consumption and black body radiation: The sophisticated design of the oven reduces both the power required to evaporate the strontium, and the amount of black body radiation (BBR), by using a shielding technique. The heat generated inside the oven is reflected back to the reservoir (where the bulk of the strontium is kept) to increase its temperature. For the strontium to emit vapour the whole body of the dispenser had to be heated. This required an electrical supply of about 15 A [5]. Because the dispenser is in a line with MOT, the amount of receive BBR will be high. The BBR induce the AC Stark shift which is one of the major uncertainties in the accuracy of the optical clocks [116].

The atomic oven (in this setup) was adapted from [15] and redesigned by a member of the Space Optical clock (SOC2) project, Lyndsie Smith [117]. The oven was machined at the school of Physics & Astronomy workshop, as it can seen in Fig.3.3, it consisted of:

Atomic dispenser: A 33 mm long stainless steel tube, with 10 mm inner diameter, a DN 16 CF flange at its bottom, and a 4 mm hole at the top. Into this hole was fitted the capillary tubes which collimated the atomic beam. The capillary tubes was made from stainless steel, 8 mm long and 0.2 mm inner diameter. The atomic dispenser was sealed with a standard DN 16 CF blank flange.

Heating tube: Made from alumina material to ensure better thermal isolation, it

fitted onto the atomic reservoir. The heat was generated by a tantalum wire (from Goodfellow Cambridge Ltd.) with a diameter of 0.25 mm that Connected to the feedthrough.

Shielding unit: Consisted of two pieces of polished aluminum. The smaller piece was the same size as the DN 16 CF flange and was placed under the atomic dispenser whereas the larger piece covered the entire body of the oven.

The strontium is known to react with the oxygen to form strontium oxide (SrO). To load the atomic source, therefore, it is essential to isolate the strontium from the air. A Transparent plastic box was used to totally enclose the oven. The box was filled with argon first and then the strontium was cleaned from the oil and loaded into the oven. After assembling the oven, it was connected to the apparatus by inserting it inside a 8 cm long full nipple as shown in Fig.3.1.

3.1.2 Gate Valve and Atomic Beam Shutter

A gate valve (from the Kurt J Lesker company) was installed immediately after the nipple that contained the atomic oven, this was to separate the atomic source section from the rest of the vacuum system and maintain the vacuum in the atomic oven section if there was ever a need to break the vacuum in the science chamber section. In that way the strontium in the oven would not oxidize.

It is highly desirable to maintain the vacuum in the science chamber should it be necessary to reload the atomic oven with strontium. This can be achieved by adding another valve to the science chamber section and changing the position of the gate valve and the atomic beam shutter as illustrated in Fig. 3.4.

For an efficient loading of the MOT a thick and slow atomic beam is needed.

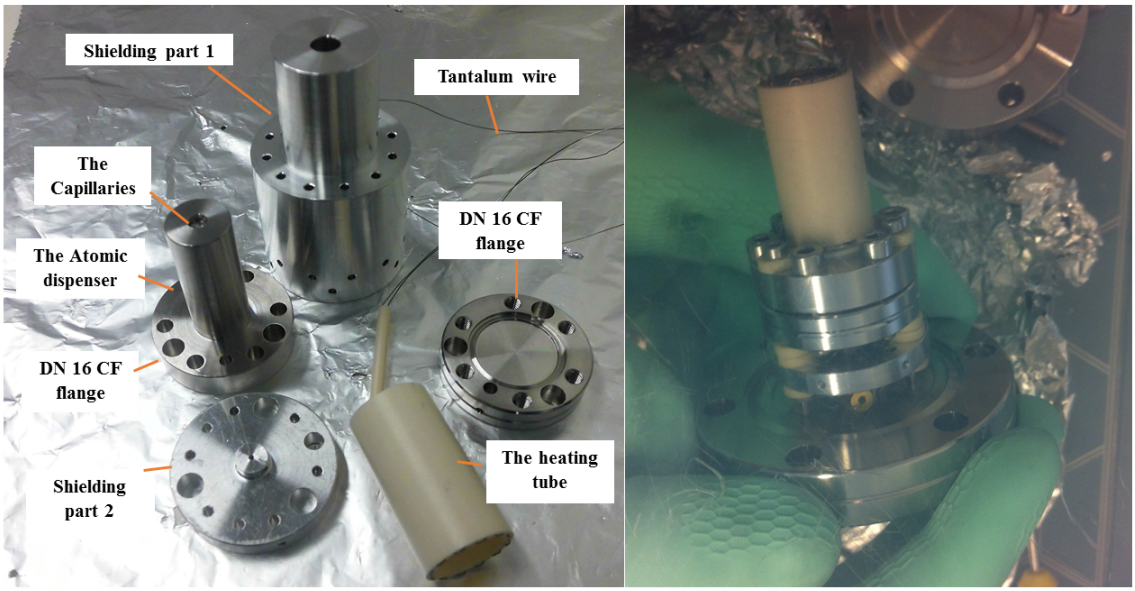

Figure 3.3: Photographs show (A) The essential component of the atomic oven: the atomic dispenser where the 6 g of Sr was positioned (the reservoir), the DN 16 CF flange to seal the atomic dispenser with a nickel gasket because cooper reacts with strontium and nickel can resist the high temperatures. The tube was heated using the tantalum wire, with the shielding parts reflecting the heat back to the atomic dispenser in order to minimize heat losses by black body radiation. (B) Strontium is a highly reactive element and must be contained in an inert environment; vacuum, argon or oil, for example. The atomic oven, therefore, was loaded with Sr and assembled inside a transparent box filled with argon gas to protect it from oxidation.

Zeeman slowing has proved to be the most successful technique to produce such an atomic beam. Nevertheless, these slowed atoms still could heat the atoms in the trap and thus an atomic beam shutter was installed to completely block the path of the atomic beam whenever it is required as seen in Fig. 3.1. For example, when interrogating a sample of cold atoms with a clock laser they need to be completely isolated, especially from the BBR generated by the atomic oven.

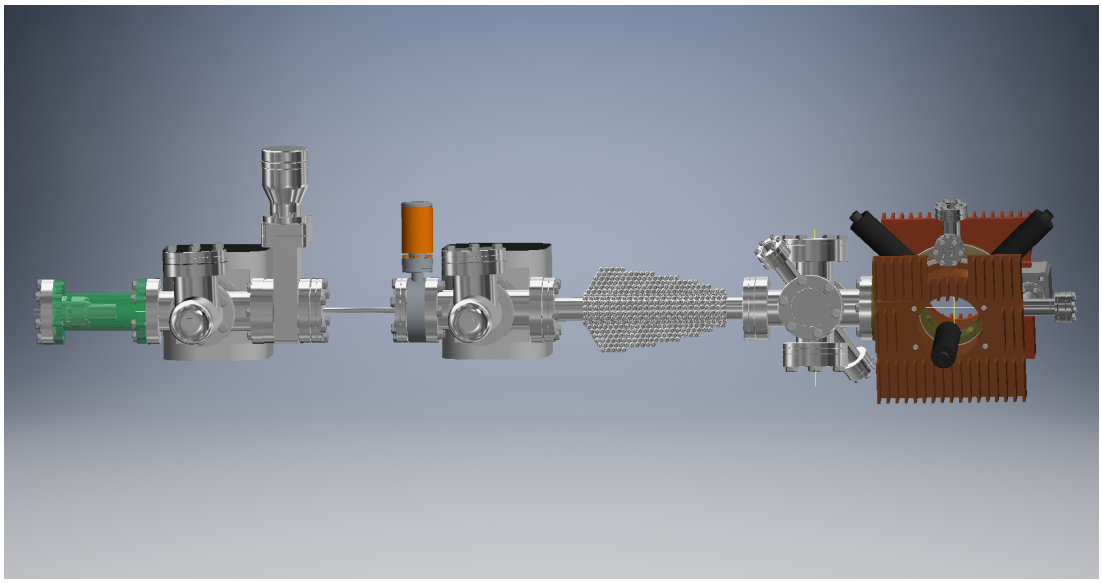

Figure 3.4: CAD drawing of the design of a proposed atomic beam apparatus. The pressure can be maintained in one section of the apparatus if there is a need to break the vacuum in the other section. That can be implemented by adding a valve to the science chamber section in the built apparatus (figure 3.1) and change the positions of the gate valve and the atomic beam shutter.

3.1.3 Differential Pumping Stage

The differential pumping technique is a way to maintain a difference in the pressure between two sections or chambers when they are connected by an orifice or a fine tube due to low vacuum conductance. Producing a high strontium atomic beam flux requires relatively high pressure, while to cool and trap the atoms, one needs to minimize the pressure. By utilizing the differential pumping technique, the pressure in the science chamber is maintained two orders of magnitude lower than the pressure in the oven section. The differential pumping tube itself, shown in figure 3.5, was a 100 mm long custom made stainless steel tube with 4.6 mm inner diameter manufactured by Kurt J Lesker Co. It was connected to the vacuum apparatus by a standard DN 35 CF flange. The pressure difference between the two stages of the vacuum system was estimated by calculating the conductance of the differential pumping tube. The

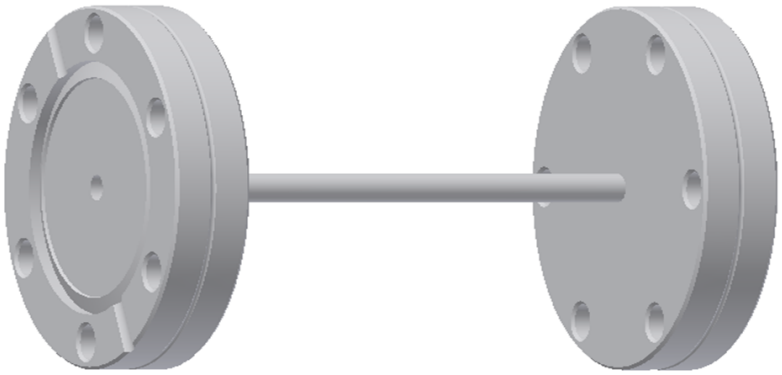

Figure 3.5: CAD drawing for the differential pumping tube (100 mm long and 4.6 mm inner diameter) that was inserted between the oven section and the science chamber to maintain a difference in the pressure between the two stages of the vacuum system (by two orders of magnitude).

conductance, C, of a short pipe or tube of length L (cm), inner diameter d (cm) for molecular flow can be calculated as [118] :

$$C = \frac{d^3 \cdot \pi}{12 \cdot L} \cdot \overline{c} \tag{3.1}$$

where $\overline{c}$ represent mean speed of the particles which can be expressed as:

$$\overline{c} = \sqrt{\frac{8 \cdot R \cdot T}{\pi \cdot M}} \tag{3.2}$$

with R the universal gas constant, M the mean molar mass, and T the temperature in °C. For dry air at T=20 °C the conductance can be written as:

$$C = 12.1 \cdot \frac{d^3}{L}. \tag{3.3}$$

From Eq.3.3, the conductance of the differential pumping tube was $C_{diff} = 0.118$ l/s.

To estimate the pressure difference between the two chambers, one needed to calculate the effective pumping speed for the ion pumps S_{eff}. This depends on the

pumping speed of the existing ion pumps and the total conductance of the science chamber section. As stated above, the science chamber section was pumped by two ion pumps: 25S and 3S with pumping speed of 25 l/s and 3 l/s respectively. The science chamber total conductance C_{tot} is equal to the sum of the conductance of all parts of the science chamber, which included: CF 35 "T" pipe, 22 cm long CF 25 nipple for the Zeeman slower, eight way cross, and finally the science chamber. The effective pumping speed can be calculated by using the relation:

$$\frac{1}{S_{eff}} = \frac{1}{S_{ion}} + \frac{1}{C_{tot}}. \tag{3.4}$$

Eq.3.4 yields an effective pumping speed for the 25S ion pump of 10.56 l/s, and 1.8 l/s for the 3S ion pump. Therefore, the total effective pumping speed equals 12.36 l/s. As a result, the expected pressure difference caused by the differential pumping stage $= \frac{12.36 l/s}{0.118 l/s} = 104$. In addition to the ion pumps, the getter pump contributed to the evacuation of the science chamber.

In practice achieved in the atomic oven section was 10^{-9} mbar with 4×10^{-11} mbar in the science chamber section when the atomic oven is off.

3.1.4 Zeeman Slower

the Zeeman slower was installed after the differential pumping tube to increase the loading efficiency of the MOT by pre-cooling the strontium atoms from the atomic source. The Zeeman slower is composed of spherical permanent magnets. It is composed of two parts: an adhesive layer which acts as a base, whereas the required magnetic field is generated by the fins see Fig.3.1. More information about the Zeeman slower is provided in the next chapter.

3.2 Atomic Package

3.2.1 Science Chamber

The science chamber is the place where the strontium atoms can be cooled, trapped, and probed. When I started work on this project, I had the option to work with a science chamber that had been already used in our laboratory as part of a transportable clock setup, as shown in Figure 3.6b [119]. It has eight orthogonal DN 35 CF flanges around it and one DN 100 CF flange in both sides. Although this chamber offered good optical access I decided to construct a new chamber (as designed in our group) for two reasons:

Chamber size: The width of the pre-used chamber was 110 mm. To generate the required magnetic field gradient for the first stage cooling ($\approx$ 45 G/cm) water cooling had to be used for the anti-Helmholtz coils. That added extra complexity to the system. With a 35 mm width, the magnetic field gradient could be achieved in a new chamber by using a passive heat sink without the need for water cooling.

Chamber material: The material of the pre-used chamber was 316L stainless steel,but a new chamber could be made out of titanium. The benefit of using titanium it being nonmagnetic, light in weight, and it has almost the same thermal expansion coefficient 7.1×10^{-6} K^{-1} as BK-7 8.6×10^{-6} K^{-1}. That meant the quality of the vacuum is less likely to be compromised due to changes in temperature.

The geometry of the new chamber can be seen in Figure 3.6a. It had the shape of an octagonal prism with three pairs of orthogonal optical access flanges (two pairs with 25 mm diameter, and one pair of DN 16 CF flange of 16 mm diameter). In

addition there is one opening for the atomic beam (a DN 35 CF flange to connect it with the vacuum system) and, directly opposite, a DN 16 CF flange providing access for the Zeeman slowing beam. Finally, there were two 70 mm diameter holes, one on either sides, for additional optical access.

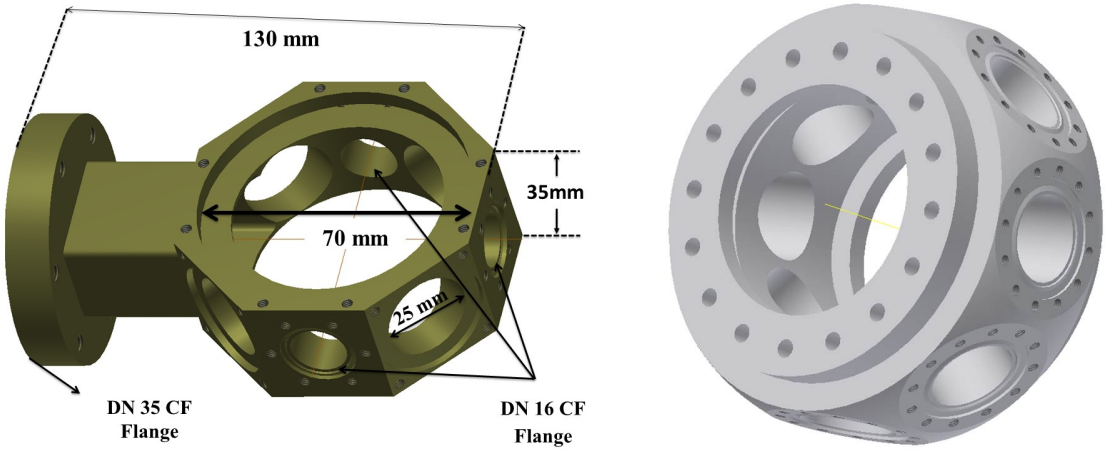

(a) The new science chamber

(b) The old science chamber

Figure 3.6: CAD drawings for the two science chambers that could have been used in the experiment. Although the old chamber (RHS) provides more space for optical access, the new science chamber (LHS) was chosen because of its narrower width (35 mm compared with 110mm), which reduced the power required to generate the magnetic field gradient and remove the need for a water cooling system for the Anti-Helmholtz coils.

Before proceeding with the building of the apparatus it was very important to be confident that the new chamber could provide the necessary optical access for the clock performance which is 461 nm for the first stage cooling, probing and fluorescence detection access, 679 & 707 nm for repumping, 689 nm for second stage cooling, 698 nm for clock laser, and 813 nm for the lattice laser, Fig.3.7 shows the access for all the lasers needed in the experiment.

The optical components used in the science chamber were:

- Four 30 mm diameter $\times$ 3 mm thick BK-7 windows with broadband anti-

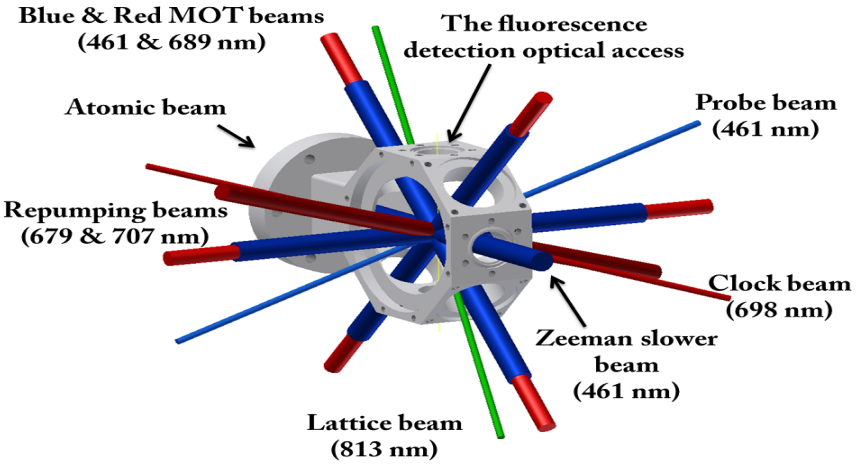

(a) One-dimensional optical lattice with all the lasers and detection access.

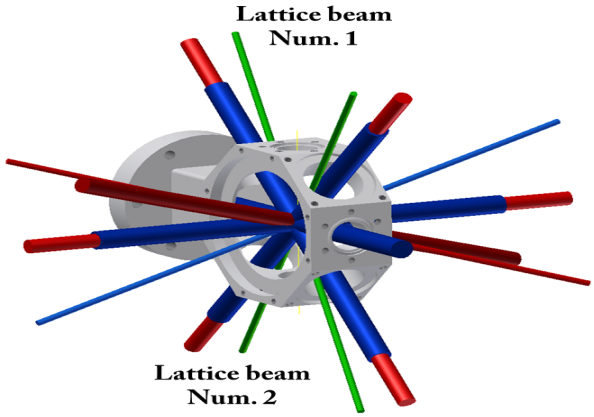

(b) Two-dimensional optical lattice.

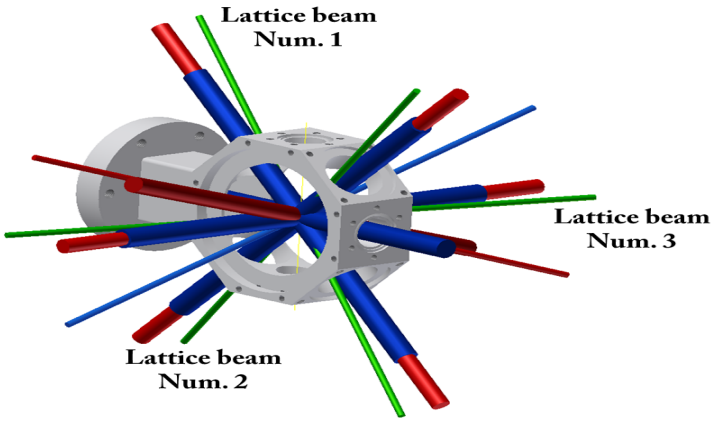

(c) Three-dimensional optical lattice.

Figure 3.7: CAD drawings of the science chamber illustrating configuration optical access for detection, cooling, repumping, trapping, and spectroscopy laser beams.

reflecting coating on both sides (from Diamond Coatings).

- Two 70 mm diameter × 7 mm thick Calcium Fluoride CaF_2 windows with broadband anti-reflecting coating from the outer side and ITO coating from the inside (from Diamond Coatings).
- Three NM 16 CF flange zero length viewports. Two were made from Ko-dial glass with "VAR" Anti-Reflective coatings and one C-cut sapphire viewport with broadband anti-reflective coatings that can be heated to 200 °C (from Torr scientific Ltd).

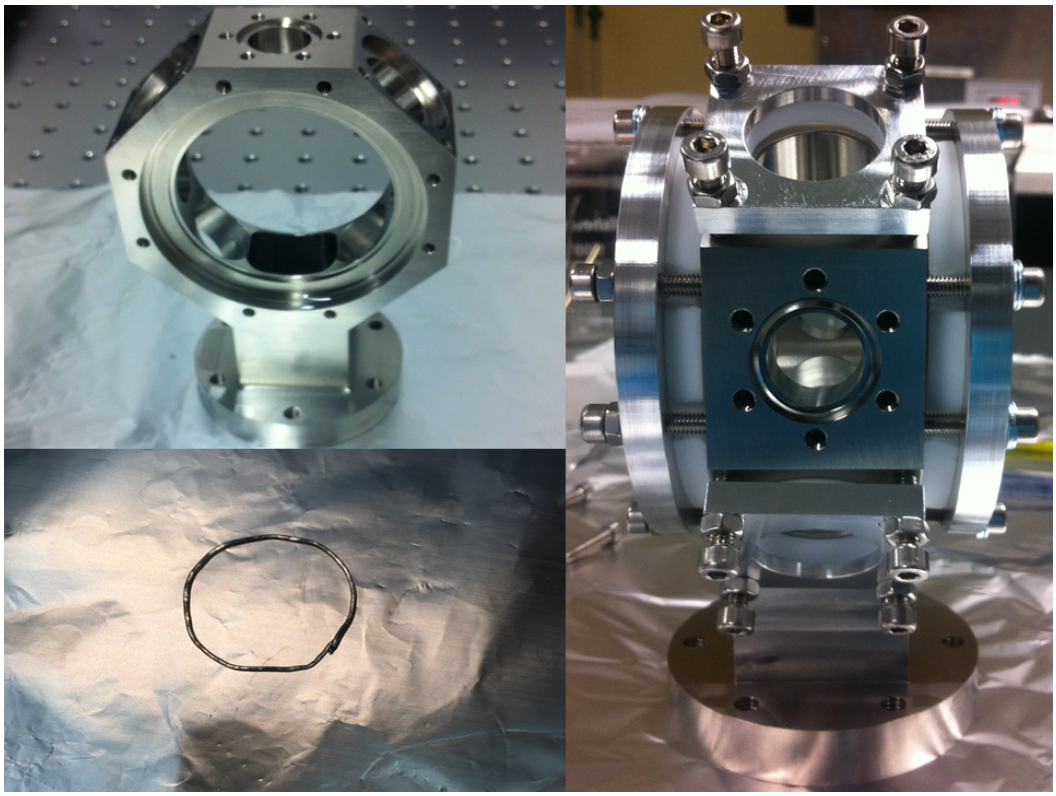

Figure 3.8: Photographs illustrating the securing of the windows to the science chamber using the indium sealing method. Top left, preparing the MOT chamber by cleaning it carefully. Bottom left, the indium wire. right, the chamber when using comprising flange to secure the windows in their position using Teflon.

The windows were attached to the science chamber using the indium sealing tech-

nique. This technique is reliable, simple and fast to achieve. As can be seen in Fig.3.8, to implement the sealing one needed indium wire (from Goodfellow Cambridge Ltd.), a compressor flange Teflon in circular form to cover the window in order not to harm it. First, a ring of indium wire (if the window is circular) was inserted between the chamber surface and the window, then applying a pressure $\approx$ 10 bar for a reasonable time, the sealing was achieved. To ensure good sealing, it was essential to allow sufficient space for the indium wire to expand on the window without obscuring the optical access. In our chamber, from the edge of the window a space of 5 mm was used when sealing the smaller windows (30 mm) and 10 mm with the bigger windows (70 mm). The thickness of the indium wire was 0.5 mm for smaller windows and 1 mm for the bigger ones.

The pressure in the UHV regime can be achieved when the indium sealing implemented correctly. The melting point for indium is about 156 °C, which is relatively low. The advantage of this low melting point is that the window can be replaced by heating the seal to a temperature higher than the melting point. On the other hand, the disadvantage of a low melting point is the temperature limit when heating the chamber to get rid of the impurities inside it, the temperature was kept at $\approx$ 100 °C in order not to melt the indium. Therefore, the chamber had to be cleaned very well and kept as clean as possible prior to sealing the windows.

3.2.2 Magneto-optical Trap Coils and Passive Heat Sink

The magnetic field gradient that is required for trapping the ^{88}Sr atoms can be generated using a pair of coils in an anti-Helmholtz configuration. The $^1S_0$ - $^1P_1$ transition in ^{88}Sr has a 32 MHz linewidth. Such a broad linewidth required a high magnetic field gradient ($\approx$ 45 G/cm) to trap the ^{88}Sr atoms which, in turn, required high

current and power. The width of the atomic chamber and the optical access at its sides determined the separation of the MOT coils and their inner diameter. However, attaching the coils directly to the chamber limit the performance of the optical clock by increasing uncertainty due to the BBR resulting from the coils which induces AC Stark shift. For the Helmholtz configuration, the distance between the coils should be equal to the radius of the coils. To shield the trapped ^{88}Sr atoms from the heat of the coils, I designed a multi-layer shielding unit. It consisted of coil mounts attached to passive heat sinks and two layers from aluminum and nylon. The heat sink 16cm $\times$ 16 cm with 40 fins, each fin is 44 mm $\times$ 2 mm $\times$ 3 mm to increase the surface area, see Fig. 3.9. The generated heat was transferred to the edges of the heat sink by conduction and then dissipated to the surrounding environment by convection, without the need for a water cooling system, see Fig. 3.9. Copper was chosen for its high thermal conductivity of 401 W m^{-1}K^{-1}. Both the aluminium and nylon were 2 mm in thick. Aluminum was chosen for its low emissivity (0.2) which acts to direct the heat away from the atomic chamber (the lower the emissivity the less heat that is radiated by BBR). The second layer of Nylon spacers had an additional function which was to collimate the magneto-optical trap coils as well as to protect the large windows in the science chamber from accidental damage. Therefore, the distance between the coils was increased to 51 mm while the average coil radius was 50 mm.

$R_a = \frac{nd}{2} + r_i$ was the average coil radius, where d was the diameter of the wire, and r_i was the inner diameter of the coil. The magnetic field of the MOT coils along their axis of symmetry was calculated from the Biot-Savart law where the two coils have the same current and number of turns:

$$B = \frac{\mu_0 n I R_a^2}{2[R_a^2 + (x-b)^2]^{3/2}} - \frac{\mu_0 n I R_a^2}{2[R_a^2 + (x+b)^2]^{3/2}}. \tag{3.5}$$

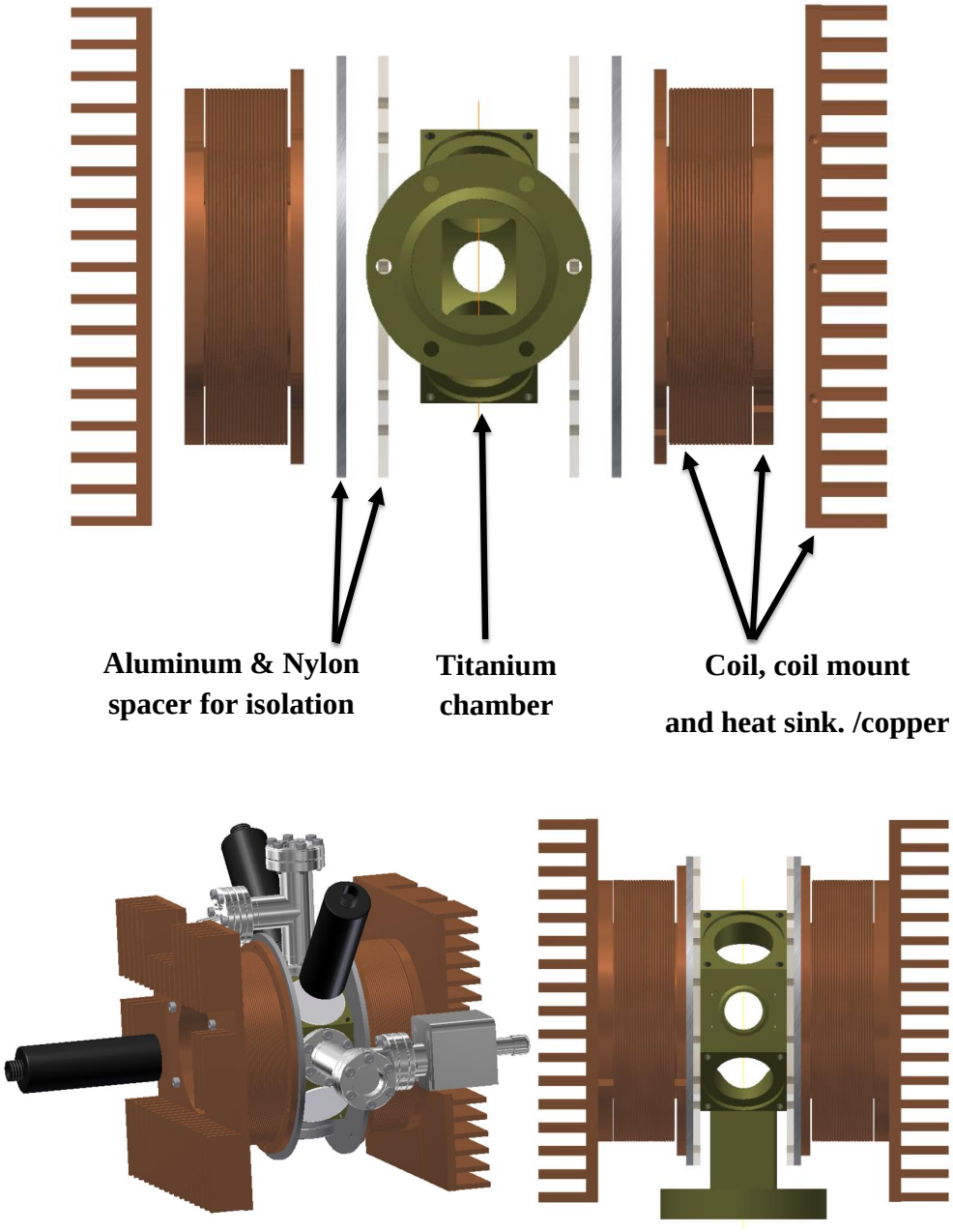

Figure 3.9: CAD drawing shows the design of the coils and coil mounts used to generate the magnetic field gradient for the MOT and the passive heat sink and two layers to shield the strontium atoms from the heat radiated from the coils. Top: is an extended side view. Bottom left : fully assembled atomic package. Bottom right : top view

Where $\mu_0 = 4\pi \times 10^7$ Hm^{-1} is the free space permeability, n is the number of wire turns in each coil, I is the coil current and b is the distance between the coil and the centre of the chamber. The magnetic field gradient can be determind from the derivative of the magnetic field.

The current that required to generate the magnetic field gradient of ≈ 45 G/cm is about 3.5 Amp, when n was 420 turns of enameled copper wire of 1.06 mm diameter. The heat (P) that is dissipated by each coil can be found as:

$$P = I^2 R. \tag{3.6}$$

The resistance $R = \rho L/A$, where ρ was the resistivity of the copper wire, L and A were the wire length and cross-sectional area respectively. The calculated value of P was 27.5 W. which is relatively high. To decrease the temperature of the coils, a fan was used. Fig. 3.10 shows the temperature of the coil mount and the heatsink when 4 A was flowed through the test coils. The temperature was decreased significantly with the aid of the fan. Thus, no water cooling was required for this stage of the experiment, but for the advanced stage, a new solutions could be introduce.

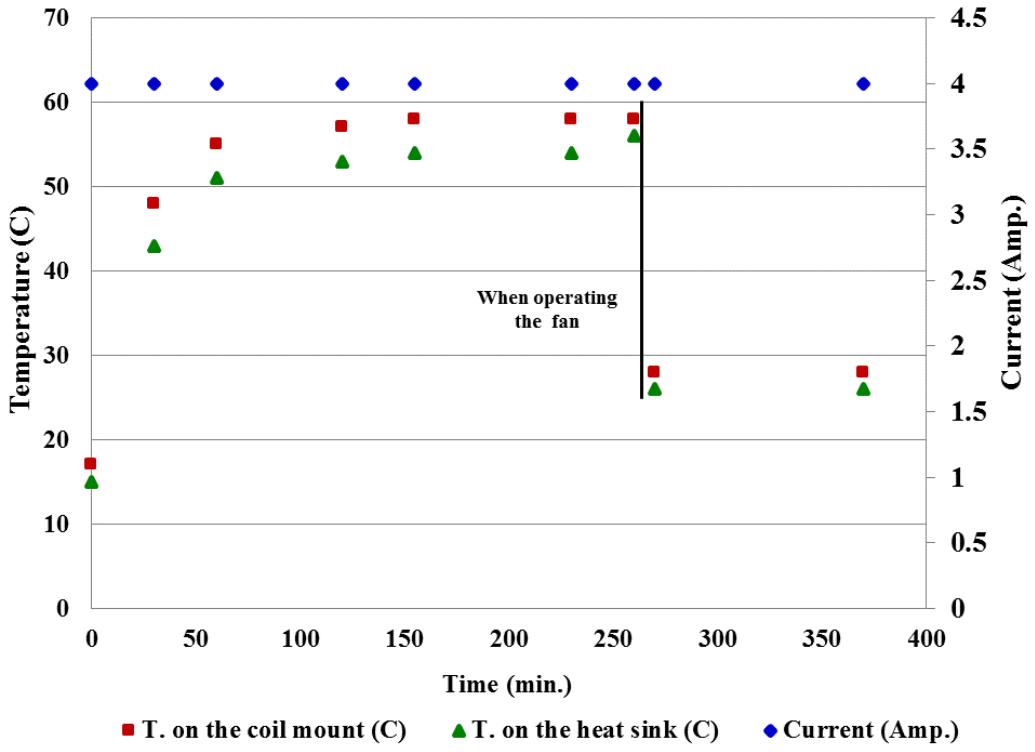

Figure 3.10: Temperature of the coil mount and heat sink with current of 4 Amp. flowing through the coils for almost four hours. The temperature is decreases substantially when using a fan to cool the coils.

3.2.3 Compensation coils

Magnetic fields generated by the earth, magnets in the ion pumps and other laboratory equipment that can exert an influence that contributes to change the position of the atoms in the MOT by shifting their energy levels according to the Zeeman Effect.

The first stage in cooling strontium had a broad transition, and so required a high magnetic field gradient to trap the strontium atoms, which meant the effect of background magnetic field is negligible. However, the second stage cooling has a linewidth of 7.4 kHz. It requires a lower value of the magnetic field gradient ($\approx$ 3 G/cm to $\approx$ 10 G/cm) [120, 121] and beam power to trap the strontium atoms. As a result, the background magnetic field could not be considered as negligible at this

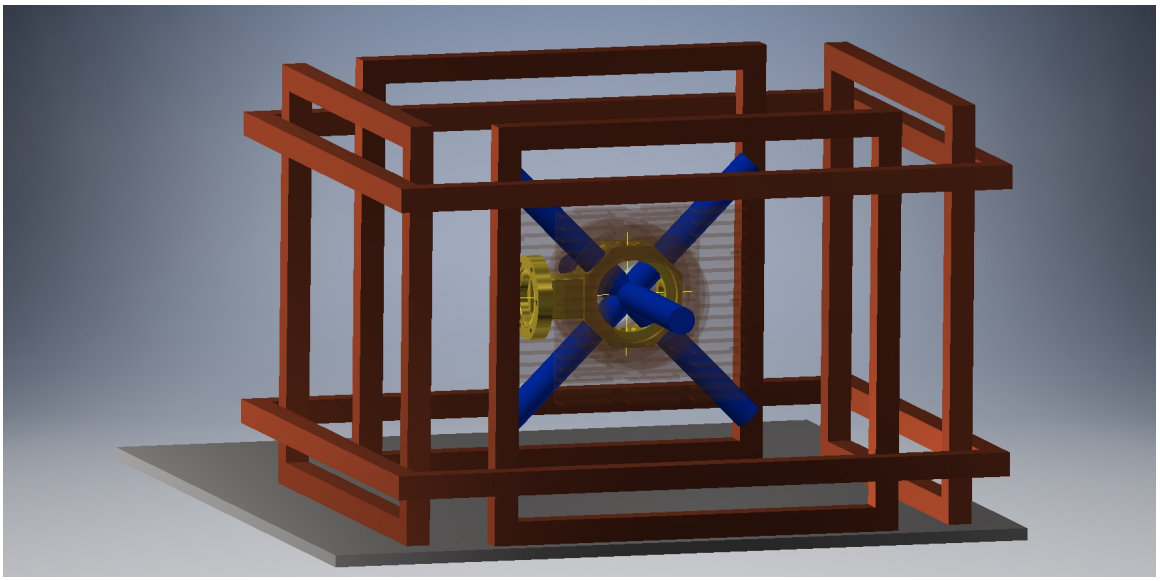

Figure 3.11: The effect of external magnetic field can be compensated for by using three pairs of coils, one pair in each of the x, y and z directions. The effect of the external magnetic field became critical when trapping the strontium atoms in the second stage cooling that uses narrow linewidth transition (7.4 KHz).

phase and could have negatively impact on the loading rate of the atoms and their temperature. Therefore, a set of three pairs of coils was constructed to cancel the external magnetic field in the region of the MOT. Each coil had 90 turns of 1.06 mm thick enameled copper wire wound on a rectangular aluminum frame as illustrated in Fig. 3.11.

3.3 Blue Laser

The 461 nm laser used in the experiment was a commercial Ti:sapphire laser that emits at 922 nm (SolsTiS) followed by an external frequency doubling cavity (SolsTiS ECD-X) manufactured by the M squared company. The 461 nm laser is required in many phases during the the experiment. It is was used to slow down the strontium atom in Zeeman slower and in the first stage cooling. In addition to using it as a

probe for detect the strontium atoms. The output power (up to 500 mW) generated by the laser divided into four paths as illustrated in Fig. 3.12:

- Zeeman slower beam : This beam was used to pre-cool the strontium atoms accelerated by the atomic source. It was shifted by 330 MHz to the read from the fundamental frequency of the $^1S_0$-$^1P_1$ transition using an acoustic optical modulator (AOM).

- First stage cooling beam : This beam was used to trap the strontium atoms in the blue MOT. It was red-shifted by 40 MHz from the resonance frequency, then subdivided into three beams that retroreflected by mirrors.

- Probe beam : This beam can be used to probe the strontium atoms when they interrogate by clock laser.

- The final beam was used to lock the frequency of the laser to the transition and monitor it. By using a PID loop controlled by a wavemeter (WSU2 supplied by HighFinesse) that has a resolution of 500 kHz.

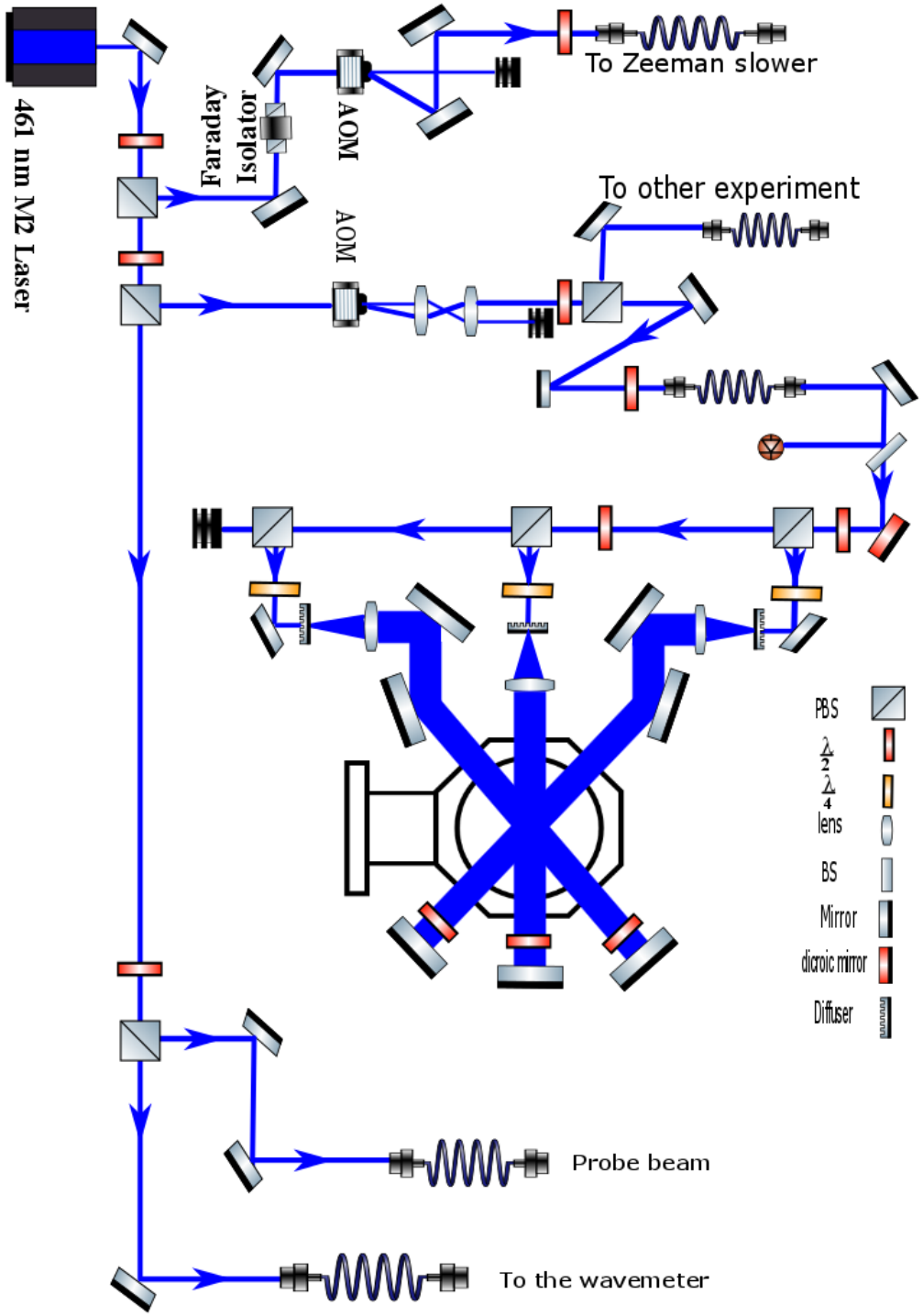

Figure 3.12: Schematic of the optical distribution used in the experiment.

Chapter 4

Zeeman Slower Based on Spherical Permanent Magnets

The initial step in the construction of an optical lattice clock is the production of gas of ultra-cold atoms. The production of such a gas is often aided by a vacuum apparatus (as described in the previous chapter), used to generate a beam of slow atoms utilizing the Zeeman slowing technique. As mentioned in Chapter Two the vapour pressure of strontium is low. However, the atomic flux can be increased by heating the atomic source to temperatures, typically, more than 650 K. At such temperatures, according to Maxwell-Boltzmann velocity distribution, only a fraction of the atoms can be captured directly in a MOT. The Zeeman slowing technique, therefore, is often utilized to increase the MOT loading efficiency by pre-cooling the strontium atoms. An alternative technique to slow down the strontium atoms is by implementing a two-dimensional magneto-optical trap (2D-MOT), but this has a number of disadvantages: Group 2 (elements) species have a common problem with the wavelength of the first stage cooling laser and frequency doubling is often needed to generate the required wavelength. Therefore using a 2D-MOT require

more laser power. Moreover, the loading rate time with 2D-MOT is longer (about 5.5 s) [119] compared to less than 0.5 s [110, 122] with a typical Zeeman slower. This will, ultimately, affect the number of captured atoms in the three dimensional MOT. Furthermore, the 2D-MOT requires additional optical equipment (mirrors, waveplates, optical fibers.) which adds more complexity to the system, especially portable systems. In addition to that, from time to time re-alignment is required.

The first generation setup did use the 2D-MOT to pre-cool the strontium atoms [119]. For the above reasons, the decision was made that the second generation setup would use the Zeeman slower developed by NPL [117]. It was the first time the Ultra-cold Atoms Group at the University of Birmingham built their own Zeeman slower.

This chapter will focus on describing a modified design, and the building and testing of a new type of Zeeman slower based on permanent spherical magnets. The preliminary results obtained during the development of this system are presented. In particular, the performance of the Zeeman slower through measuring the velocity distribution of the atoms at the center of the MOT. Furthermore, the first stage cooling of strontium was realized for the first time with such a Zeeman slower. Up to 6×10^8 strontium atoms were captured and trapped at the early stage cooling with using ≈ 30 mW of 461 nm laser.

4.1 Slowing the Strontium Atoms

The Maxwell-Boltzmann distribution describes the thermal behavior of a cloud of atoms:

$$p(v) = \sqrt{\left(\frac{m}{2\pi k_B T}\right)^3}\, 4\pi v^2 \exp\left(-\frac{mv^2}{2k_B T}\right). \tag{4.1}$$

Where T is the atomic source temperature in Kelvin, m is the atomic mass, k_B is the Boltzmann constant, and v is the speed of atoms. If we consider just the strontium atoms that effuse from the oven, the most probable velocity is given by [123]:

$$v_p = 1.22\sqrt{\frac{2k_BT}{m}} \ . \tag{4.2}$$

Using Eq.2.24 with a 461 nm laser beam diameter of 25 mm, the capture velocity for our MOT is $\approx$ 70 m/s. As a result, the velocity of the strontium atoms is too high to be efficiently trapped directly in the blue MOT. Therefore to pre-cool (slow down) the strontium atoms, a Zeeman slower is installed in the section between the atomic oven and the science chamber, see Fig.3.1.

The general operating principle of Zeeman slowing was discussed in Chapter Two. Here the focus will be more on the passage of the strontium atoms through the slower. The Zeeman slower provides an inhomogeneous magnetic field over the slowing length. When the strontium atoms travel through the applied magnetic field, they will be influenced by the Zeeman Effect which leads to a splitting of the $^1P_1$ state, which in turn, changes their resonance frequency and allows interaction with the Zeeman slowing beam.Changing the magnetic field strength gives the ability to control the resonance frequency of the atomic beam. Therefore, the magnetic field in the Zeeman slower was designed in a way that ensured the change in atomic transition is compensated for by the Doppler shift when the atoms slowed down, such that the atoms and the laser beam that slowing them remain in resonance [122, 124]; thus the magnetic field took the form of :

$$(\omega_L - \omega_o) + k_L v - \frac{(g_e M_e - g_g M_g)\mu_B B(z)}{\hbar} = 0. \tag{4.3}$$

Where g_e, g_g are the Landé g-factor for the excited and ground states respectively, M_e, M_g are the magnetic quantum numbers and $\mu_B = e\hbar/2m_e$ as the bohr magneton

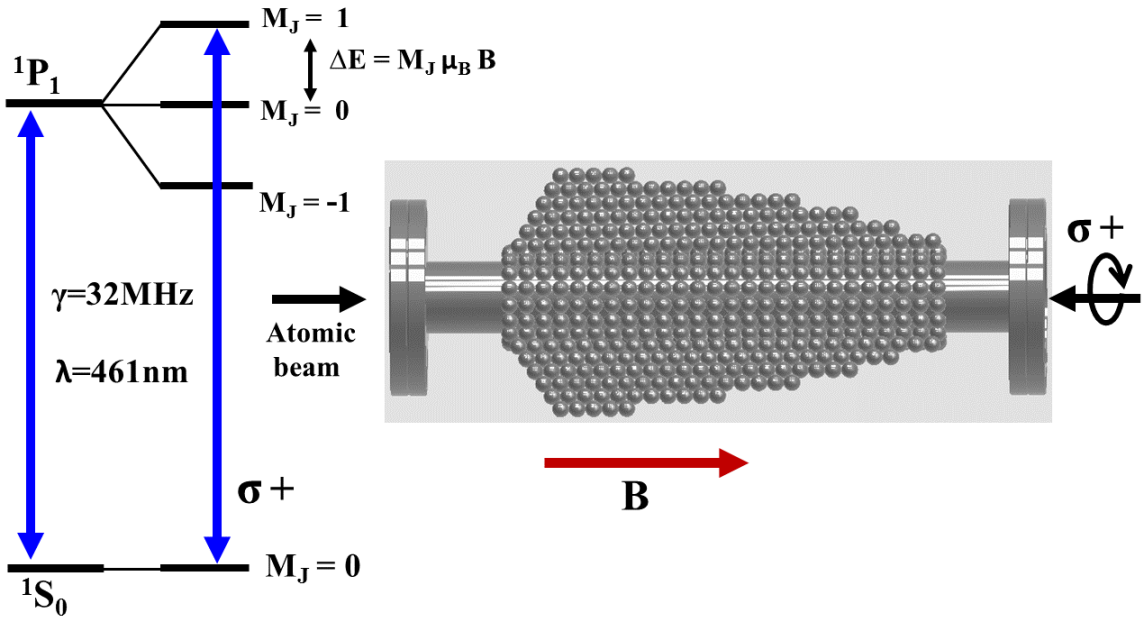

Figure 4.1: A strontium atomic beam is pre-cooled by a 461 nm laser beam with σ^+ polarization. An inhomogeneous magnetic field generated by spherical permanents magnet keeps the atoms in resonance with the laser by splitting their energy levels by $\Delta E = g_J M_J \mu_B B_z$ to compensate for the Doppler shift as the atoms slowed down.

with m_e is the electron mass.

For the ^{88}Sr the nuclear spin is zero. Therefore, the Landé g-factor and the total angular momenta ($J = L + S$) for the ground state ^{1}S$_0$ equal zero, where L and S are the orbital and spin angular momentum respectively. For the first excited state ^{1}P$_1$, the g_J=1 so that the total energy shift into three substates $M_J = 0, \pm 1$ when applying magnetic field $\Delta E = g_J M_J \mu_B B_z$. Fig. 4.1 illustrates the experimental implementation of this concept. Thermal strontium atoms that had been accelerated by the oven are decelerated by a 461 nm counter-propagating laser beam relative to the atomic beam direction with σ^+ polarization.

The maximum force experienced by the strontium atoms (hence the maximum

deceleration) takes place when $\omega_L = \omega_o$. This leads to following equation:

$$\mu_B B(z)/\hbar = \pm k_L v.$$

Using the spatial dependence for the constant deceleration $v = \sqrt{v_o^2 + 2az}$ gives us the ideal magnetic field profile shown in Fig. 4.2, and can be described by the equation :

$$B(z) = \pm \frac{\hbar k_L}{\mu_B} v_o \sqrt{1 - \frac{z}{L_o}} \tag{4.4}$$

where L_o is the length of the slower given by equation 2.14. The above treatment is

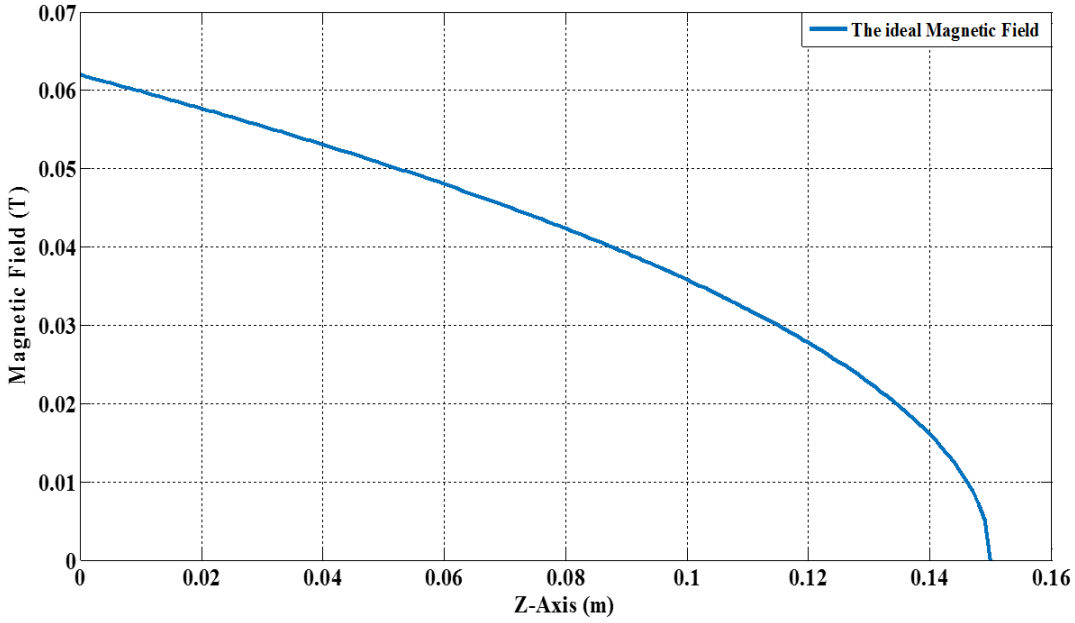

Figure 4.2: The ideal magnetic field shape required to decelerate the strontium atoms from initial velocity $v_o = 400$ m/s to standstill, according to Eq. 4.4. The length of the slower was calculated to be $L_o = 15$ cm.

based on two assumptions: first, the slowing beam intensity (I) is considered to be very high. In practice, however, we speak about laser intensities comparable to the saturation intensity for the cycling transition I_{sat} (see equation 2.9) which is equal to 42.7 mW/cm^2 for the $^1S_0$ - $^1P_1$ in ^{88}Sr. Moreover, the maximum deceleration

which corresponds to a maximum scattering force requires the atoms to be exactly in resonance with the laser at every point through the slower. The slowing process under this condition is unstable because if there is an increase in the velocity of the atoms due to an improper shaping of the magnetic field profile or heating due to spontaneous emission, atoms can be lost from the slowing process which decrease the overall deceleration [125, 126]. Therefore, it is preferable to choose a fractional value for the maximum deceleration $a = \epsilon a_{max}$, where $0 < \epsilon < 1$. According to this, the length of slower is reduced to:

$$L_o = \frac{v_o^2 - v_f^2}{2\epsilon a_{max}}. \tag{4.5}$$

The most probable velocity of the atoms is set by the oven temperature to 400 m/s, and we wish to decelerate the strontium atoms to a velocity of 50 m/s which is within the MOT capture velocity. Therefore, the length of the slower should be 15 cm according to above equation.

With the Doppler shift, the force on the atoms depends on their velocity, and the robustness of the slowing process can be improved by using the value of the slowing force (A), where the derivative has its maximum value. In this case, the optimal value of ϵ can found for the slowing force equal to 0.75 of its maximum value, as shown in Fig. 4.3 where the curve has the steepest gradient. In the real Zeeman slower the magnetic profile may deviate from the ideal, so it is preferable to choose a value lower than 0.75. For our Zeeman slower, ϵ value is set at 0.60.

4.2 Zeeman Slower Based on Spherical Permanent Magnet

The idea behind this type of Zeeman slower is to use spherical permanent magnets to generate a longitudinal magnetic field in a magnetically stable arrangement. The

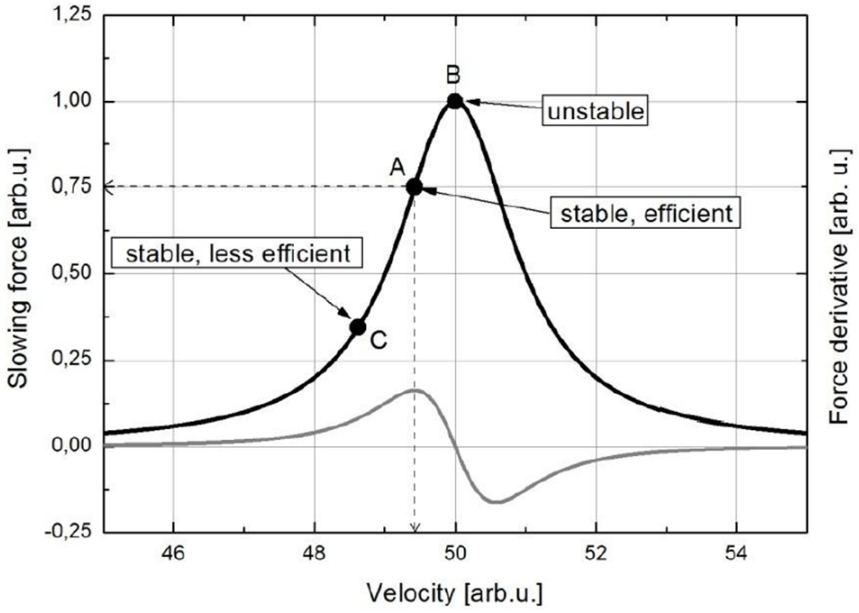

Figure 4.3: The slowing force (black curve) and it is derivative (gray curve) versus velocity of the atoms, with three points indicated: B) where $\epsilon = 1$, the atoms and laser are precisely in resonance; that yields unstable slowing. A) $\epsilon = 0.75$ the derivative of the slowing force has its maximum value; therefore, the slowing is stable and efficient. C) the slowing is stable but less efficient [6].

reasons for choosing this type of Zeeman slower is that it is compact, tunable, easy to assemble, and inexpensive. Moreover, it uses a longitudinal magnetic field that means either σ^+ or σ^- polarized cooling light can be used to drive the atoms to the excited state. Also, it would consume about half the laser power of a transverse slower (this type of slower would need both σ^+ and σ^- to generate linear polarized light) [126]. This consideration becomes very important when working with strontium atoms because few compact laser sources that can generate sufficient power at a wavelength of 461 nm. In addition, the length of the slower would be reduced to half that of the transverse slower. Furthermore, as this design uses permanent magnets to generate the required magnetic field, no power supply or water-cooling is needed, which reduce the complexity of the optical lattice clock. In addition with spherically

shaped permanent magnetic dipoles, the spherical shape is particularly suitable to build the square lattice can be used as an adhesive layer. The adhesive layer is the base that the magnetic dipoles sit on, and if arranged correctly it suppose not to generate any magnetic field.

4.3 Simulation of the Slower Magnetic Field

This work aimed to find a configuration for the magnetic dipoles that assures the generation of a magnetic field profile suitable for slowing down thermal atoms, While minimizing the local magnetic interactions between dipoles. Such an arrangement is referred to as a "self-assembled Zeeman slower" [127]. The required magnetic field profile was generated by the superposition of the fields from each dipole. A single dipole placed at the origin and oriented along z-axis has magnetic field components along the three axes given by:

$$B_x = \frac{\mu_o M}{4\pi}[\frac{3xz}{r^5}]. \tag{4.6}$$

$$B_y = \frac{\mu_o M}{4\pi}[\frac{3yz}{r^5}]. \tag{4.7}$$

$$B_z = \frac{\mu_o M}{4\pi}[\frac{2z^2 - x^2 - y^2}{r^5}]. \tag{4.8}$$

Where $\mu_o = 4\pi \times 10^{-7}$ H/m is the permeability of free space, M is the dipole magnetic moment and $r^2 = x^2 + y^2 + z^2$. In an array of N dipoles symmetrically distributed around the z-axis, the filed components in the x and y-direction will sum to zero along the axis of symmetry, so that the entire field comes solely from the z-component for each dipole. Fig. 4.4 shows the profiles of the magnetic field of a one-dimensional array for different numbers of dipoles: 6, 9, 12 and their sum. Commencing at z = 0, the dipoles were placed in a line parallel to the z-axis and 22 cm away from it. From Fig. 4.4 one can see that increasing the number of dipoles leads to a gradual decrease

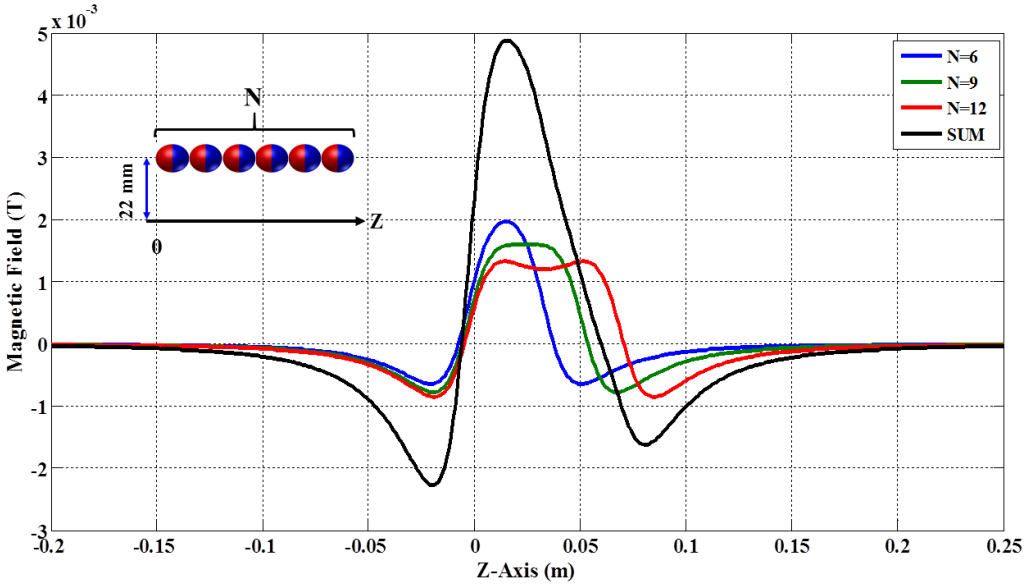

Figure 4.4: The simulation shows the magnetic field profile for a one-dimensional array of 6, 9, 12 magnetic dipoles. The dipoles and their sum. The dipoles start at z = 0 and are placed in a line 22 mm away from the z-axis and parallel to it. The distance between the centres of the dipoles is 6 mm, and the magnetic dipole moment = 0.075 A.m^2.

in the total magnetic field profile. The whole field has an asymmetric pattern which indicates it is suitable to generate the required inhomogeneous magnetic field that can be formed either by varying the number of the dipoles in each array, or by changing the distance of each array from the magnetic axis.

Now the initial parameter to shape the magnetic field profile is known. We could have proceeded to find a magnetically stable arrangement for these arrays of dipoles, but one aim of Zeeman slower is to generate the required magnetic field with a stable structure without using any mechanical or other material support. Efficient atomic beam slowing requires the magnetic field components in the x, y directions to "vanish", so the longitudinal field should vary minimally towards the transverse direction. Therefore, for a stable three-dimensional configuration, the magnetic field has to be symmetric around the z-axis.

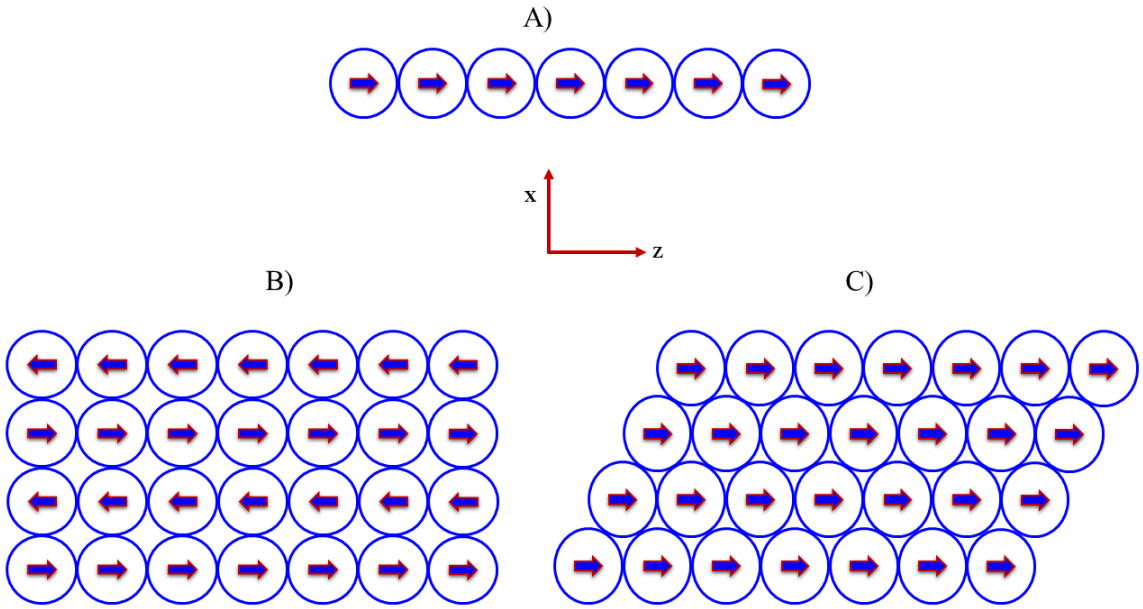

Figure 4.5: Spherical magnetic dipoles in a stable magnetic configuration. A) A one-dimensional array: formed when the south pole in one dipole attaches to the north pole in another dipole. B) A two-dimensional array: formed by aliening the poles of adjacent one-dimensional arrays in opposite directions to each other. This arrangement generates no net magnetic field (square pattern). C) A two-dimensional array: formed by aligning one-dimensional arrays in the same direction as each other (hexagonal pattern).

A stable one-dimensional array can be generated by attaching the north pole of a dipole to the south pole of another dipole to make a chain. As can be seen in Fig. 4.5 (A), a two-dimensional stable arrangement can be created in two ways: first, when two or more one-dimensional arrays are aligned in the opposite direction to each other to produce a square pattern, see Fig. 4.5(B), second, aligning the one-dimensional arrays in line with each other as in Fig. 4.5 (C) creates a hexagonal pattern.

The one, two and three-dimensional patterns of stable magnetic structure can be used to generate the required profile but a stable three-dimensional arrangement is more complicated than the one or two-dimensional configurations. In three-

dimensions it is possible to generate many stable structures, but three-dimensional configurations are highly sensitive to the chronological order in which they are assembled. A chain of the one-dimensional array can form a ring when it is closed onto itself. This ring is stable and has no magnetic field along its axis. Stacking many numbers of these rings, see Fig. 4.6, it is possible to generate two types of cylindrical lattice depending on the orientation of the magnetism of the neighbouring rings:

A "Square cylindrical lattice" see (A) in Fig. 4.6 created when the orientation of the magnets in one ring is opposite to the direction of magnetization in its neighbouring ring. This type is similar to the (B) arrangement in Fig. 4.5.

A "hexagonal cylindrical lattice" see (B) in in Fig. 4.6 can form when the orientation of the magnets is in the same direction as in the neighbouring ring, similar to pattern (C) in Fig. 4.5.

Neither square nor hexagonal patterns (referred to as an adhesive layer) produce a net magnetic field, yet they form an important part of the slower. They are used as a stable solid bottom layer that hosts the arrays of magnets and keeps them in the correct position. The square pattern was chosen to work with because it has a convenient geometry for the spherical magnet arrays to sit on, without the need for any support.

The strength of the magnetic field created by these arrays of spherical magnets can vary with longitudinal and radial positions. In principle, many configurations can generate the required Zeeman slower magnetic field, depending on the application of the slower. I followed the design suggested by [127] because it is a magnetically stable arrangement and symmetric around the z-axis. It was suitable for our application because this arrangement provided the required magnetic field with a minimum number of individual magnets so that the cost and weight remained low. The suggested

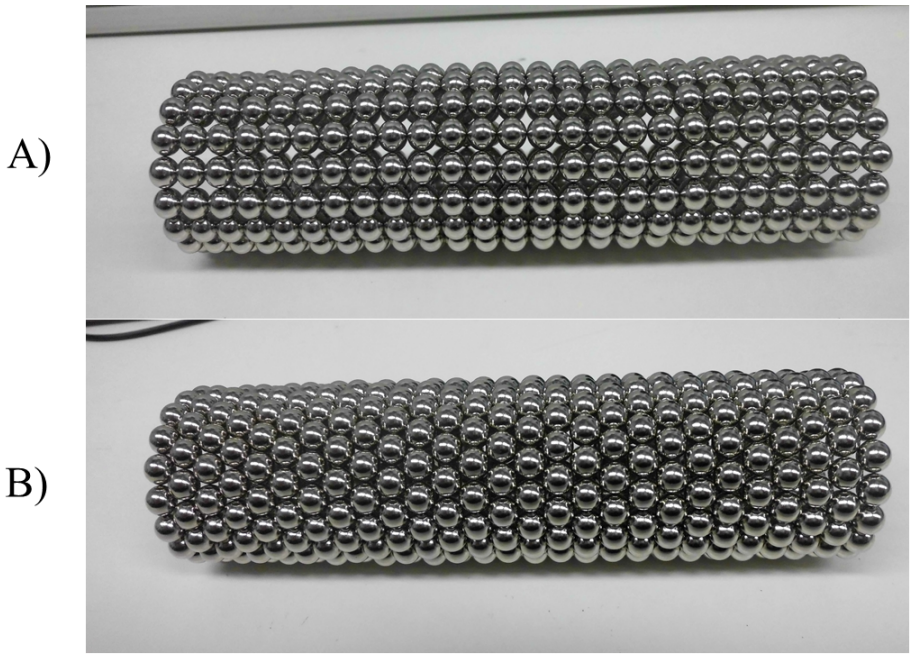

Figure 4.6: Stable magnetic arrangements for cylinder configurations: A)-square pattern: where many rings of one-dimensional dipoles were stacked in the opposite direction to each other. B)-hexagonal pattern where many rings of one-dimensional dipoles were stacked in the same direction as each other.

configuration had three fin-like shapes. All the fins were identical, their magnetic fields pointed in the same direction and they were evenly spaced around the central core as shown in Fig. 4.8a. To this end, we should take a look at how the required magnetic field was generated. To determine how many dipoles were required for each fin, and their distribution, I wrote a MATLAB program to simulate the magnetic field generated by the slower based on Eq. 4.8. Many configurations were simulated to achieve the required profile. Fig. 4.7 shows the simulation of the magnetic profile that is the closer profile to ideal one over the slowing area using N45 grade neodymium iron boride spherical permanent magnets with each having a radius of 6 mm, and a DN 25CF tube. The configuration consisted of five layers in each fin, see Fig. 4.9. The number of spherical magnetic dipoles was varied in each layer, starting with the

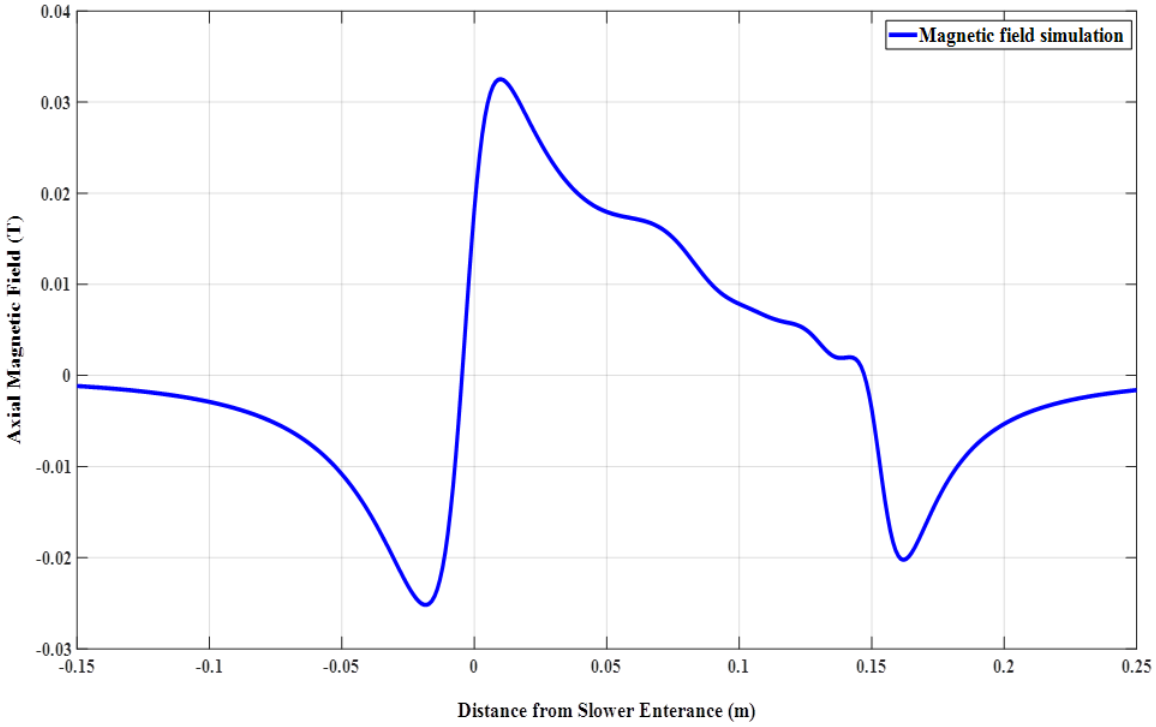

Figure 4.7: Simulation of the magnetic field profile for the chosen Zeeman slower configuration when using N45 grade neodymium iron boride spherical permanent magnets of radius of 6 mm. The configuration consists of three fins; each fin contains five layers. The first, second, third, and fourth layers contain two rows of 26, 23, 19, and 15 dipoles respectively. The fifth layer consists of one row of 8 dipoles. From the magnetic field profile, we can see that the slowing area starts from about zero and continues until 15 cm. The wings of the magnetic field profile can also contribute to slowing the strontium atoms due to the broad ${}^1S_0 - {}^1P_1$ transition in strontium.

most extended layer which has 2×26 dipoles, then the number of dipoles decreases gradually to take the numbers 2×23 in the second layer, 2×19 in the third one, 2×15 in the fourth layer, and 1×8 in the most top layer. However, as the number of layers increased their distance from the z-axis also increased.

4.4 Constructing the Slower

As mentioned in the previous section, it is possible to generate a magnetically stable configuration by adding rows of spherical permanent magnets in a hexagonal pattern on top of either a square or hexagonal cylindrical lattice (adhesive layer). It is also necessary to use the simulation to indicate the typical structure to realize the Zeeman slower magnetic field profile and optimize it. Various configurations were simulated, built, and their magnetic fields measured to assess whether they produced a magnetic field profile close to the profile required to slow the strontium atoms. Fig. 4.7 shows the optimum simulation was obtained, depending on the characteristic of the magnets, the distance between them and the center of the magnetic field axis.

The goal was build a slower that had a profile close to that of the simulation. The magnets used were the N45 grade neodymium iron boride spherical permanent magnets, with a radius of 6 mm, mentioned above. first step was to build a square cylindrical lattice adhesive layer. It consisted of 26 rings; each ring containing 18 magnets in order to give an equal spacing of the three fins so that the symmetry of the magnetic field around the z-axis was maintained. The adhesive layer was wrapped around a non-magnetic stainless steel CF25 tube that had been custom made by the school of Physics/University of Birmingham workshop.

The fin structure was modified in our design, Although the configuration remains the same as shown in Fig. 4.8b. I found it is tough to arrange the dipoles in the same way as described in Fig. 4.8a to obtain the required field profile in a magnetically stable arrangement. It was much easier to utilize the two-dimensional hexagonal pattern to build the fins in order to generate the required magnetic field profile.

Following the simulation, many slowers were built with a different magnet con-

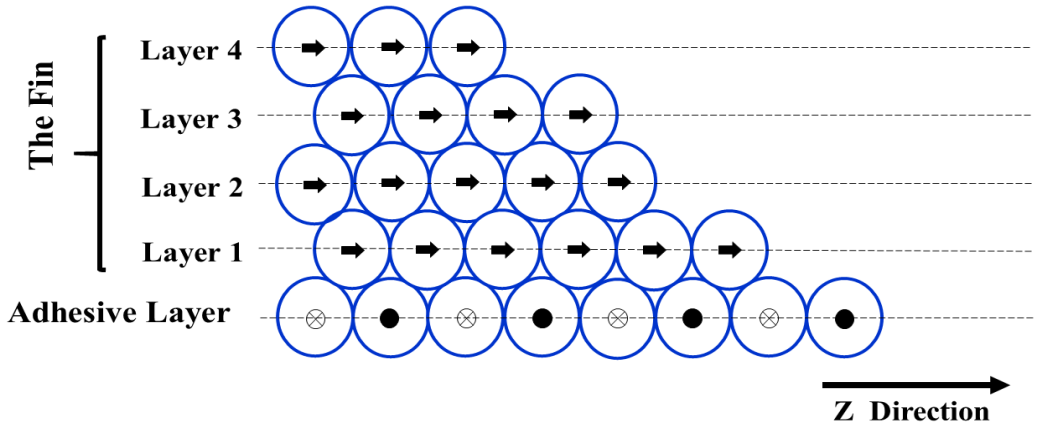

(a) The fin structure (side view) and part of the adhesive layer as proposed in [127]. In practice, it is tough to implement this structure due to the strong interaction between the magnets. During construction dipoles in a layer started to interact with dipoles in other layers. The fin structure was changed because the dipoles would not lie in the correct positions. In turn, the magnetic field profile would be different from the required profile.

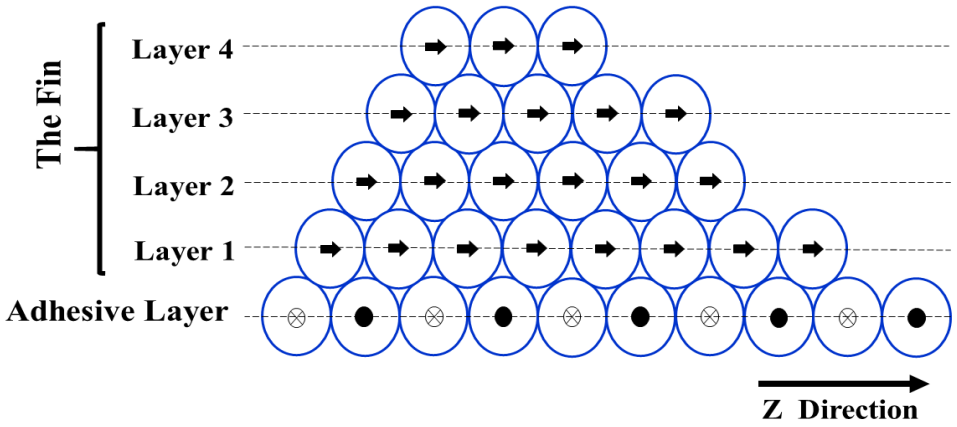

(b) A side view of the modified design for the fin structure in the Zeeman slower, showing part of the adhesive layer. The two-dimensional hexagonal array pattern was used to construct the fin. In this way, it was possible to put many layers on top of each other without the positions of the dipoles changing due to their magnetic interactions. This arrangement generated the required magnetic field, see Fig. 4.9. Three fins could produce a magnetically stable, self-assembling structure for the whole slower. Number of dipoles shown is for illustrative purpose only.

Figure 4.8: Two figures illustrate the difference in the fin structure between the proposed design and our modified design with which it is much easier to construct a magnetically stable configuration.

figurations, and their magnetic fields measured using a Hall probe. The optimal arrangement which exhibits a Zeeman slower-like profile was found to consist of five layers in each of the three fins with dipole numbers being 2×26, 2×23, 2×19, 2×15, and 1×8. The magnetic field in such a configuration is stronger in the bottom layer and then decreases slowly toward the upper layers. The length of the slower was slightly increased by one dipole (6 mm) from the ideal length that calculated from

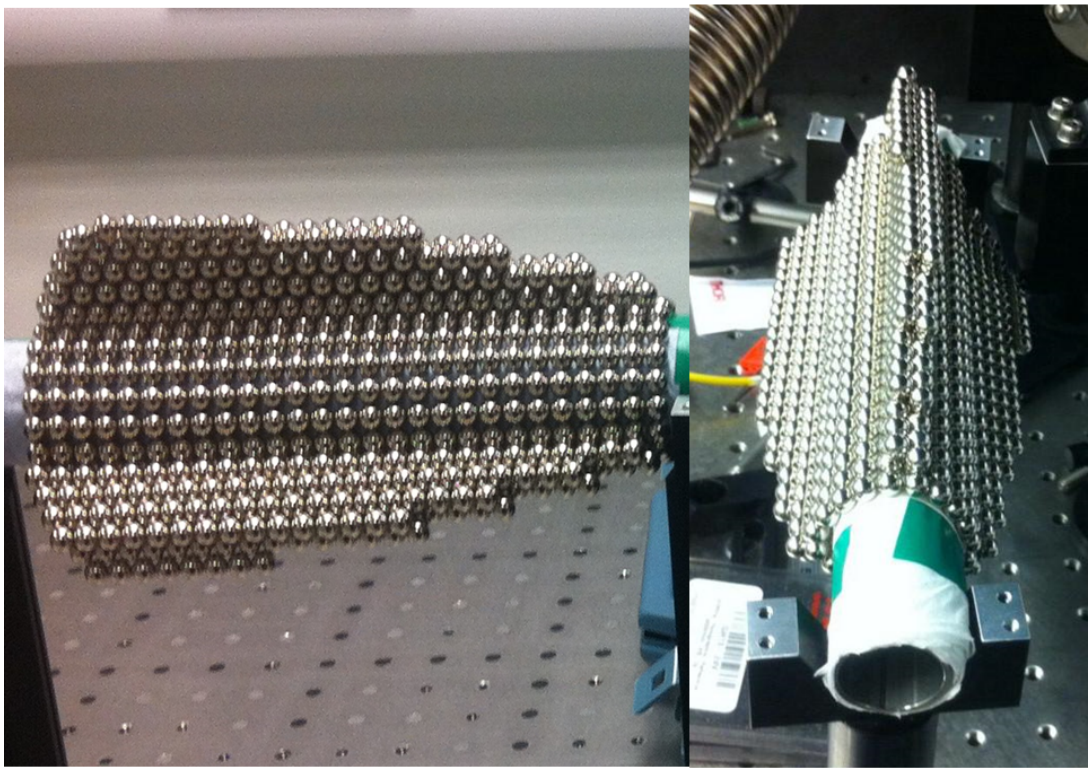

Figure 4.9: The Zeeman slower as built, photos show left side view (left panel), and the top view (right panel). The slower consists of two parts: the adhesive layer and three fins. The adhesive layer is a square cylindrical lattice consisting of 18 dipoles wrapped around the DN 25CF tube. The three fins were arranged symmetrically around the longitudinal magnetic axis to generate the required magnetic field. Each fin had five layers: the first, second, third, and fourth layers had two rows of 26, 23, 19, and 15 dipoles in each; whereas the fifth layer has one row of 8 dipoles. This arrangement generates a better magnetic field profile according to the simulation, see Fig. 4.7.

Eq. 4.4 because with this configuration (26 dipoles) the magnetic field is smoother compeered to simulation using 25 dipoles. Fig. 4.9 Shows the built Zeeman slower. This configuration generates the smoothest magnetic field profile that is compatible with the simulation.

4.4.1 Realizing the Magnetic Field of the Slower

It was necessary to be careful when building the slower because of the difficulties inherent in handling the spherical permanent magnets due to their strong interactions and their sensitivity to structural order. Experience of building several slowers has shown that the following points should be considered when building a slower.

- Opposite fin: All the fins have to be identical in the number of magnets, configuration pattern, and arranged to produce a magnetic field acting in a common direction, i.e. towards the +z-direction in the slower. Fig. 4.10 shows the magnetic field profile of a slower when the magnetic field of one fin points in the opposite direction to the other two.

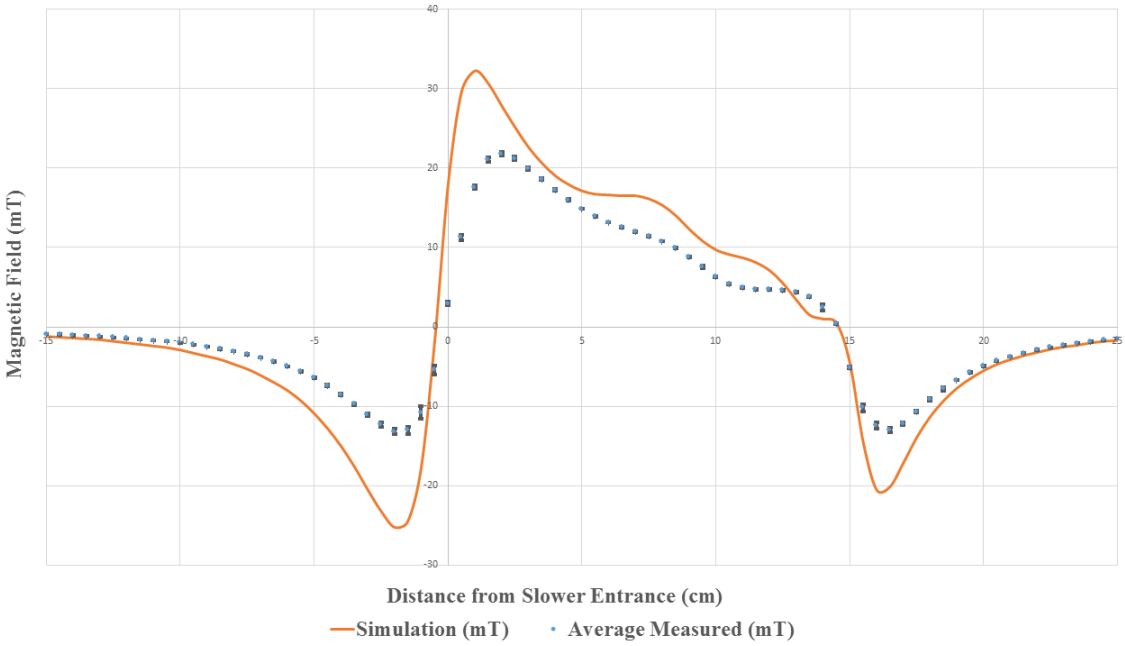

Figure 4.10: The measured magnetic field for a Zeeman slower when the magnetic field of one of the fins points in the opposite direction to those of the other two. The magnetic field has fewer maxima and minima than predicted by the simulation.

- Adding whole fins: the process of adding the fins on top of the adhesive layer

has to be by adding one layer at a time to each fin in order, so that balance was maintained in the magnetic field between the fins and the adhesive layer. Adding a single whole fin directly to the adhesive layer changed the structure of the adhesive layer due to the strength of the magnetic field of that fin; this change was not always discernible to the eye, but it led to distortion of the magnetic field profile of the slower, see Fig. 4.11.

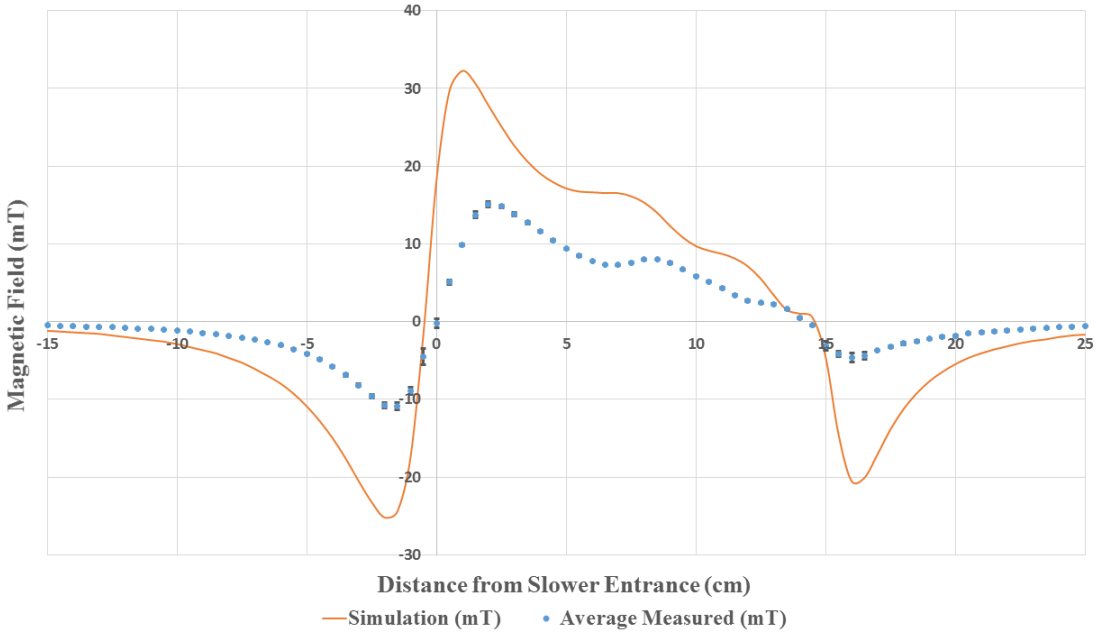

Figure 4.11: The measured magnetic field for a Zeeman slower when adding whole fins that were built separately, directly to the adhesive layer. Due to the strength of a fin's magnetic field, the structure of the adhesive layer will change. The magnitude of the magnetic field dropped to half what it should have been according to the simulation.

- Forming the adhesive layer: see (B) in Fig.4.5, is to make rings by aligning the poles of adjacent one-dimensional arrays in opposite directions (called "perpendicular" because the magnetic field of the fins will be perpendicular to the field of the adhesive layer). Secondly, making a rectangular shape with the magnets then close it on itself (the magnetic field of the fin will be parallel to the adhesive

layer in this case). Fig. 4.12 shows the difference in the magnetic field profile between two slowers, where the adhesive layer built in the two different ways: "perpendicular" and "parallel".

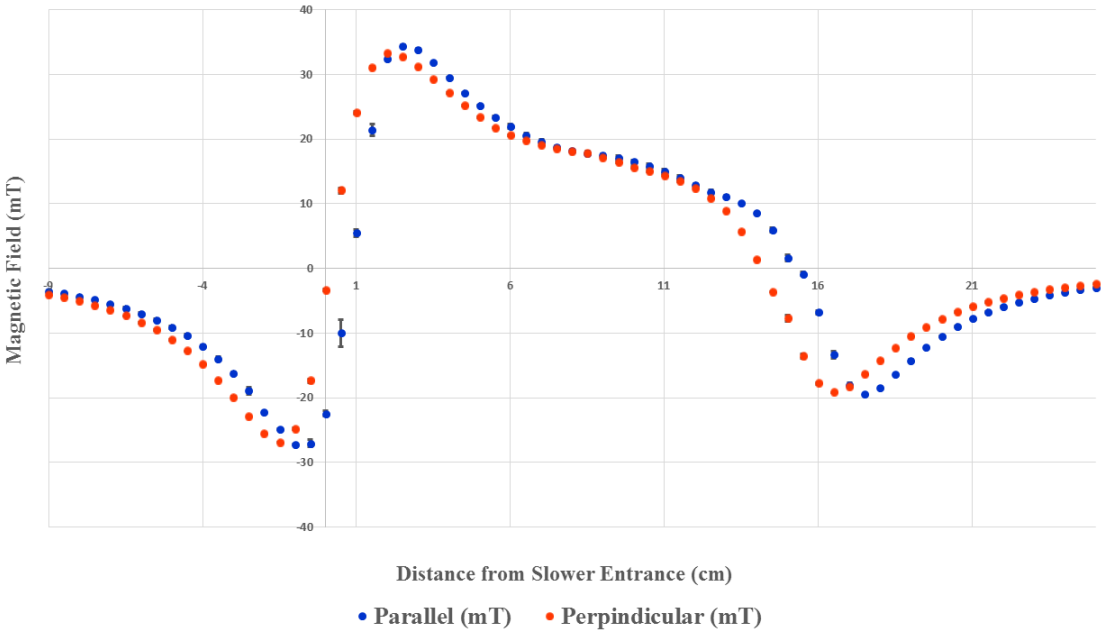

Figure 4.12: The measured magnetic field profile for built Zeeman slower when the square adhesive layer constructed in two different ways. For the parallel profile, there is a contribution from the adhesive layer to the whole magnetic field, whereas the perpendicular profile does not contribute to the entire magnetic field.

It is important to note that every time one build the slower in a wrong way the magnetic field profile and value would change, so the magnetic field profile of the situations mentioned above could not be reproducible.

After all the above issues had been identified and solved, it was relatively easy to reproduce the magnetic field profile consistently, using the above guidelines.

Fig.4.13 shows the measured and simulated on-axis longitudinal magnetic fields. The measured field is not very smooth; the reason could be the physical size of the magnets that have been used (6 mm diameter) or the DN 25 CF tube which has an

outer diameter of 25.4 mm. By using smaller magnets or a bigger tube, the field profile could be improved. The figure shows good qualitative agreement between measured and simulated field profiles, though, the actual field is shifted slightly to the right, possibly caused by a slight movement of the slower or fins on the adhesive layer, as it is hard to keep the magnets precisely in the required positions. Otherwise, measured and simulated fields agree well with each other in shape and magnitude. From the figure, we also see that the slowing length extends from approximately zero to 15 cm, which should provide sufficient slowing of the strontium atoms due to the broad ${}^1S_0 - {}^1P_1$ transition. The magnetic field in the x and y-direction was scanned at the beginning of the slower when the field has its maximum value. The transverse field magnitude was found to be less than 1 mT across the slower, which should not affect the slower performance significantly.

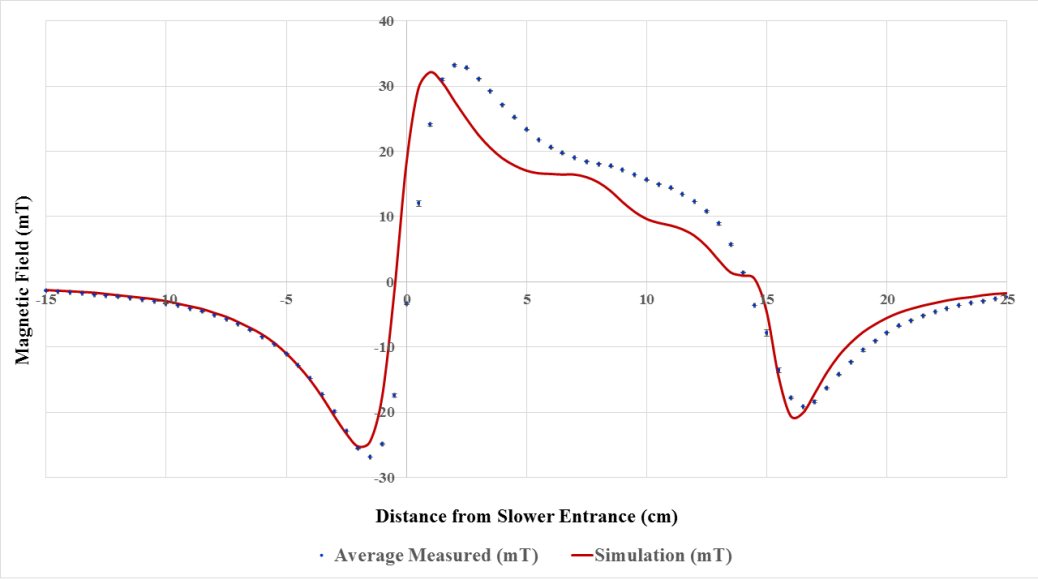

Figure 4.13: Shows the measured and simulated on-axis longitudinal magnetic field profiles for the Zeeman slower. The slowing length starts at around zero and extends to 15 cm. The measured field shows good agreement with the simulated in both shape and magnitude.

4.5 Shielding the Magnetic Field of the Slower

In contrast to the traditional Zeeman slower the magnetic field in the permanent magnets Zeeman slowers cannot be turned off, the longitudinal field of the slower acts permanently along the slowing axis. This is different from a transverse permanent magnet slower where the magnet field decreases to zero after 5 cm from the end of the slower [5]. Thus, there is a possibility that the longitudinal magnetic field can interfere with the magnetic field generated by the MOT coils and adversely affect the number of the captured atoms. In an attempt to prevent this from happening magnetic shielding was used. The basic idea behind magnetic shielding is that the

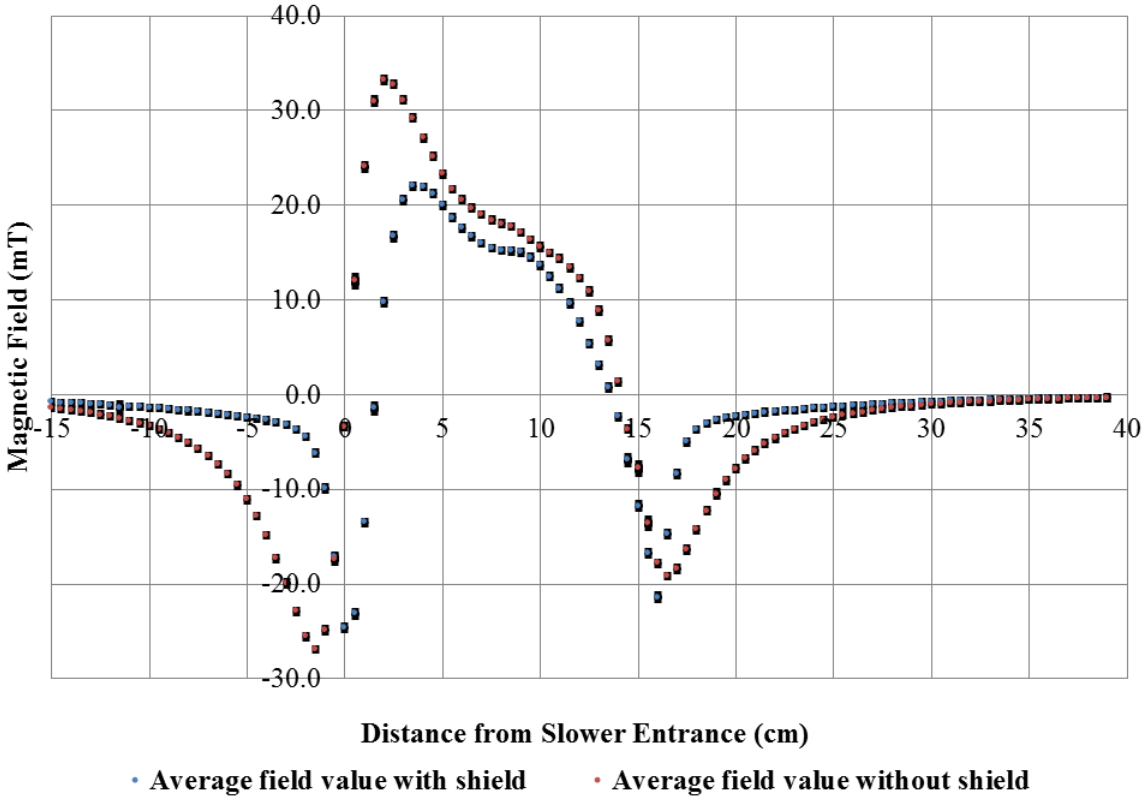

Figure 4.14: The measured magnetic field profile for the self-built slower showing the difference in the magnetic field when the magnetic shields were placed directly on either side of the slower.

magnetic field is directed away from the item being shielded by finding an easier path through the shield material. [128]. In our case, two square plates (6 mm thick × 20 cm × 20 cm) of cast iron were used to redirect the Zeeman slower longitudinal magnetic field away from the area where the MOT was located in order to minimize any perturbation in the MOT. For effective shielding, the shield should be mounted close to the magnetic source. The two cast iron plates were mounted directly before and after the slower. This caused a problem as our slower consisted of permanent magnets in a "self-assembled" configuration without any glue or mechanical mount to hold them. They were attracted to the shields and detached themselves from the slower.

To solve this problem, a 3 mm thick plastic layer was attached to the cast iron plate to prevent direct contact between the slower magnets and the shields, see Fig.4.15(A). Although the plastic layer kept the spherical magnets in position without damaging the slower, the magnetic profile was massively distorted as can been seen in Fig. 4.14, which shows a comparison between the magnetic field profile for the slower without and with shielding placed directly before and after the slower.

From Fig. 4.14 we see that the peak field magnitude has considerably decreased and shifted to the right, with the position of the first minimum squeezing the length of the field. The shields work well at the ends of the magnetic field which decreased sharply, to close to zero, across the MOT area. However, the massive distortion in field profile meant its ability to steadily decelerate the atoms was gone, which made the slower of little use. It was clear that the positioning of two shields, one on either side of the slower was not a proper choice. Subsequently, a single shield was placed mid-distance between the end of the slower and where the centre of the MOT should be, see Fig. 4.15(B). Although the magnetic field profile was recovered, the effect of

the shielding across the MOT area was negligible. Fig. 4.16 shows a zoomed section of magnetic field profiles across the magneto-optical trap area centred at Z = 38 cm for a single shield placed mid-way between the end of slower and centre of the MOT, and the unshielded slower. It is evident that the shielding did not make a significant difference; approximately 1G maximum. It is clear that the shielding effect when the shields were mounted away from the slower were negligible compared with the magnetic field generated by the MOT-which were more than 100 G close to the centre of the MOT. Due to lack of space and the size of the cast iron shield, the decision

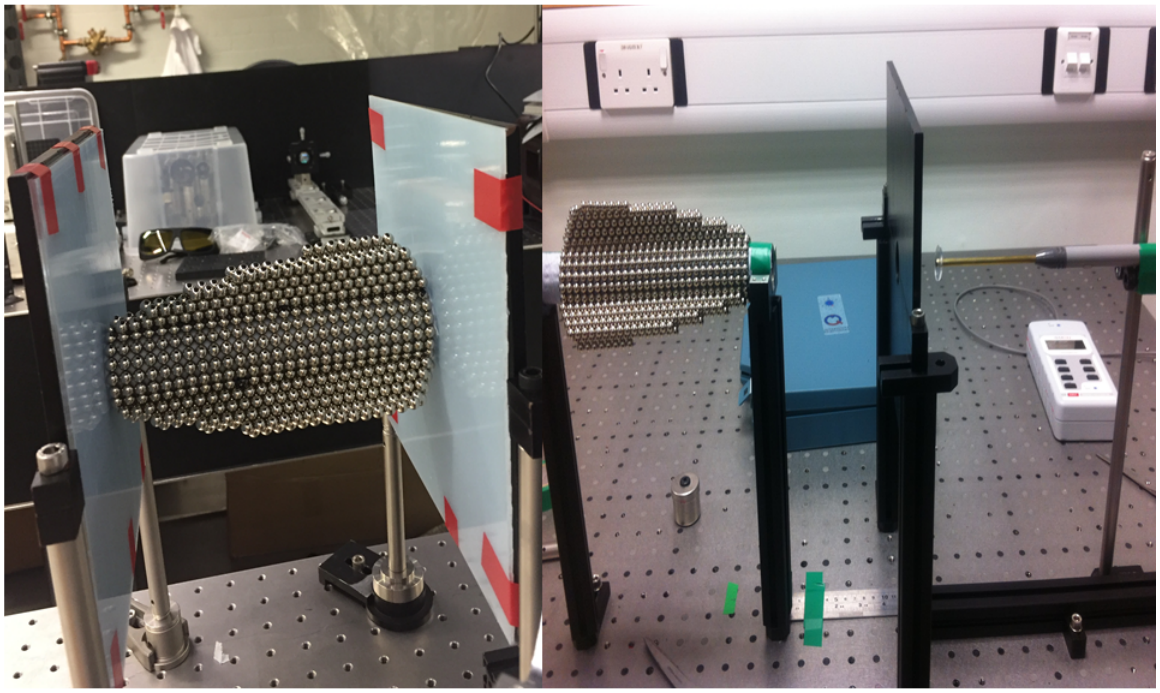

(A) (B)

Figure 4.15: Two photo show the set-up used to measure the slower's magnetic field. (A) The cast iron shield plate was mounted directly before and after the slower. (B) The cast iron shield plate was mounted about 13 cm away from the slower; which is roughly half the distance between the centre of the MOT and the end of the Zeeman slower.

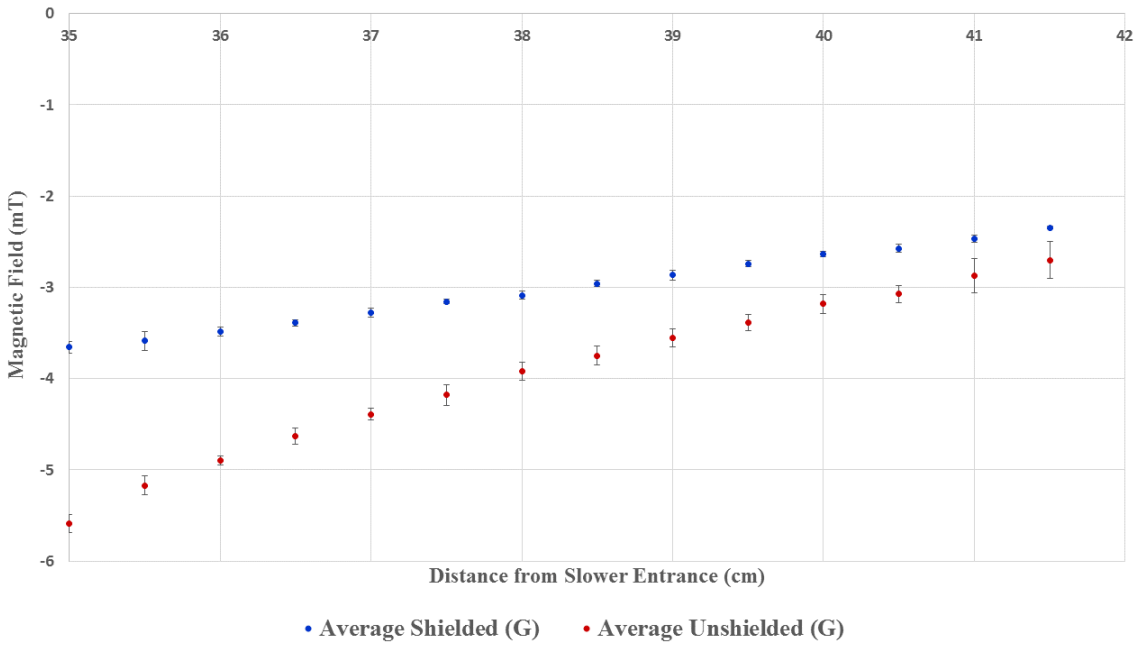

Figure 4.16: Zoomed magnetic field profile across the MOT region of the Zeeman slower in two cases: first, when the shield was placed halfway between the end of the slower and the centre of the MOT. Second, when there was no shield.

was made not to use magnetic shielding.

4.6 The Zeeman Slower Performance

4.6.1 Atomic Velocity Distribution

Strontium atoms that leave the oven will have a Maxwell-Boltzmann distribution with the most probable velocity given by Eq. 4.2. During their travel through the slowing area, the strontium atoms will be under the influence of the Doppler shift $kv = \frac{2\pi}{\lambda}v$ as well as the Zeeman shift $\mu B(z)/\hbar$, where λ is the slowing beam wavelength, and μ is the magnetic moment for the atomic transition which is equal to the Bohr magneton μ_B for the ^{88}Sr atoms. The effective detuning Δ_{eff} at any point through the slower can be obtained from the sum of the laser detuning from the atomic resonance $\delta_L = \omega_L - \omega_o$

and both Doppler and Zeeman shifts:

$$\Delta_{eff}(z) = \delta_L + kv - \mu_B B(z)/\hbar. \tag{4.9}$$

The maximum deceleration is obtained when the effective detuning Δ_{eff} has a minimum value, when the average scattering force experienced by the strontium atoms is given by:

$$F(v,z) = \frac{\hbar k \Gamma}{2} \frac{s_o(z)}{1 + s_o(z) + 4[\Delta_{eff}^2(z)/\Gamma^2]}. \tag{4.10}$$

Where $s_o = I/I_{sat}$ is the saturation parameter. It is equal to the ratio of the slowing beam intensity (I) to the saturation intensity of the $^1S_0 -^1 P_1$ transition I_{sat}. This value was considered constant in our simulation.

From Eq. 4.10 we can see that the scattering force is a function of velocity $v(z)$ and distance z. As Eq. 4.10 cannot be solved analytically, it was solved numerically using the Runge-Kutta-Fehlberg fifth order method. The numerical simulation used the measured longitudinal magnetic field (Fig. 4.13) to simulate the motion of the strontium atoms along the slower and predict their velocity in the centre of the MOT. It showed the change in velocity with constant distance for several initial velocities ranging from 100 m/s to 400 m/s in steps of 25 m/s. The simulation starts from 15 cm before the slower and continues to the centre of the MOT as can see in Fig. 4.17. The maximum capture velocity for the slower was calculated to be 350 m/s, which could be increased by improved the number of magnets in the slower. Strontium atoms with initial velocities less than 170 m/s could not reach the MOT because they were slowed down early and stopped before they entered the slower. Remarkably, atoms kept decelerating even after they had exited the slower, this happened over a distance between 15 - 37 cm, even though the magnetic field had flipped. This phenomenon could have been caused by the strong $^1S_0 -^1 P_1$ transition, which leads

to the presence of a scattering force even with relatively high effective detuning. This also explained why atoms with initially low velocities decelerated too early and were lost. By varying the local saturation parameter and laser detuning, it is possible to maximize the number of captured atoms.

The distribution of the atomic velocity of the strontium atoms was simulated for several slowing beams detuned by -300 MHz to -360 MHz. The result of the simulation are summarized in Fig. 4.17. The change in the slowing beam detuning led to a shift in the range of velocities of the atoms that would be expected to be captured. A slowing beam with greater detuning can slow atoms with higher velocities, but at the same time, there will be a loss of atoms at lower velocities by a roughly equal amount. As the figure shows, when the detuning of the slowing beam is -300 MHz we can capture velocities ranging from 325 m/s to 170 m/s. By increasing the detuning to -360 MHz, then we capture velocities ranging from 350 m/s to 200 m/s. As the function of the Zeeman slower is to increase the loading efficiency, we are interested in the degree of detuning that maximizes the number of captured atoms in the MOT. According to our simulation, the best detuning to achieve that goal is -330 MHz. With this value of detuning, it is possible to decelerate atoms with velocities ranging from 350 m/s to 170 m/s to within the capture velocity of our MOT.

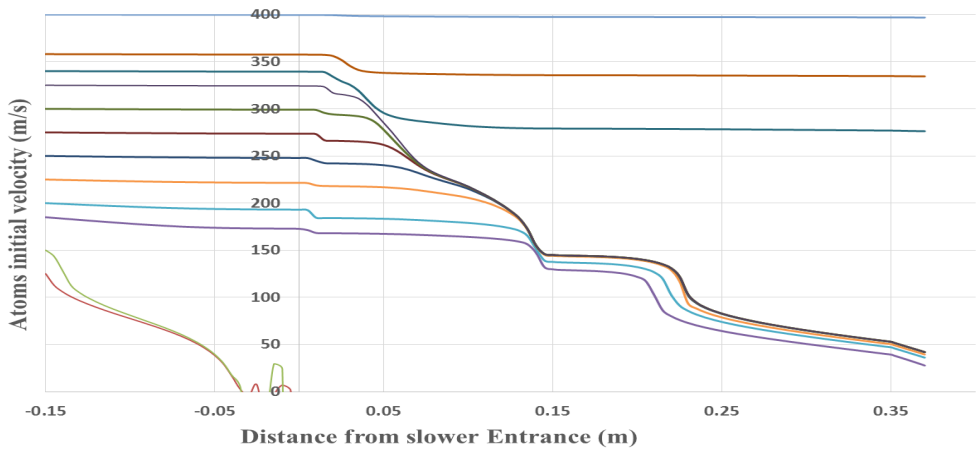

(a) Atomic velocity distribution when the detuning is 300 MHz.

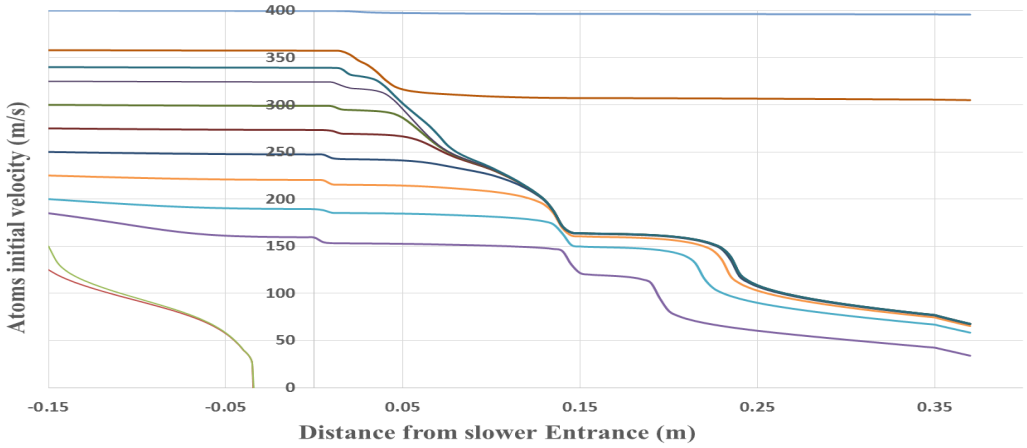

(b) Atomic velocity distribution when the detuning is 330 MHz.

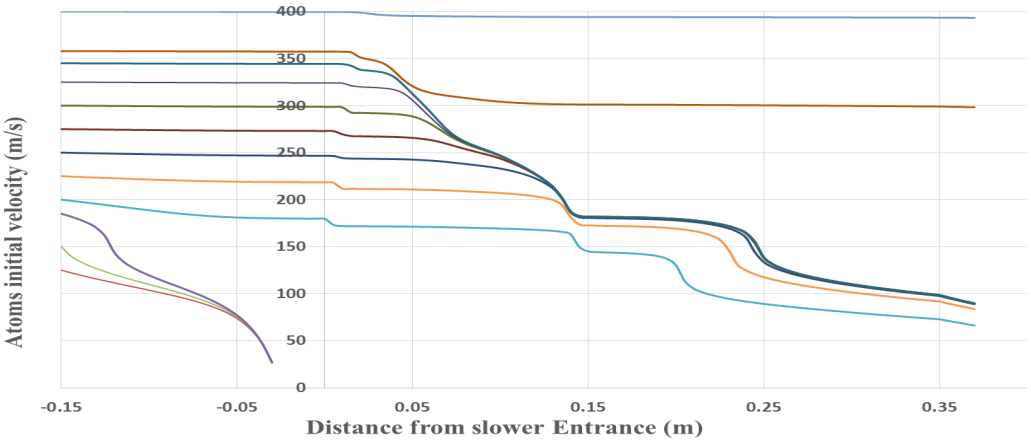

(c) Atomic velocity distribution when the detuning is 360 MHz.

Figure 4.17: Simulation of the atomic velocity distribution across the Zeeman slower, and prediction of the velocity of the atoms in the MOT for different values of slowing beam detuning. The velocity decreases as detuning decreases.

The average velocities in the centre of the MOT for different values of detuning as calculated from the simulation, are summarized in Fig. 4.18. As mentioned above the velocity of the atoms was decreased by decreasing the detuning of the slowing beam. this change is not quite linear. There is a slight difference between the predicted

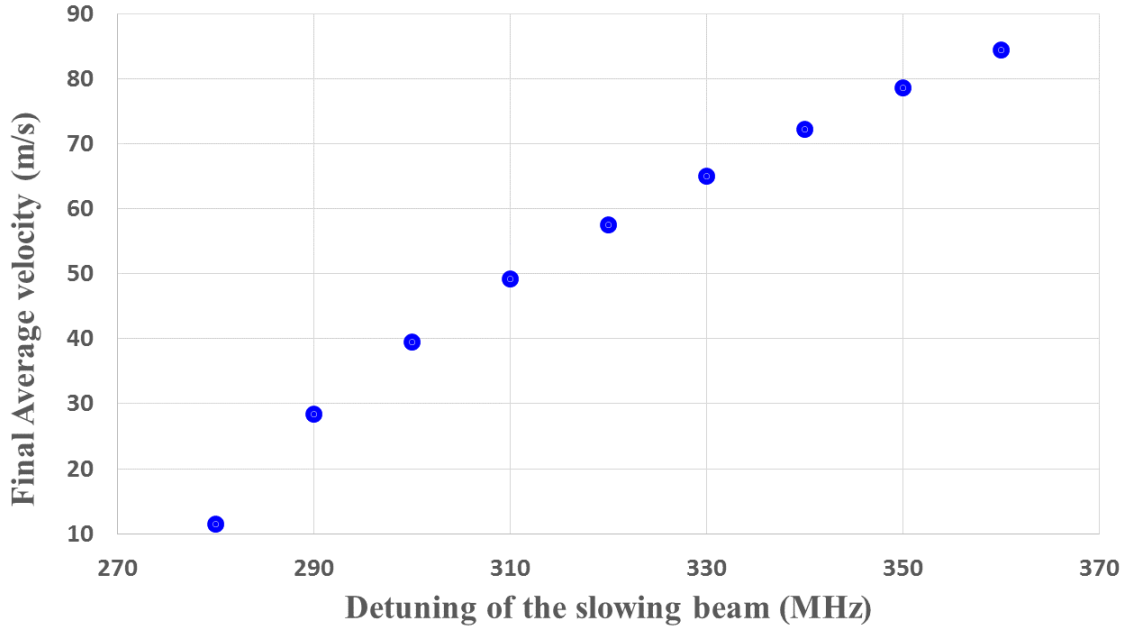

Figure 4.18: Simulation of the average velocity at the center of the MOT for different initial velocities that had different detuning values. The final average velocity decreased as the detuning of the slowing beam decreased.

final velocity and the measured one. The difference may come from the saturation parameter s_o. In the simulation, s_o assumed to be a constant whereas in the actual set-up the Zeeman slowing beam is set to be convergent. A converging laser beam means increasing the optical intensity of the laser (I) with distance towards the oven. This leads to a further increase in the scattering events causing an increase in the radiation pressure on the strontium atoms. This phenomenon could lead to constant deceleration as discussed in Section 4.1 and hence the ϵ parameter was introduced. In our simulation, the slowing process is assumed to start at the point where the

magnetic field was measured, 15 cm away from the entrance of the slower. Scattering events before this distance are ignored. This assumption is valid due to the short distance of simulation, and that the laser was detuned to -330 MHz from the transition resonance. Although, with this detuning, the probability of scattering events in the distance before measuring the magnetic field, will be less, they could still contribute to slowing the strontium atoms and reduce their velocity in the centre of the MOT.

In order to characterize the performance of the Zeeman slower, it was essential to measure the velocity distribution of the atomic beam. Therefore, the longitudinal and the transverse velocity distributions of the atoms were measured at the centre of

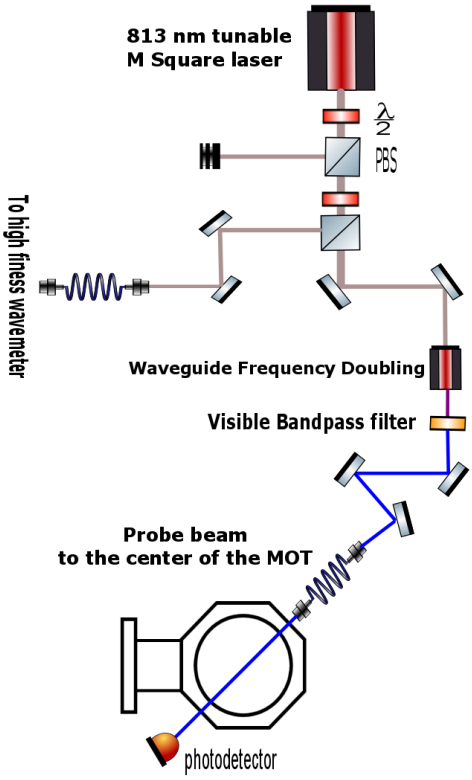

Figure 4.19: The set-up was used to generate the 461 nm probe laser using a commercial fiber integrated wavelength conversion module from NTT. 100 mW of a 922 nm laser light was injected into the waveguide to obtain 20 mW of 461 nm light. The produced light was filtered from the infra-red light using visible bandpass filter.

the MOT chamber. To cover a wide range of velocities in the atomic beam a resonant probe has to scan as much as 2 GHz away from the atomic resonance. The detuning of the Zeeman slowing beam was set to 330 MHz red-shifted from the atomic resonance, so it was not possible to use the same laser to measure the distribution. There was a tunable 813 nm Ti: Sapphire laser (from the M-square company) available. This laser was used to feed a commercial fiber integrated wavelength conversion module from NTT(WH-0461-000-A-B-C) to produce a 461 nm from 922 nm by frequency doubling. Fig. 4.19 shows the set-up that was used to obtain the 461 nm laser beam.

The 461 nm beam probe was delivered to the science chamber by a PM optical fiber and aligned above of the retro-reflected MOT beams' mirrors with an angle of $47\pm2^{\circ}$ with respect to the atomic beam. Fraction of the probe beam was sent to a photodiode to monitor the variation in intensity, and the other fraction transmitted to the atoms. While sweeping the frequency of the laser probe around the atomic resonance, the fluorescence signal was recorded by a CCD camera. Fig.4.20 shows the measured longitudinal velocity distribution when the Zeeman slowing beam had ≈ 30 mW of power, 15 mm diameter, and 330 MHz of red detuning in two cases: 4.20b when Zeeman slower beam on and 4.20b when Zeeman slower beam off. The probe beam had 3 mW of power and was a 3 mm diameter. The atoms were slowed to a velocity less than 60 m/s which was within the capture velocity the MOT. Theoretically, the decelerated atom peak should be sharper and higher, whereas the residual Maxwell-Boltzmann distribution should be flatter. We suggest the reason for this divergence caused by the power broadening; although the probe power was not powerful (3 mW) its diameter was small because it was collimated, thus the saturation parameter s_o

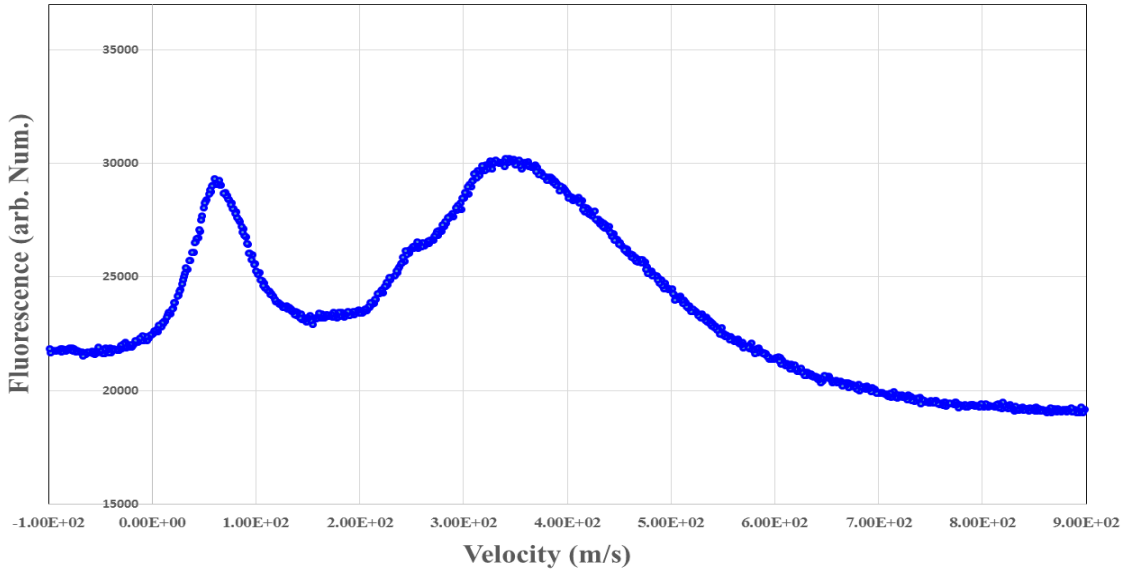

(a) The longitudinal velocity distribution of strontium atomic beam measured at the center of the MOT (after the atoms are exited the slower) showing the effect of the Zeeman slower. The fluorescence signal was recorded with a CCD camera when scanning the resonant 461 nm laser probe. The probe was set to take an angle of 47±2° to the direction of the atomic beam.

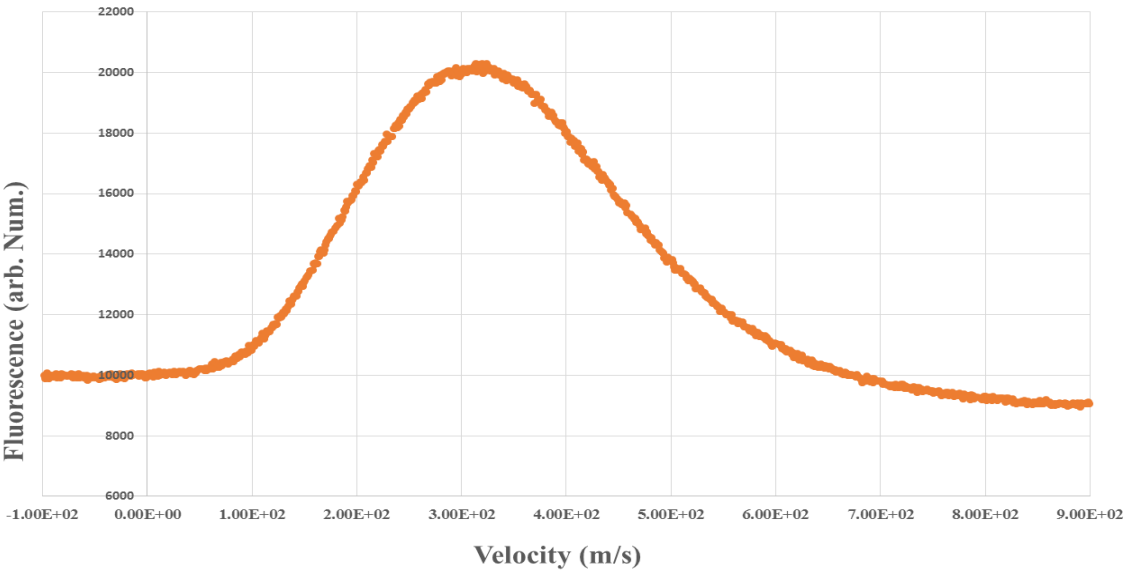

(b) The longitudinal velocity distribution of the strontium for the atomic source measured at the center of the MOT. The fluorescence signal recorded with a CCD camera when scanning the resonant 461 nm laser probe. The probe set to take an angle of 47±2° to the direction of the atomic beam.

Figure 4.20: The longitudinal velocity distribution of the strontium atoms showing: (a) The effect of the Zeeman slower on the atomic beam. (b) The atomic velocity distribution from the atomic source.

had a value of approximately unity, see Eq.4.11.

$$s_o \equiv \frac{I}{I_{sat}} = \frac{P_{probe}/(\pi r^2)}{42.7mW/cm^2} \approx 1. \tag{4.11}$$

That is, the probe intensity was approximately the same magnitude for the saturation intensity of the ${}^1S_1 -{}^1 P_1$ transition which is 42.7 mW/cm^2. Therefore, for this value of the probe intensity, the power broadening is equal to:

$$\Delta\nu = \gamma\sqrt{1 + s_o} = 45.25\ MHz. \tag{4.12}$$

4.6.2 The Atomic Beam Divergence

The atomic beam can be characterized by using orthogonal-crossed-beam spectroscopy when the probe beam is set to an angle 90° to the atomic beam. With this configuration, it is possible to estimate the flux and divergence of the atomic beam. To implement this technique the transit time broadening has to be small compared to the natural width of the relevant atomic transition so the measured line width will not be broadened. The transit time broadening $\Delta\nu_{tt}$ is given by:

$$\Delta\nu_{tt} \equiv \frac{1}{\tau} = \frac{v}{d}.$$

Where v is the most probable velocity of the atomic beam $v = 1.22\sqrt{2K_BT/M}$ and d is the diameter of the probe beam. When the oven temperature is 375°C and the diameter of the probe beam is 3 mm, the transit time broadening is equal to :

$$\Delta\nu_{tt} = \frac{v}{d} = \frac{427m/s}{3 \times 10^{-}3m} \approx 142\ kHz.$$

Which is less than the natural linewidth of the ${}^1S_0 -{}^1 P_1$ transition. The relation between the measured frequency width $\Delta\nu_{tr}$ and the divergence of the atomic beam α is given by:

$$\alpha = \frac{\Delta\nu_{tr}}{\Delta\nu_D},$$

where $\Delta\nu_D$ is the Doppler broadening (given in Equation 2.5), $\Delta\nu_D \simeq 1.26$ GHz when the oven temperature $\approx 375°$C. The frequency width of the ${}^1S_0 - {}^1P_1$ transition measured at the center of the MOT chamber by scanning the 461 nm laser around the resonance of the ${}^1S_0 - {}^1P_1$ transition, the fluorescence signal recorded with a CCD camera.

Fig. 4.21 is the spectroscopic signal showing the frequency width when the probe beam was perpendicular to the direction of the atomic beam. This configuration enables us to determine the resonance feature of the ${}^1S_0 - {}^1P_1$ transition. From Fig. 4.21 we can see that the measured frequency width is less than the shift between ^{88}Sr and ^{86}Sr isotopes ($\nu^{88} - \nu^{86} = 124.5$ MHz) [129]. Thus the signal for each isotope can be detected. The measured frequency width for the ^{88}Sr isotope has FWHM equal to 61 MHz. Therefore the estimated divergence in the atomic beam is:

$$\alpha = \frac{61MHz}{1.26GHz} \simeq 50\ mrad.$$

Fig.4.21 was measured at the center of the MOT chamber without applying the Zeeman slowing beam to determine the resonance frequency (it has been offset by 650.503789 THz and displayed at 0Hz).

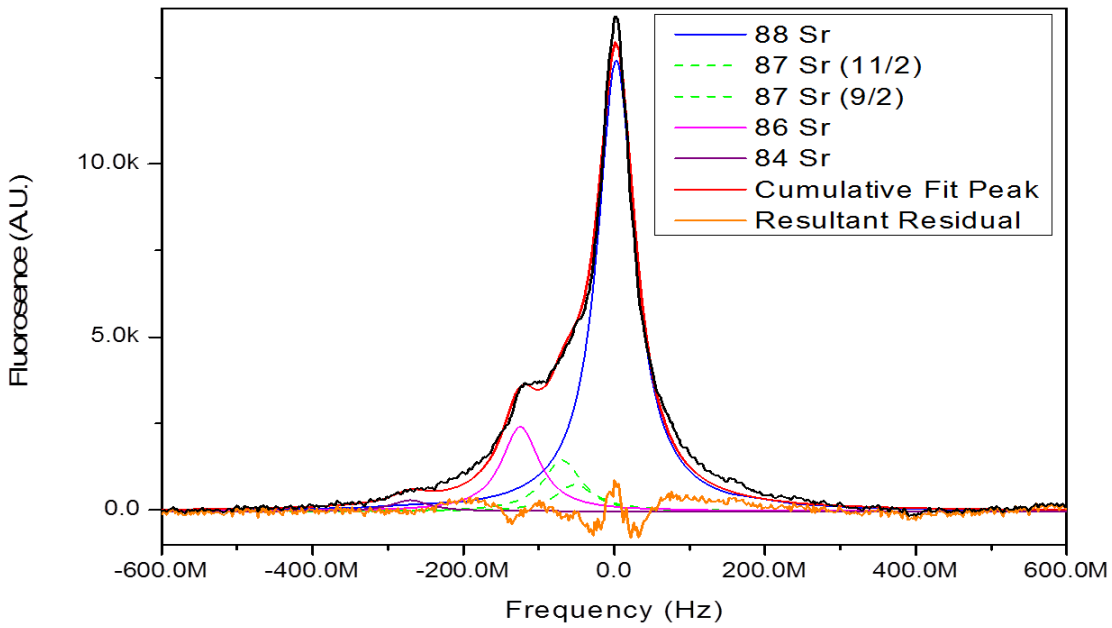

Figure 4.21: Strontium fluorescence signal of the ${}^1S_0 - {}^1P_1$ transition in different isotopes obtained when scanning the blue laser around the resonant transition. The signal recorded with a CCD camera when the probe was aligned perpendicular to the atomic beam direction. Resonance feature of the ${}^1S_0 - {}^1P_1$ transition can be determined with this configuration. Multiple Lorenzian fit function used to identify five peaks (^{88}Sr, ^{87}Sr (11/2), ^{87}Sr (9/2), ^{86}Sr, ^{84}Sr) from the fluorescent spectroscopy using the measured frequency width, the residual of fitting are also plotted with actual spectrum and cumulative fitted spectrum of 5 identified peaks.

4.6.3 Number of Atoms

The illumination from the MOT is an excellent indicator by which to estimate the number of trapped atoms in the MOT. The scattering rate can be utilized to count the number of photons per second emitted from the atoms in the MOT as [130]:

$$R_{scat.} = \frac{s_o \Gamma \pi}{1 + s_o + [2\delta/\Gamma]^2}. \tag{4.13}$$

The saturation parameter s_o and the detuning δ used here were for the MOT beams. The fraction of the emitted photons reached the camera can be calculated as a function of the solid angle of the MOT lens that has a radius r_L at a distance r from the centre of the MOT:

$$f = \frac{r_L^2}{4r^2}. \tag{4.14}$$

The number of photons incident on the camera per second could be expressed as:

$$N_p = \frac{N}{Q.E \times t \times T_L}. \tag{4.15}$$

Where N is the calibration factor of the camera for the low power laser beam, Q.E is the quantum efficiency of the camera for the 461 nm wavelength, t is the camera exposure time, and T_L is the lens transmission factor. The imaging system in our setup consisted of an Andor 5.5 megapixel sCMOS camera that had quantum efficiency of $\approx$ 70 % for the 461 nm wavelength, a 25.4 mm diameter lens with a transmission = 0.75 that away 7 cm from the MOT, and a 25.4 mm radius mirror that reflect the MOT light to the camera. The total number of atoms trapped in the blue MOT could then be found from combining Equations 4.13, 4.14, and 4.15:

$$N_{MOT} = \frac{N_p}{R_{scat.}.f}. \tag{4.16}$$

The number of trapped atoms in the MOT is proportional to the power of the slowing beam to a particular value, after that the number of the trapped atoms will

drop down. The multi-photon effect could be the reason for that. By increasing the density of the atom in the MOT, spontaneously emitted photons from an atom can be reabsorbed by another one. Fig. 4.22 shows the number of trapped atoms in the MOT as a function of the power of the beam when the detuning was fixed at -330 MHz. Due to a limit on the power, Figure 4.22 does not show the maximum value for

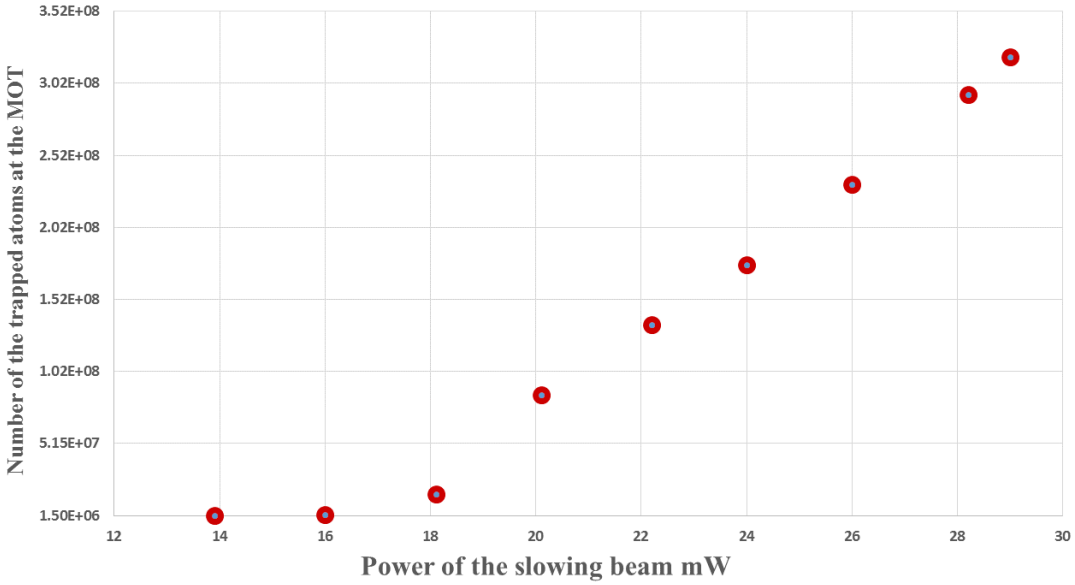

Figure 4.22: The number of the captured strontium atoms in the first stage cooling as a function of Zeeman slowing beam power. The detuning was fixed to -330 MHz.

the trapped atoms. In our laboratory, two experiments are running simultaneously, and there is just one laser so the laser power is divided between them. The light used by the Zeeman slower is shifted to -330 MHz by using an acousto-optic modulator (AOM). Then the laser delivered to the atoms by an optical fiber. In both cases, the coupling efficiency was poor which another reason for lack of power.

4.7 First Stage Cooling

The high velocity strontium thermal atoms that effuse from the atomic oven were slowed down first by a counter-propagating Zeeman slowing beam until their velocities came within the capture velocity of the magneto-optical trap; Then they were trapped at the center of the magneto-optical trap chamber that used the $^1S_0 - ^1P_1$ transition for both cooling and trapping. This was done by applying a magnetic field gradient of ≈45 G/cm and using three retro-reflected orthogonal laser beams of a 461 nm laser.

In this setup, each beam had ≈ 3 mW of optical power and a beam diameter of 25 mm. All three beams were circularly polarized. The frequency of the beams was detuned to the red by 40 MHz from the $^1S_0 - ^1P_1$ transition.The corresponding oven power was 18 W. Depending on the imaging system explained in Section 4.6.3, up to 6×10^8 strontium atoms were estimated to be captured at the blue MOT.

The $^1S_0 - ^1P_1$ transition is not completely closed. Most of the electrons in $^1P_1$ decay back to the ground state, with the expectation that a fraction, 1/50000, of the electrons would decay to the $^1D_2$. From this state electrons might decay to $^3P_1$ or $^3P_2$. Two lasers of wavelengths 707 nm and 679 nm were used to bring the electrons to the ground state. The difference in the number of the atoms trapped in the MOT with and without using re-pumpers could be detected by the naked eye. Fig.4.23 shows a real image for the first stage cooling, the number of trapped strontium atoms was achieved with the aid of the 707 nm and 679 nm re-pumpers lasers, and Fig. 4.24 shows a real image for the blue MOT without using the re-pumpers lasers . The same camera setting was used to take both images.

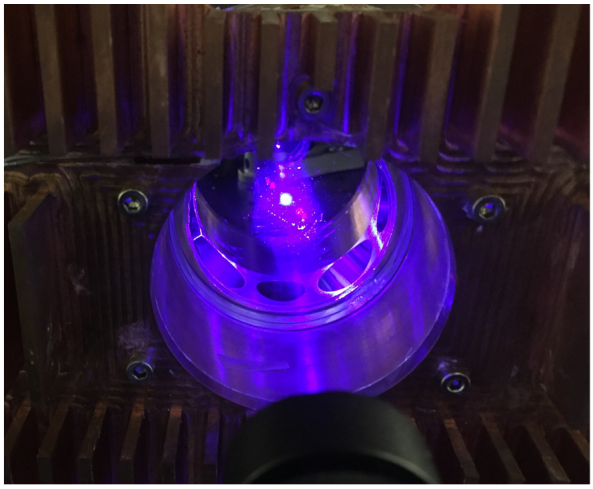

Figure 4.23: A photo of the blue MOT achieved with Zeeman slowing beam of ≈ 30 mW of power, 15 mm diameter, and 330 MHz of red detuning. In addition laser repumpers of wavelengths 707 nm and 679 nm were used.

Figure 4.24: A photo of the blue MOT achieved with Zeeman slowing beam of ≈ 30 mW of power, 15 mm diameter, and 330 MHz of red detuning without using any repumpers.

Chapter 5

461 nm Laser Source

During the first year of my Ph.D., I worked on the frequency doubling cavity as my contribution to the transportable strontium optical lattice clock project. Then the decision was made to establish a Laboratory-base optical lattice clock project. The 461 nm light generated by the frequency doubling cavity was used to realize the first stage cooling with single-beam MOT in a miniaturized atomic package [131], after the atomic package and the laser were ready, the system was delivered to the NPL with the rest of the miniaturized atomic package equipment.

First stage cooling of the strontium atoms, which uses the $^1S_0$-$^1P_1$ transition required a 461 nm blue laser. The Ti:Sapphire lasers can provide power up to 5 W through frequency doubling which is more than enough power to cool the strontium atoms in this wavelength, but the problem with these laser systems lies in their cost and problems with their ability to transport. Until very recently there was no laser diode available at this wavelength. Nowadays some options exist, although they are expensive and typically exhibit low power (<20 mW) and poor beam quality. On the other hand, a MOPA (Master Oscillator Power Amplifier) system can provide compactness, reliability, and transportability. A PPKTP (Periodically Poled Potassium

Titanyl Phosphate) crystal was used to double the frequency of the 922 nm laser inside a monolithic cavity, and to amplify the intensity of the laser light in the cavity. This leads to an increase in the conversion efficiency of the 461 nm output power ($\eta = \frac{P_{2\omega}}{P_{\omega}^2}$), where $P_{2\omega}$ is the power of the second harmonic light and P_{ω}^2 is the squre of the fundamental power that enter the cavity. When the input power at 922 nm was 1 W, up to 300 mW of 461 nm laser light was emitted from the cavity, which provided sufficient power for cooling and trapping the strontium experiment.

5.1 Second Harmonic Generation Theory

Nonlinear Optics is a branch of optics that concern the nonlinear phenomena i.e where the polarization density is not a linear function of the electric field, that arise from interaction of some materials with intense coherent light, for example, some react quadratically with input power, such as second harmonic generation (SHG). In non-linear media many phenomena can be observed such as sum frequency generation (SFG) which occurs when two different frequencies of input waves add together ($\omega_3 = \omega_1 + \omega_2$) to produce a new frequency, and the amplitude of the nonlinear polarization is:

$$P(\omega_1 + \omega_2) = 2\epsilon_o \chi^{(2)} E_1 E_2. \tag{5.1}$$

Where $\chi^{(2)}$ is the second order susceptibility, ϵ_0 is the permittivity of free space and E_1 and E_2 are the electric field of the incident waves which have frequencies ω_1 and ω_2 respectively. A useful application of SFG is the production of tunable radiation in the ultraviolet region of spectrum [132]. Difference frequency generation (DFG) can be generated if there are two optical waves with different frequencies and ($\omega_1 > \omega_2$) input on second-order non-liner crystals, the result is new radiation with a frequency

$\omega_3 = \omega_1 - \omega_2$ [133]. The application of DFG is to produce tunable radiation in the infrared region of spectrum [132]. According to Falkenau a typical threshold that needs to realize such effect is about 2.5 kW/cm^2 [134]. The invention of the laser has opened the door to such phenomena due to its high intensity. The possibility to have a particular, defined wavelength has become possible due to the discovery of second harmonic generation and other nonlinear techniques.

Second harmonic generation can take place when two photons with the same frequency interact with each other and produce a new photon with double frequency [132]. When electromagnetic radiation is incident on a non-linear material and passes through it, the radiation acts to induce dipole moment to oscillation, where a "dipole moment per unit volume" represent the polarization. When the dipole oscillation is close to harmonic oscillation and the light intensity is low the displacement of the dipole will be incredibly small and the approximation can be made that the polarization is proportional to electric field:

$$P(t) = \epsilon_0 \chi^{(1)} E(t). \tag{5.2}$$

Where $\chi^{(1)}$ is the first order susceptibility and ϵ_0 is the permittivity of free space. When the electric field becomes larger the approximation does not hold, and the restoring force is no longer proportional to the displacement, and this where the nonlinearity comes from. In the above Eq. 5.2 the susceptibility is assumed to be independent of the field strength, so χ can be expand as a power series:

$$\chi = \chi^{(1)} + \chi^{(2)} E(t) + \chi^{(3)} E^{(2)}(t) + ... \tag{5.3}$$

Here χ comes from the polarization power series in E [135]. Where $\chi^{(2)}$ and $\chi^{(3)}$ are second and third-order nonlinear susceptibilities and so on.

$$P(E) = \epsilon_0(\chi^{(1)} + \chi^{(2)} E(t) + \chi^{(3)} E^{(2)}(t) + ...)E(t)$$

$$= \epsilon_0(\chi^{(1)}E(t) + \chi^{(2)}E^{(2)}(t) + \chi^{(3)}E^{(3)}(t) + ...)$$

$$\equiv P^{(1)} + P^{(2)} + P^{(3)} + ... \tag{5.4}$$

Suppose there is a monochromatic linearly polarized plane wave, that has frequency ω incident on a nonlinear medium:

$$E = E_o \cos(\vec{k} \cdot \vec{z} - \omega t). \tag{5.5}$$

By substituting this equation into Equation 5.4:

$$P(E) = \epsilon_0\chi^{(1)}E_o \cos(\vec{k} \cdot \vec{z} - \omega t) + \epsilon_0\chi^{(2)}E_o^2 \cos^2(\vec{k} \cdot \vec{z} - \omega t). \tag{5.6}$$

By using trigonometrical identities the above equation can be rewritten as:

$$P(E) = \epsilon_0\chi^{(1)}E_o \cos(\vec{k} \cdot \vec{z} - \omega t) + \frac{1}{2}\epsilon_0\chi^{(2)}E_o^2 + \frac{1}{2}\epsilon_0\chi^{(2)}E_o^2 \cos 2(\vec{k} \cdot \vec{z} - \omega t). \tag{5.7}$$

The first term on the RHS of the equation is the light of the fundamental frequency ω, the second term is the optical rectifier which is an electrostatic field found across the second-order crystal. The third term is the second harmonic generated with frequency of 2ω.

$$P^{(2)} = \epsilon_0\chi^{(2)}\frac{1}{2}E_o^2 \cos 2(\vec{k} \cdot \vec{z} - \omega t). \tag{5.8}$$

The incident light induces a nonlinear response in nonlinear materials, which leads to an additional frequency component. Each atom in the nonlinear material will respond to the nonlinear polarization with an oscillating dipole moment with new frequency (2ω), and which will exhibit dipole radiation. The radiation from each dipole will interfere with each other, either destructively or constructively; the system should be designed in such a way that the atoms radiate in phase. Maxwell's equations can be used to derive the optical wave equation that describes the behaviour of a travelling wave through the nonlinear media, starting with displacement current $\vec{D} = \epsilon_0\vec{E} + \vec{P}$,

where $\vec{P}$ depends nonlinearly on $\vec{E}$ (for more details see [132]), assuming the medium is lossless and dispersionless:

$$\nabla^2\vec{E} - \frac{\epsilon_r^{(1)}}{c^2}\frac{\partial^2\vec{D}^{(1)}}{\partial t^2} = \frac{1}{\epsilon_0 c^2}\frac{\partial^2\vec{P}^{NL}}{\partial t^2}. \tag{5.9}$$

using $c = \sqrt{\mu_0\epsilon_0}$.

This inhomogeneous wave equation describes the relationship between the response of the second derivative of the nonlinear polarization to the electric field, and indicates that changes in the polarization (the acceleration of charges) causes the dipole to radiate at a new frequency, and produce a new frequency component of the electromagnetic radiation. The right-hand side of the equation which is the second derivative of the time-dependent nonlinear polarization acts as a source for the electromagnetic field that accelerates the charges. The acceleration makes the dipole oscillate at the second harmonic frequency. As stated before: to maximize the efficiency of second harmonic generation and keep extracting energy from the incident wave, the phase matching condition has to be satisfied:

$$\Delta k = k_2 - 2k_1. \tag{5.10}$$

Where k_2, k_1 are the wave numbers of the second harmonic and the fundamental respectively. The maximum intensity can be achieved when $\Delta k = 0$, this minimizes the destructive interference between frequency conversions that take place at different location along the crystal length. If the phase match condition is fulfilled the refractive indices for input and output wave have to be the same:

$$n_w = n_{2w}. \tag{5.11}$$

This condition usually cannot be achieved in an isotropic material, but birefringence media can be used to satisfy the phase matching condition because this material has different refractive indices for different axis.

Phase matching is usually fulfilled in three ways:

Critical phase matching: The crystal axes have the capability to make both the refractive indices equal for both beams, so their velocities can be made equal if the crystal axis is carefully chosen.

Noncritical phase matching: Because the refractive indices change differently with temperature, the crystal temperature should be adjusted to a point where both refractive indices are the same for the two beams. The temperature required to achieve this technique can be in the range of a few hundred degrees.

Quasi-phase matching: QPM can be realized by periodic poling of the crystal, that leads to reorientation along the axis of the crystal, therefore the sign of the nonlinear coefficient d_{eff} can change periodically as a function of position along the crystal length. In QPM. the coherence length is optimized in a way that makes the fundamental power get more conversion, but the matching does not actually take place .

5.2 Monolithic Second Harmonic Cavity

As stated previously, the frequency of a light that pass through a non-linear crystal can be doubled by implementing the second harmonic generation (SHG) process. A single pass of a continuous laser beam leads to limited SHG conversion efficiency because the conversion efficiency is proportional to the square of the power of the fundamental frequency:

$$P_{2\omega} = \eta P_{\omega}^{2}. \tag{5.12}$$

For common crystals: LBO, BBO, BiBO, KTP,$LiNbO_3$, PPKTP, and PPLN the η = 0.01-2%/W.cm. The conversion efficiency can be improved by placing the crystal

inside an optical cavity. Eq. 5.12 shows that if the power of the fundamental, P_ω, was enhanced by factor of 50, the SHG power $P^2_{2\omega}$ would increase by a factor of 2500 compered to the single pass SHG [136].

Many parameters should be considered when designing a cavity, two are particularly important: the waist of the fundamental beam and the transmission of the coupling mirrors. Focusing the fundamental beam enhances the intensity at the focus, but that is at the expense of lowering the intensity away from the focus. The compromise between the length of the crystal and intensity was studied by Boyd and Kleinman [7]. They suggested an optimum value for the focusing ratio was L/b =2.84, see Fig. 5.13, where L is the length of the crystal, and b is confocal parameter which is given by:

$$b = \frac{2\pi\omega_o^2}{\lambda n}. \tag{5.13}$$

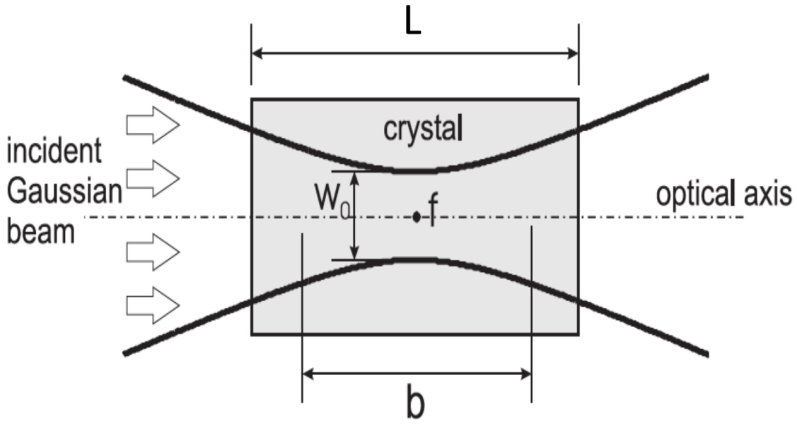

Figure 5.1: Schematic illustration of the optimal position of the fundamental beam waist (ω_o) incident at the centre of a crystal to achieve the highest frequency doubling conversion efficiency, where L is the length of the crystal, f is the focal point, and b is the confocal parameter [7].

The design of the cavity done by our group, followed the design of [137]. The crystal was similarly selected; a 20 mm long PPKTP. With 921.7 nm wavelength,

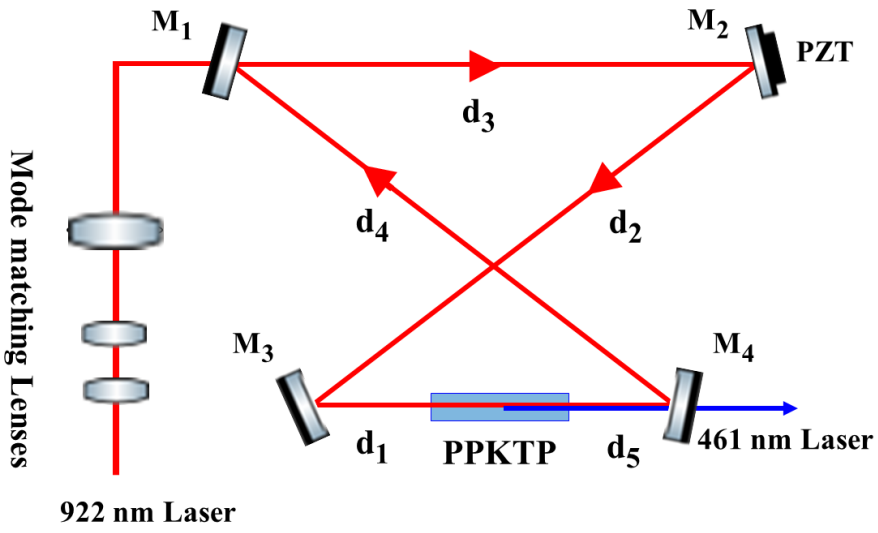

Figure 5.2: Schematic of bow-tie cavity. M_1 and M_2 are plane mirrors, M_3 and M_4 are curved mirrors with radius of curvature, R = 75 mm. The distance d_3 is 110 mm, d_2 and d_4 = 101 mm and the distance between M_1 and M_2 = 90 mm.

the refractive index of the crystal was $n_{z,921.7}$= 1.836. According to calculations in [137] the optimum value for the beam waist was $w_o^{opt} = 23.6\mu$m. The predicted second harmonic power was in the range of hundreds of milliwatts, with this value of power the PPKTP crystal suffered in terms of thermal damage due to the thermal lensing, thermal lensing a raise from the absorption of blue light as a result of the tight focusing of the beam. To avoid such a situation the beam waist was chosen to be 43μm which is nearly double the optimum value, meanwhile, no big difference in conversion efficiency was found between the two values, whereas the thermal lensing was expected to be a quarter of its value at the optimum beam waist.

Fig.5.2 show the schematic diagram for the cavity using a bow-tie configuration. There are four mirrors in the cavity. M_1 and M_2 are flat mirrors; whereas the other two (M_3 and M_4) are curved mirrors with radius curvature R=75 mm. The tilting angle of the ring resonator was set to 11^o. The M_1 mirror has partial transmission at

922 nm and anti-reflection for 461 nm, mirrors M_2 and M_3 are high reflective for 922 nm and anti-reflection for 461 nm and the M_4 mirror is totally reflective for 922 nm and transmission = 98% for 461 nm. All the mirrors have an anti-reflection coating for both 922 and 461 nm from outside them.

The cavity was aligned. The mirrors M_1 and M_2 were glued and left for 24 hours to set. Whereas, mirrors M_3 and M_4 were glued to a post mounted on a translation stage which could move in the three dimensional within the body of the cavity, and the mirrors correctly aligned before the mirrors were glued in place.

The cavity consisted of two main parts: The body of the cavity, which was made of stainless steel, and the crystal housing. The crystal housing also has small parts: a copper heatsink with eight screws, four to connect it with the cavity and four to adjust the crystal, the copper mount has a 0.3 mm groove in which to place the crystal, and a plastic thermal shield with a 3 mm slot to isolate the crystal. The crystal housing has many advantages: first, it acts to distribute the temperature uniformly throughout the crystal and prevent it from extending to the cavity. Secondly, it allowed the crystal to be moved along the x and y axes.

5.2.1 Cavity stability

To stabilize a cavity, one needs two parameters: the length of the cavity L or more specifically the round trip path length and the radius of curvature of the mirrors R. These parameters have to satisfy the stability condition $0 < g_1 g_2 \leqslant 1$ where $g_1 = 1 - (\frac{L}{R_1})$ and $g_2 = 1 - (\frac{L}{R_2})$. This relation is valid for a Fabry - Perot cavity.

However, the cavity that will be used has a bow-tie design with four mirrors, so an alternative technique is required to calculate the stability, and ray transfer matrix analysis was used. This method is also known as ABCD matrices analysis, is a form

of ray tracing. It is widely used to design and model some optical systems especially lasers. It consists of a ray transfer matrix that can be constructed to describe the optical system, and a vector representation of the light ray. By suitable matrix multiplication the light path can be found for the bow-tie cavity design. There are three different types of optical component used. Therefore six matrices will structure the **M** matrix:

$$M_c = \begin{pmatrix} 1 & L/2 \\ 0 & 1 \end{pmatrix} \quad (5.14)$$

For propagation from the centre of crystal to its end. Crystal length, L.

$$M_{nw} = \begin{pmatrix} 1 & 0 \\ 0 & n_w \end{pmatrix} \quad (5.15)$$

For changing the refractive index of the crystal at the boundary between the crystal and air n_w the refractive index for the medium.

$$T_d(d) = \begin{pmatrix} 1 & d \\ 0 & 1 \end{pmatrix} \quad (5.16)$$

For beam propagation from the end of crystal to the curved mirror, separations distance, d.

$$M_r(r) = \begin{pmatrix} 1 & 0 \\ -1/f & 1 \end{pmatrix} \quad (5.17)$$

For focusing of the beam by the curved mirror, focal length = R/2.

$$M_p = \begin{pmatrix} 1 & 0 \\ 0 & 1 \end{pmatrix} \quad (5.18)$$

For reflection by plane mirror.

$$M_{1/nw} = \begin{pmatrix} 1 & 0 \\ 0 & 1/n_w \end{pmatrix} \quad (5.19)$$

For change of refractive index from that of air to that of the crystal, nw.

The ABCD matrix can be structured by completing one cycle around the cavity starting from the center of the crystal (see Fig.5.2) :

$$\mathbf{M} = M_c \cdot M_{nw} \cdot T(d_5) \cdot M_r(r_2) \cdot T(d_4) \cdot M_p \cdot T(d_3) \cdot M_p \cdot T(d_2) \cdot M_r(r_1) \cdot M_{1/nw} \cdot M_c). \quad (5.20)$$

The **M** matrix describes the path of the beam inside the cavity. The optical cavity has two identical mirrors opposite each other, each with a radius of curvature R, and the distance separating them d. The ray tracing matrix treats them as thin lenses with focal lengths, $f = \frac{R}{2}$. This structure is known as the lens equivalent waveguide or lens equivalent duct. Light that travels down the waveguide will be refocused to stay within the waveguide or cavity, by this condition the "eigenrays" of the system can be found: the input ray vector $\begin{pmatrix} x_1 \\ \theta_1 \end{pmatrix}$ at a section of the waveguide multiplied by a real or complex constant λ equal to the output ray vector $\begin{pmatrix} x_2 \\ \theta_2 \end{pmatrix}$, this will give:

$$\mathbf{M} \begin{pmatrix} x_1 \\ \theta_1 \end{pmatrix} = \begin{pmatrix} x_2 \\ \theta_2 \end{pmatrix} = \lambda \begin{pmatrix} x_1 \\ \theta_1 \end{pmatrix}. \tag{5.21}$$

Which represents an eigenvalue equation, and can be written as:

$$[\mathbf{M} - \lambda \mathbf{I}] \begin{pmatrix} x_1 \\ \theta_1 \end{pmatrix} = 0. \tag{5.22}$$

I is the 2x2 identity matrix. By solving the eigenvalue equation of the transfer matrix $\mathbf{det}\,[\mathbf{M} - \lambda \mathbf{I}] = 0$, the stability factor g can be found:

$$g \overset{def}{=} \frac{tr(\mathbf{M})}{2}. \tag{5.23}$$

The eigenvalues are the solutions of the characteristic equation. From the quadratic formula, we find

$$\lambda = g \pm \sqrt{g^2 - 1}. \tag{5.24}$$

After N passes of the ray through the system we have:

$$\begin{pmatrix} x_n \\ \theta_n \end{pmatrix} = \lambda^n \begin{pmatrix} x_1 \\ \theta_1 \end{pmatrix}. \tag{5.25}$$

The stability of the cavity depends on the divergences of the light ray from the optical axis. If the light ray stays close to the axis and λ^n does not grow without limit, the cavity is stable.

Suppose $g^2 > 1$ that lead to a real value for both ray vectors, since $|\lambda_+\lambda_-| = 1$ one of them has to be greater than unity. That means the ray corresponding to this eigenvector cannot converge, thus stability condition is $g^2 < 1$, and λ must have an imaginary part. The parameters used in the cavity design were as follows: the radius of curvature was $R = -75$ mm, folding angle was 11^o, the distance between the plane mirrors, 110 mm, between the centres of the curved mirrors was 90 mm, and the total cavity length was 404 mm. The stability parameter found to be $|g| \simeq 0.3$ which is less than unity.

5.2.2 Cavity Operation

After the initial alignment was completed, the cavity was moved to the frequency doubling module and mounted on a Peltier cooler to stabilize its temperature. The optics used to couple the beam to the cavity was a telescope which consisted of two lenses and a third lens for focusing the beam. The beam waist was measured before the beam enter the cavity and it was found $\omega_{0||} = 390$ μm and $\omega_{0\perp} = 374$ μm. Fig.5.3 shows the beam profile before entering the cavity. The theoretical calculation from a similar design [137] predicted that the beam waist would be 43 μm in the crystal and 163 μm between the mirrors M_1 and M_2.

The Pound-Drever-Hall (PDH) technique [138] was utilized to lock the cavity for continuous stable operation mode. A piezoelectric actuator mounted on the M_2 mirror controlled the cavity length. The current to the 922 nm diode laser is frequency modulated. The reflected beam from the cavity received by the RF photodiode then

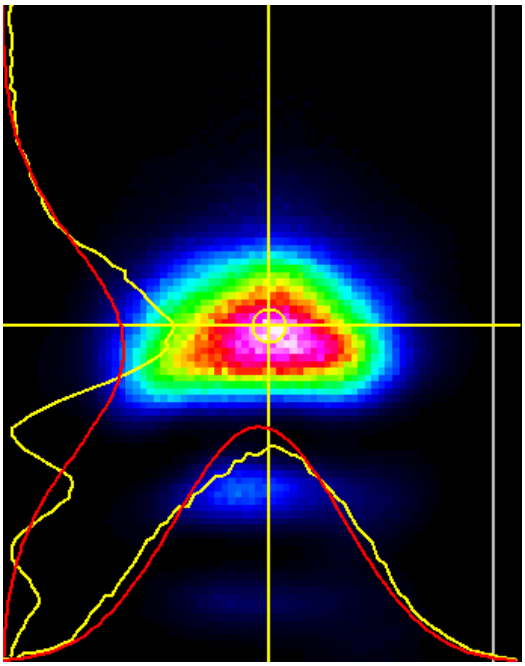

Figure 5.3: Beam profile before it entered the cavity, for 43 mW power. Although the beam profile not resembling the pure mode, the majority of power is described by the TEM00 mode with slight astigmatism. The additional side lobes are a feature of TA are unavoidable, the cavity only accepts the proportion of light that coupled to the cavity TEM00.

sent to the mixer to generate an error signal. If there is any remaining amplitude from the modulation signal it will be filtered by a low pass filter. The lockbox generates the servo signal from the error signal which will be amplified by the high voltage piezoelectric transducer. The amplified signal sent to piezoelectric will correct any change in the signal phase. The feedback setup for locking the cavity is illustrated in Fig.5.4.

The free spectral range of the cavity (FSR) depends on the length of the round trip, d, As the total length of the cavity was 404 mm, so the FSR :

$$FSR = \frac{c}{d}. \tag{5.26}$$

Where c is the speed of light in air. Thus $FSR = 742$ MHz, but this value does not take into account the crystal, when the crystal is installed within the cavity, Eq. 5.27

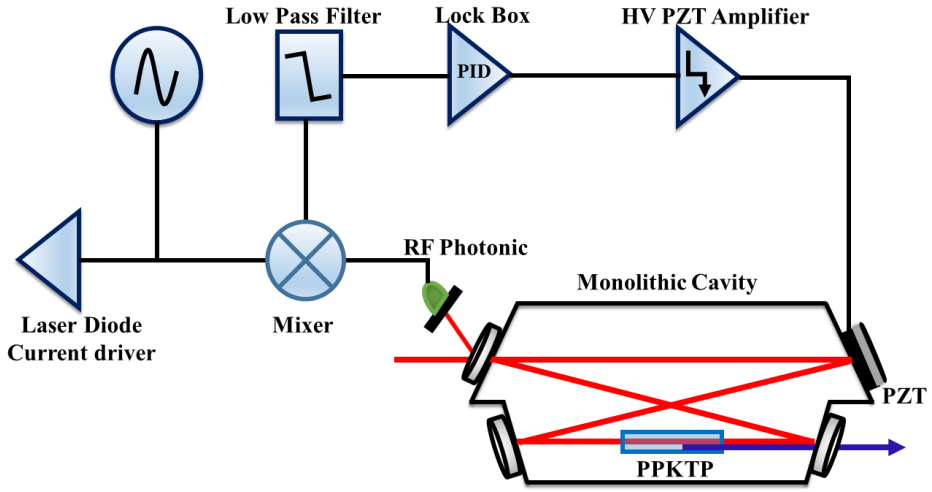

Figure 5.4: The electronic setup to lock the cavity using the PDH technique. The feedback loop consisted of a frequency modulator, RF photodiode to picked up the signal, mixer to generate an error signal, low pass filter, lockbox, HV piezoelectric amplifier, and a piezoelectric transducer.

becomes:

$$FSR = \frac{c}{d + (n_{ppktp} - 1) \cdot L}. \tag{5.27}$$

Where n_{ppktp} is the refractive index of the PPKTP crystal in the direction of propagation, which is $n_{ppktp,z,922} = 1.836$, L is the length of the crystal L=20 mm, with this included the resulting $FSR = 713$ MHz.

The finesse of the cavity can be expressed in terms of free spectral range over the full width of half maximum of the bandwidth of its resonance, and this does not depend on the cavity length. Finesse can calculate by using the expression [139] :

$$F = \frac{\pi}{2arcsin(\frac{1-\sqrt{\rho}}{2\sqrt[4]{\rho}})} \approx \frac{\pi}{1-\sqrt{\rho}} \approx \frac{2\pi}{1-\rho}. \tag{5.28}$$

Where ρ is the fraction of circulating power remaining after one round trip, that means $1-\rho$ was dissipated if no light entered the cavity. The transmission of the M_2 mirror was measured $\simeq 14 \pm 0.5\%$ and if we suppose there are no other losses from other mirrors, the finesse is, $F = 43$.

Through the operation of the cavity, we reported up to 300 mW of 461 nm blue laser second harmonic generation from a 1 W, 922 nm laser, which correspond to 30 % system efficiency as can be seen in Fig. 5.5 (a). The conversion efficiency of the input power including the power that is not mode match to the cavity was about 5%, see Fig. 5.5 (b). This value of conversion efficiency was lower than that typically achieved in [137, 140]. The reasons for that is because only $40\% - 50\%$ of the input beam is mode matched with the cavity mode see Fig. 5.3, caused by the lack of an optical component to shape the beam since there was not enough space available in the frequency doubling laser module.

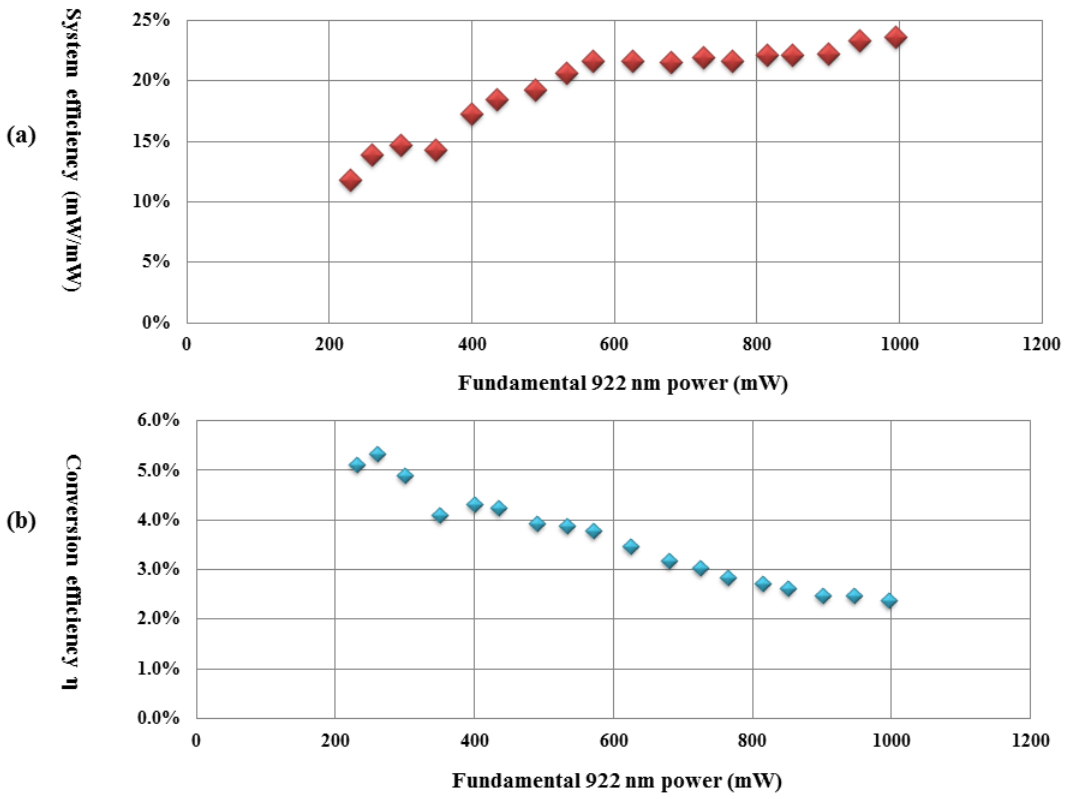

Figure 5.5: (a) The relation between the system efficiency ($\frac{P_{2\omega}}{P_{\omega}}$) and the fundamental power that enter the cavity. (b) The SHG conversion efficiency ($\eta = \frac{P_{2\omega}}{P_{\omega}^2}$) for non mode matching fundamental power.

The other reason comes from thermal effects which arise from the pre-Tapered Amplifier (TA) current, when it fluctuates and causes a drift in the input power and noise this affects the locking of the cavity. Fig.5.6 (a) shows the relation between the fundamental power that enter the cavity and the achieved 461 nm laser power.

The power in the second harmonic is highly sensitive to the temperature of the crystal. Adjusting the crystal temperature changes the phase matching and that can lead to an increase or decrease the output power depending on how close temperature is to the phase matching. The temperature of the crystal was changed from 27 °C to 28.825 °C for constant power of 2.8 A from the TA which is equal to 1 W of 922 nm of input power. The optimum temperature in such operational conditions was found to be 28 °C, which is in a good agreement with the same type of crystal used elsewhere; i.e., 28.5 °C in [137]. Fig.5.6 (b) shows the 461 nm power as a function of the crystal temperature. The difference between the output power at the optimum temperature and the lower output power than what we have reported because the measurements were taken under non-optimized operation of the system, due to two reasons: first, the system design made it hard to realign the mirrors. Second, the thermal effect from the pre -TA that led to drifting of the fundamental power over time. The result produced did give us a better understanding about the behavior of the system, and we were able to work to optimize it. However, the available power was enough for the experiment.

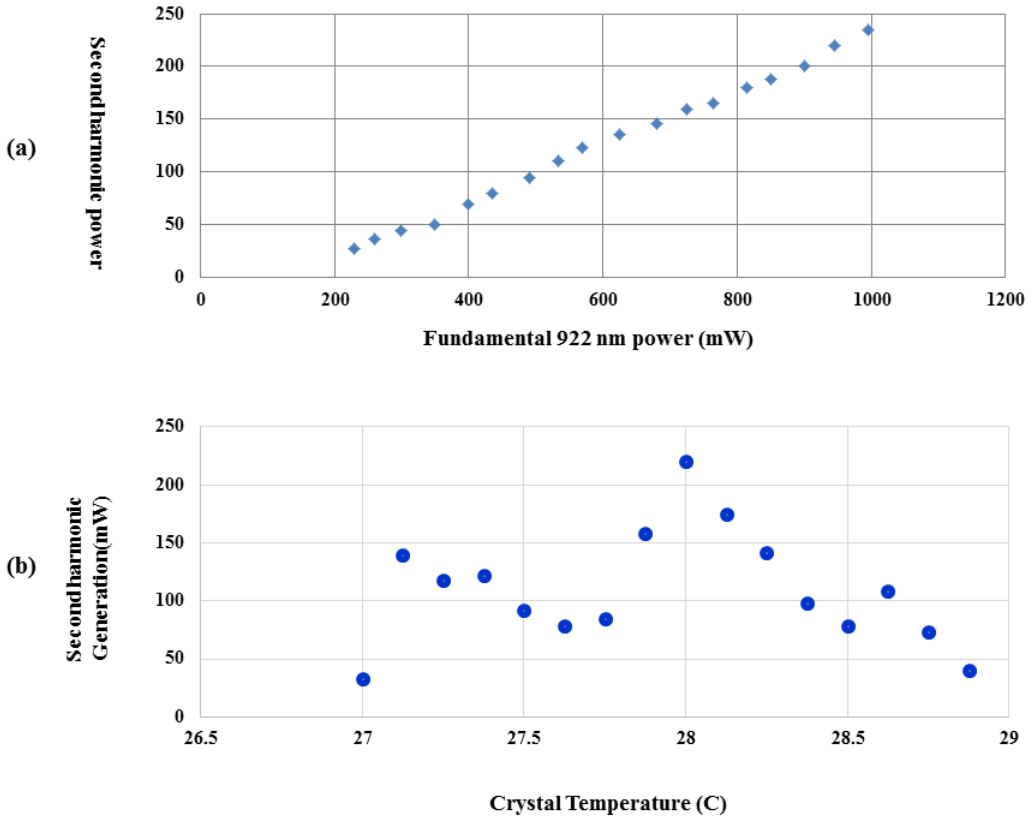

Figure 5.6: (a) The relation between the achievable second harmonic blue laser with non mode matching fundamental 922 nm laser. (b) The relation between the crystal temperature and the power of the second harmonic, for constant input power of 1 W.

Chapter 6

Conclusions and Outlook

Conclusions

This thesis aimed to build an experimental apparatus which could be used to slow, cool, and trap the strontium atoms constituting the heart of an optical lattice clock. To meet this objective, I designed and built a vacuum system.

An atomic oven has been used instead of a dispenser due to its long life and the high flux of the collimated atomic beam. By utilizing the differential pumping technique, the pressure in the magneto-optical trap (MOT) chamber could be maintained at ultra-low levels ($\approx 4 \times 10^{-11}$) mbar, which is necessary to obtain the necessary efficiency of the laser cooling and atom trapping.

This vacuum system comprised a new type of Zeeman slower based on spherical permanent magnets. I describe here the design development, building and integrating this device into vacuum apparatus for the first time. This slower has proven to work effectively: up to $6{\times}10^8$ strontium atoms were captured and trapped at the first stage cooling with using about 30 mW of 461 nm laser light. The Zeeman slower is compact (15 cm in length), and its magnetic field can be tuned by increasing or

decreasing the number of spherical permanent magnets. Moreover, its design makes the slower easy to assemble, cost-effective, and independent of a power supply or water cooling. These features make this type of Zeeman slower suitable for portable systems, in particular for space-born optical atomic clocks. Further, the development of this kind of Zeeman slower included a software code to simulate the profile of the magnetic field and resulting final velocity of the slowed atoms when at the center of the magneto-optical trap.

The importance of a Zeeman slower for optical lattice clocks becomes apparent when considering a fundamental limit to the performance of all optical atomic clocks. This limit is the quantum projection noise (QPN) that exist even when the oscillator frequency (ν) is equal to the atomic resonance frequency (ν_o).

One approach to reducing this noise is to increase the number of atoms that can be trapped in an optical lattice so that the signal to noise ratio increases. This increase in the number of atoms reduces the time for averaging the data needed to stabilize the performance of the optical clock.

I also built a monolithic frequency doubling cavity during the first year of my Ph.D. This cavity could produce, up to 300 mW of 461 nm laser light directly out of the cavity, which provides sufficient power for cooling and trapping the strontium atoms.

Outlook

Recently, the second stage cooling, the "red MOT" at 689 nm, for the strontium atoms, was realized in the vacuum system described in this thesis. Even in this colder stage, the strontium atoms were still subject to a large Doppler shift in the kHz range. Confining the atoms in a tight trap by means of an optical lattice will reduce the Doppler shift, allowing precision access to the natural frequency of the clock transition in the strontium atoms. Thus, the next step towards a strontium optical lattice clock is to transfer the strontium atoms from the "red MOT" to the optical lattice for interrogation by an ultra-stable "clock laser".

Possible improvements for the Zeeman slower

This type of Zeeman slower is designed to be self-assembled, with no need for external support to fix the permanent magnetic dipoles in position, to generate the required magnetic field. The resistance of the slower to physical deformation is not very high, and any damage to the slower could lead to distorting the profile of the magnetic field and hence reducing its efficiency. For laboratory-based experiments, this configuration has proven to work well. For a portable system, it is essential to prevent the slower from being damaged. That can be achieved in two ways: either using glue to stick the permanent magnetic dipoles in place or produce a protective case to contain the entire slower which will keep the dipoles in position. The second option could be more practical as it gives the possibility of realigning the dipoles if that is needed. Figure 6.1 shows a proposed design for the Zeeman slower protective case that can be "printed" using a suitable 3D printer.

Another possible factor for improving the slower is to revisit the shielding. As

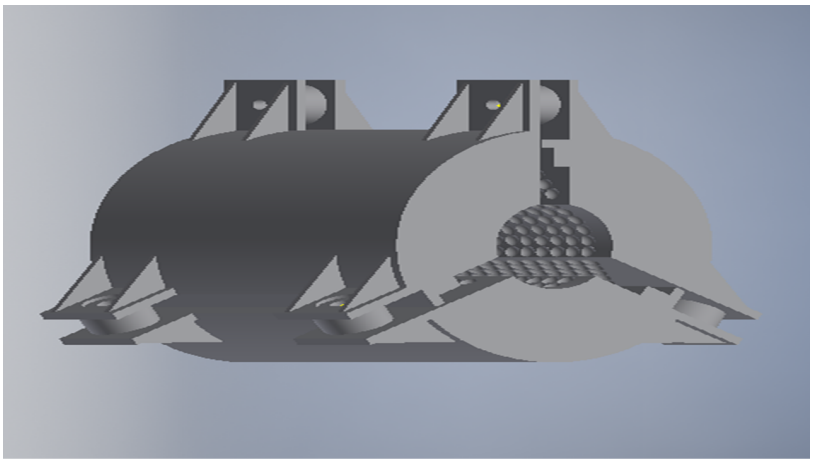

Figure 6.1: CAD drawing showing the proposed design for a protective case for the Zeeman slower to hold the permanent magnets in position.

explained previously (see Section 4.6.1) atoms with an initial speed less than 170 m/s will not be able to reach the MOT because they are slowed down in a very early stage and lost even before they enter the slower. Therefore, shielding the magnetic field of the slower could increase the number of captured atoms in the MOT as well as preventing disturbing the captured atoms in the MOT. Although cast iron was explored as a possible shield for the slower, it is worth it to explore another shielding material such as mu-metal.

Bibliography

[1] R. Hobson, *An optical lattice clock with neutral strontium*. Ph.D. thesis, University of Oxford (2016).

[2] J. Jones, *Quantum metrology with a single ytterbium ion optical clock*. Ph.D. thesis, University of Birmingham (2018).

[3] C. Foot, *Atomic Physics*. No. 978-0-19-850695-9 in Oxford Master Series in Physics. Oxford University Press, 1st Ed. (2005).

[4] A. M. Steane, M. Chowdhury and C. J. Foot, *Radiation force in the magneto-optical trap*, J. Opt. Soc. Am. B **9** (12), 2142–2158 (1992).

[5] E. M. Bridge, *Towards a strontium optical lattice clock*. Ph.D. thesis, University of Oxford (2012).

[6] M. Bober, J. Zachorowski and W. Gawlik, *Designing Zeeman slower for strontium atoms towards optical atomic clock*, arXiv:1006.1554 (2010).

[7] G. D. Boyd and D. A. Kleinman, *Parametric Interaction of Focused Gaussian Light Beams*, Journal of Applied Physics **39** (8), 3597–3639 (1968).

[8] M. Inguscio and L. Fallani, *Atomic physics: precise measurements and ultracold matter*. No. 13: 9780198525844. OUP Oxford (December 2013).

[9] H. S. Margolis, *Optical frequency standards and clocks*, Contemporary Physics **51** (1), 37–58 (2010).

[10] M. Favier, *Mercury optical lattice clock: from high-resolution spectroscopy to frequency ratio measurements*. Ph.D. thesis, Université Pierre et Marie Curie-Paris VI (2017).

[11] A. D. Ludlow, M. M. Boyd, J. Ye, E. Peik and P. O. Schmidt, *Optical atomic clocks*, Rev. Mod. Phys. **87** 637–701 (2015).

[12] J. E. Sansonetti and W. C. Martin, *Handbook of Basic Atomic Spectroscopic Data*, Journal of Physical and Chemical Reference Data **34** (4), 1559–2259 (2005).

[13] W. F. McGrew et al., *Atomic clock performance enabling geodesy below the centimetre level*, Nature **564** (7734), 87–90 (2018).

[14] T. Nicholson et al., *Systematic evaluation of an atomic clock at 2 – 1018 total uncertainty*, Nature Communications **6** 6896– (2015).

[15] M. Schioppo, *Development of a transportable strontium optical clock*. Ph.D. thesis, Universitadi Firenze (2010).

[16] *SI Brochure: The International System of Units (SI) [8th edition, 2006; updated in 2014]*. Bureau International des Poids et Mesures. `www.bipm.org/en/si/si_brochure/.`

[17] M. M. Boyd, *High Precision Spectroscopy of Strontium in anOptical Lattice: Towards a New Standard forFrequency and Time*. Ph.D. thesis, Faculty of the Graduate School of theUniversity of Colorado (2007).

[18] A. M. Lepschy, G. A. Mian and U. Viaro, *Feedback Control in AncientWater and Mechanical Clocks*, IEEE Trans. Education **vol. 35** (1), pp.3–10 ((1992)).

[19] A. A. Mills, S. Day and S. Parkes, *Mechanics of the sandglass*, European Journal of Physics **17** (3), 97–109 (1996).

[20] K. Higgins, D. Miner, C. Smith and D. Sullivan, *A Walk Through Time - The Evolution of Time Measurement through the Ages (version 1.2.1)*. National Institute of Standards and Technology, Gaithersburg, MD. (2010). `https://www.nist.gov/pml/time-and-frequency-division/popular-links/walk-through-time`.

[21] P. Arora, A. Awasthi, V. Bharath, A. Acharya, S. Yadav, A. Agarwal and A. S. Gupta, *Atomic clocks: A brief history and current status of research in India*, Pramana **82** (2), 173–183 (2014).

[22] P. Forman, *Atomichron: The Atomic Clock fromConcept to Commercial Product*, proceedings of the IEEE **73** (7), 1181–1204 (1985).

[23] D. W. Allan, *Statistics of atomic frequency standards*, Proceedings of the IEEE **54** (2), 221–230 (1966).

[24] D. B. Sullivan et al., *Primary Atomic Frequency Standards at NIST*, Journal of research of the National Institute of Standards and Technology **106** (1), 47–63 (2001).

[25] L. Essen and J. V. L. Parry, *An Atomic Standard of Frequency and Time Interval: A Caesium Resonator*, Nature **176** (4476), 280–282 (1955).

[26] M. A. Lombardi, T. P. Heavner and S. R. Jefferts, *NIST Primary Frequency Standards and the Realization of the SI Second*, The Jornal of Measurement Science **2** (4), 74–89 (2007).

[27] P. Eon, H. Myoung-Sun, K. Yong, G. Kurt, L. Sang-Bum, P. Yong, L. Won-Kyu and Y. Dai-Hyuk, *Accuracy evaluation of the KRISS-F1 fountain clock*, in *IFCS 2014 - 2014 IEEE International Frequency Control Symposium, Proceedings*. IEEE Computer Society, United States (2014).

[28] S. Beattie, B. Jian, A. Alcock, J. Bernard, M. Gertsvolf, R. Hendricks, F. Ozimek, K. Szymaniec and K. Gibble, *The NRC-FCs2 primary frequency standard at the National Research Council Canada*, in *2017 Joint Conference of the European Frequency and Time Forum and IEEE International Frequency Control Symposium, EFTF/IFC 2017 - Proceedings*, 640–641. Institute of Electrical and Electronics Engineers Inc., United States (2017).

[29] G. Santarelli, P. Laurent, P. Lemonde, A. Clairon, A. G. Mann, S. Chang, A. N. Luiten and C. Salomon, *Quantum Projection Noise in an Atomic Fountain: A High Stability Cesium Frequency Standard*, Phys. Rev. Lett. **82** 4619–4622 (1999).

[30] A. Al-Masoudi, S. Dörscher, S. Häfner, U. Sterr and C. Lisdat, *Noise and instability of an optical lattice clock*, Phys. Rev. A **92** 063814 (2015).

[31] W. M. Itano, J. C. Bergquist, J. J. Bollinger, J. M. Gilligan, D. J. Heinzen, F. L. Moore, M. G. Raizen and D. J. Wineland, *Quantum projection noise: Population fluctuations in two-level systems*, Phys. Rev. A **47** 3554–3570 (1993).

[32] S. Bilicki, *Strontium optical lattice clocks : clock comparisons for timescales and fundamental physics applications*. Theses, Université Pierre et Marie Curie - Paris VI (2017).

[33] T. Hnsch and A. Schawlow, *Cooling of Gases by Laser Radiation*, Opt. Comm. **13** (1), 68–69 (1975).

[34] L. Hollberg, C. W. Oates, G. Wilpers, C. W. Hoyt, Z. W. Barber, S. A. Diddams, W. H. Oskay and J. C. Bergquist, *Optical frequency/wavelength references*, Journal of Physics B: Atomic, Molecular and Optical Physics **38** (9), S469–S495 (2005).

[35] T. Udem, R. Holzwarth and T. W. Hnsch, *Optical frequency metrology*, Nature **416** (6877), 233–237 (2002).

[36] S. A. Diddams, D. J. Jones, J. Ye, S. T. Cundiff, J. L. Hall, J. K. Ranka, R. S. Windeler, R. Holzwarth, T. Udem and T. W. Hänsch, *Direct Link between Microwave and Optical Frequencies with a 300 THz Femtosecond Laser Comb*, Phys. Rev. Lett. **84** 5102–5105 (2000).

[37] T. Rosenband et al., *Frequency Ratio of Al+ and Hg+ Single-Ion Optical Clocks; Metrology at the 17th Decimal Place*, Science **319** (5871), 1808–1812 (2008).

[38] M. Chwalla et al., *Absolute Frequency Measurement of the* $^{40}Ca^{+}$ $4s\ ^2S_{1/2} - 3d\ ^2D_{5/2}$ *Clock Transition*, Phys. Rev. Lett. **102** 023002 (2009).

[39] K. Matsubara, H. Hachisu, Y. Li, S. Nagano, C. Locke, A. Nogami, M. Kajita, K. Hayasaka, T. Ido and M. Hosokawa, *Direct comparison of a Ca+ single-ion*

clock against a Sr lattice clock to verify the absolute frequency measurement, Opt. Express **20** (20), 22034–22041 (2012).

[40] H. S. Margolis, G. P. Barwood, G. Huang, H. A. Klein, S. N. Lea, K. Szymaniec and P. Gill, *Hertz-Level Measurement of the Optical Clock Frequency in a Single 88Sr+ Ion*, Science **306** (5700), 1355–1358 (2004).

[41] A. A. Madej, P. Dubé, Z. Zhou, J. E. Bernard and M. Gertsvolf, $^{88}Sr^{+}$ *445-THz Single-Ion Reference at the* 10^{-17} *Level via Control and Cancellation of Systematic Uncertainties and Its Measurement against the SI Second*, Phys. Rev. Lett. **109** 203002 (2012).

[42] J. von Zanthier et al., *Absolute frequency measurement of the In+ clock transition with a mode-locked laser*, Opt. Lett. **25** (23), 1729–1731 (2000).

[43] R. M. Godun, P. B. R. Nisbet-Jones, J. M. Jones, S. A. King, L. A. M. Johnson, H. S. Margolis, K. Szymaniec, S. N. Lea, K. Bongs and P. Gill, *Frequency Ratio of Two Optical Clock Transitions in* $^{171}Yb^{+}$ *and Constraints on the Time Variation of Fundamental Constants*, Phys. Rev. Lett. **113** 210801 (2014).

[44] N. Huntemann, M. Okhapkin, B. Lipphardt, S. Weyers, C. Tamm and E. Peik, *High-Accuracy Optical Clock Based on the Octupole Transition in* $^{171}Yb^{+}$, Phys. Rev. Lett. **108** 090801 (2012).

[45] N. Huntemann, C. Sanner, B. Lipphardt, C. Tamm and E. Peik, *Single-Ion Atomic Clock with* 3×10^{-18} *Systematic Uncertainty*, Phys. Rev. Lett. **116** 063001 (2016).

[46] N. Huntemann, B. Lipphardt, C. Tamm, V. Gerginov, S. Weyers and E. Peik, *Improved Limit on a Temporal Variation of m_p/m_e from Comparisons of* Yb^+ *and Cs Atomic Clocks*, Phys. Rev. Lett. **113** 210802 (2014).

[47] W. H. Oskay et al., *Single-Atom Optical Clock with High Accuracy*, Phys. Rev. Lett. **97** 020801 (2006).

[48] S. M. Brewer, J.-S. Chen, A. M. Hankin, E. R. Clements, C. W. Chou, D. J. Wineland, D. B. Hume and D. R. Leibrandt, $^{27}Al^+$ *Quantum-Logic Clock with a Systematic Uncertainty below* 10^{-18}, Phys. Rev. Lett. **123** 033201 (2019).

[49] H. Katori, M. Takamoto, V. G. Pal'chikov and V. D. Ovsiannikov, *Ultrastable Optical Clock with Neutral Atoms in an Engineered Light Shift Trap*, Phys. Rev. Lett. **91** 173005 (2003).

[50] M. Takamoto and H. Katori, *Spectroscopy of the* $^1S_0$–$^3P_0$ *Clock Transition of* ^{87}Sr *in an Optical Lattice*, Phys. Rev. Lett. **91** 223001 (2003).

[51] M. Takamoto, F. Hong, R. Higashi and H. Katori, *An optical lattice clock*, Nature **435** (7040), 321–324 (2005).

[52] R. Le Targat et al., *Experimental realization of an optical second with strontium lattice clocks*, Nature Communications **4** 2109– (2013).

[53] S. Falke et al., *A strontium lattice clock with 3 10 17 inaccuracy and its frequency*, New Journal of Physics **16** (7), 073023 (2014).

[54] I. Ushijima, M. Takamoto, M. Das, T. Ohkubo and H. Katori, *Cryogenic optical lattice clocks*, Nature Photonics **9** 185– (2015).

[55] D. Akamatsu, H. Inaba, K. Hosaka, M. Yasuda, A. Onae, T. Suzuyama, M. Amemiya and F.-L. Hong, *Spectroscopy and frequency measurement of*

the87Sr clock transition by laser linewidth transfer using an optical frequency comb, Applied Physics Express **7** (1), 012401 (2013).

[56] M. Bober et al., *Strontium optical lattice clocks for practical realization of the metre and secondary representation of the second*, Measurement Science and Technology **26** (7), 075201 (2015).

[57] N. Hinkley, J. A. Sherman, N. B. Phillips, M. Schioppo, N. D. Lemke, K. Beloy, M. Pizzocaro, C. W. Oates and A. D. Ludlow, *An Atomic Clock with 10–18 Instability*, Science **341** (6151), 1215–1218 (2013).

[58] B. J. Bloom, T. L. Nicholson, J. R. Williams, S. L. Campbell, M. Bishof, X. Zhang, W. Zhang, S. L. Bromley and J. Ye, *An optical lattice clock with accuracy and stability at the 1018 level*, Nature **506** 71– (2014).

[59] T. Kohno, M. Yasuda, K. Hosaka, H. Inaba, Y. Nakajima and F.-L. Hong, *One-Dimensional Optical Lattice Clock with a Fermionic171Yb Isotope*, Applied Physics Express **2** 072501 (2009).

[60] C. Y. Park et al., *Absolute frequency measurement of1S0(F= 1/2)–3P0(F= 1/2) transition of171Yb atoms in a one-dimensional optical lattice at KRISS*, Metrologia **50** (2), 119–128 (2013).

[61] M. Pizzocaro, P. Thoumany, B. Rauf, F. Bregolin, G. Milani, CeciliaClivati, G. A. Costanzo, F. Levi and D. Calonico, *Absolute frequency measurement of the* $^1S_0$ $^3P_0$ *transition of 171Yb*, Metrologia **54** (1), 102 (2017).

[62] H. Hachisu, K. Miyagishi, S. G. Porsev, A. Derevianko, V. D. Ovsiannikov, V. G. Pal'chikov, M. Takamoto and H. Katori, *Trapping of Neutral Mercury*

Atoms and Prospects for Optical Lattice Clocks, Phys. Rev. Lett. **100** 053001 (2008).

[63] L. Yi, S. Mejri, J. J. McFerran, Y. Le Coq and S. Bize, *Optical Lattice Trapping of* ^{199}Hg *and Determination of the Magic Wavelength for the Ultraviolet* $^1S_0 \leftrightarrow {}^3P_0$ *Clock Transition*, Phys. Rev. Lett. **106** 073005 (2011).

[64] C. Lisdat et al., *A clock network for geodesy and fundamental science*, Nature Communications **7** 12443– (2016).

[65] K. Yamanaka, N. Ohmae, I. Ushijima, M. Takamoto and H. Katori, *Frequency Ratio of* ^{199}Hg *and* ^{87}Sr *Optical Lattice Clocks beyond the SI Limit*, Phys. Rev. Lett. **114** 230801 (2015).

[66] A. D. Ludlow et al., *Sr Lattice Clock at 1 x 10–16 Fractional Uncertainty by Remote Optical Evaluation with a Ca Clock*, Science **319** (5871), 1805–1808 (2008).

[67] G. P. Barwood, G. Huang, H. A. Klein, L. A. M. Johnson, S. A. King, H. S. Margolis, K. Szymaniec and P. Gill, *Agreement between two* $^{88}Sr^+$ *optical clocks to 4 parts in* 10^{17}, Phys. Rev. A **89** 050501 (2014).

[68] C. W. Chou, D. B. Hume, J. C. J. Koelemeij, D. J. Wineland and T. Rosenband, *Frequency Comparison of Two High-Accuracy* Al^+ *Optical Clocks*, Phys. Rev. Lett. **104** 070802 (2010).

[69] R. Bajaj, S. L. Ranaweera and D. P. Agrawal, *GPS: location-tracking technology*, Computer **35** (4), 92–94 (2002).

[70] X. Li, G. Dick, M. Ge, S. Heise, J. Wickert and M. Bender, *Real-time GPS sensing of atmospheric water vapor: Precise point positioning with orbit, clock, and phase delay corrections*, Geophysical Research Letters **41** (10), 3615–3621.

[71] X. Li, G. Dick, C. Lu, M. Ge, T. Nilsson, T. Ning, J. Wickert and H. Schuh, *Multi-GNSS Meteorology: Real-Time Retrieving of Atmospheric Water Vapor From BeiDou, Galileo, GLONASS, and GPS Observations*, IEEE Transactions on Geoscience and Remote Sensing **53** (12), 6385–6393 (2015).

[72] J. Grotti et al., *Geodesy and metrology with a transportable optical clock*, Nature Physics **14** (5), 437–441 (2018).

[73] C. W. Chou, D. B. Hume, T. Rosenband and D. J. Wineland, *Optical Clocks and Relativity*, Science **329** (5999), 1630–1633 (2010).

[74] S. Blatt et al., *New limits on coupling of fundamental constants to gravity using Sr 87 optical lattice clocks*, Physical Review Letters **100** (14), 140801 (2008).

[75] C. Guerlin, P. Delva and P. Wolf, *Some fundamental physics experiments using atomic clocks and sensors*, Comptes Rendus Physique **16** (5), 565 – 575 (2015). The measurement of time / La mesure du temps.

[76] B. Altschul et al., *Quantum tests of the Einstein Equivalence Principle with the STEQUEST space mission*, Advances in Space Research **55** (1), 501 – 524 (2015).

[77] *The International System of Unit (SI)*. Bureau International des Poids et Mesures. `https://www.bipm.org/utils/common/pdf/si-brochure/SI-Brochure-9-EN.pdf`.

[78] P. Gill, *When should we change the definition of the second?*, Philosophical Transactions of the Royal Society of London A: Mathematical, Physical and Engineering Sciences **369** (1953), 4109–4130 (2011).

[79] C. Cohen-Tannoudji, *Atoms in Electromagnetic Fields*, vol. 3 of *World Scientific Series on Atomic, Molecular and Optical Physics:*, ch. Atomic Motion in Laser Light, 405–481. World Scientific, 2nd edition Ed. (2004).

[80] S. Stenholm, *The semiclassical theory of laser cooling*, Rev. Mod. Phys. **58** 699–739 (1986).

[81] J. V. Prodan and W. D. Phillips, *Chirping the lightfantastic? Recent NBS atom cooling experiments*, Progress in Quantum Electronics **8** (3), 231 – 235 (1984).

[82] W. D. Phillips and H. Metcalf, *Laser Deceleration of an Atomic Beam*, Phys. Rev. Lett. **48** 596–599 (1982).

[83] H. J. Metcalf and P. Van der Straten, *Laser cooling and trapping*. No. 978-0-387-98728-6 in 0938-037X. Springer, New York, NY (1999).

[84] P. D. Lett, W. D. Phillips, S. L. Rolston, C. E. Tanner, R. N. Watts and C. I. Westbrook, *Optical molasses*, J. Opt. Soc. Am. B **6** (11), 2084–2107 (1989).

[85] S. Chu, L. Hollberg, J. E. Bjorkholm, A. Cable and A. Ashkin, *Three-dimensional viscous confinement and cooling of atoms by resonance radiation pressure*, Physical Review Letters **55** (1), 48 (1985).

[86] J. Dalibard and C. Cohen-Tannoudji, *Laser cooling below the Doppler limit by polarization gradients: simple theoretical models*, J. Opt. Soc. Am. B **6** (11), 2023–2045 (1989).

[87] P. J. Ungar, D. S. Weiss, E. Riis and S. Chu, *Optical molasses and multilevel atoms: theory*, J. Opt. Soc. Am. B **6** (11), 2058–2071 (1989).

[88] D. S. Weiss, E. Riis, Y. Shevy, P. J. Ungar and S. Chu, *Optical molasses and multilevel atoms: experiment*, J. Opt. Soc. Am. B **6** (11), 2072–2083 (1989).

[89] Y. Castin, H. Wallis and J. Dalibard, *Limit of Doppler cooling*, J. Opt. Soc. Am. B **6** (11), 2046–2057 (1989).

[90] M. Kasevich and S. Chu, *Laser cooling below a photon recoil with three-level atoms*, Phys. Rev. Lett. **69** 1741–1744 (1992).

[91] A. L. Migdall, J. V. Prodan, W. D. Phillips, T. H. Bergeman and H. J. Metcalf, *First Observation of Magnetically Trapped Neutral Atoms*, Phys. Rev. Lett. **54** 2596–2599 (1985).

[92] E. L. Raab, M. Prentiss, A. Cable, S. Chu and D. E. Pritchard, *Trapping of Neutral Sodium Atoms with Radiation Pressure*, Phys. Rev. Lett. **59** 2631–2634 (1987).

[93] S. A. Hopkins, *Laser Cooling of Rubidium Atoms in a Magneto-optical Trap.* Ph.D. thesis, Open University (1996).

[94] A. P. Kulosa et al., *Towards a Mg Lattice Clock: Observation of the* $^1S_0{-}^3P_0$ *Transition and Determination of the Magic Wavelength*, Phys. Rev. Lett. **115** 240801 (2015).

[95] J. Friebe et al., *Remote frequency measurement of the 1 S 03 P 1 transition in laser-cooled 24 Mg*, New Journal of Physics **13** (12), 125010 (2011).

[96] U. Sterr, C. Degenhardt, H. Stoehr, C. Lisdat, H. Schnatz, J. Helmcke, F. Riehle, G. Wilpers, C. Oates and L. Hollberg, *The optical calcium frequency*

standards of PTB and NIST, Comptes Rendus Physique **5** (8), 845 – 855 (2004). Fundamental metrology.

[97] C. Grebing, A. Al-Masoudi, S. Dörscher, S. Häfner, V. Gerginov, S. Weyers, B. Lipphardt, F. Riehle, U. Sterr and C. Lisdat, *Realization of a timescale with an accurate optical lattice clock*, Optica **3** (6), 563–569 (2016).

[98] Z. W. Barber, C. W. Hoyt, C. W. Oates, L. Hollberg, A. V. Taichenachev and V. I. Yudin, *Direct Excitation of the Forbidden Clock Transition in Neutral* ^{174}Yb *Atoms Confined to an Optical Lattice*, Phys. Rev. Lett. **96** 083002 (2006).

[99] A. D. Ludlow, N. D. Lemke, J. A. Sherman, C. W. Oates, G. Quéméner, J. von Stecher and A. M. Rey, *Cold-collision-shift cancellation and inelastic scattering in a Yb optical lattice clock*, Phys. Rev. A **84** 052724 (2011).

[100] L. D. Sarlo, M. Favier, R. Tyumenev and S. Bize, *A mercury optical lattice clock at LNE-SYRTE*, Journal of Physics: Conference Series **723** (1), 012017 (2016).

[101] J. A. Neuman, P. Wang and A. Gallagher, *Robust high temperature sapphire cell for metal vapors.*, Review of Scientific Instruments **66** (4), 2021 – 2013 (1995).

[102] F. Sorrentino, G. Ferrari, N. Poli, R. Drullinger and G. M. Tino, *Laser cooling and trapping of atomic strontium for ultracold atoms physics, high-precision spectroscopy and quantum sensors*, Modern Physics Letters B **20** (21), 1287–1320 (2006).

[103] A. V. Taichenachev, V. I. Yudin, C. W. Oates, C. W. Hoyt, Z. W. Barber and L. Hollberg, *Magnetic Field-Induced Spectroscopy of Forbidden Optical Transitions with Application to Lattice-Based Optical Atomic Clocks*, Phys. Rev. Lett. **96** 083001 (2006).

[104] S. Johnson, *Narrow Linewidth Lasers for usewith Neutral Strontium as aFrequency Standard*. Ph.D. thesis, University of Birmingham (2013).

[105] D. wierad et al., *Ultra-stable clock laser system development towards space applications*, Scientific Reports **6** 33973– (2016).

[106] P. G. Mickelson, Y. N. M. de Escobar, P. Anzel, B. J. DeSalvo, S. B. Nagel, A. J. Traverso, M. Yan and T. C. Killian, *Repumping and spectroscopy of laser-cooled Sr atoms using the (5s5p) 3 P 2 (5s4d) 3 D 2 transition*, Journal of Physics B: Atomic, Molecular and Optical Physics **42** (23), 235001 (2009).

[107] T. Mukaiyama, H. Katori, T. Ido, Y. Li and M. Kuwata-Gonokami, *Recoil-Limited Laser Cooling of* ^{87}Sr *Atoms near the Fermi Temperature*, Phys. Rev. Lett. **90** 113002 (2003).

[108] T. Legero, J. S. R. V. Winfred, F. Riehle and U. Sterr, *Ultracold 88Sr atoms for an optical lattice clock*, in *2007 IEEE International Frequency Control Symposium Joint with the 21st European Frequency and Time Forum*, 119–122 (2007).

[109] M. Chalony, A. Kastberg, B. Klappauf and D. Wilkowski, *Doppler Cooling to the Quantum Limit*, Phys. Rev. Lett. **107** 243002 (2011).

[110] Q. Wang, B.-K. Lin, Y. Zhao, Y. Li, S.-K. Wang, M.-M. Wang, E.-J. Zang, T.-C. Li and Z.-J. Fang, *Magneto-Optical Trapping of88Sr atoms with 689 nm Laser*, Chinese Physics Letters **28** (3), 033201 (2011).

[111] K. R. Vogel, T. P. Dinneen, A. Gallagher and J. L. Hall, *Narrow-line Doppler cooling of strontium to the recoil limit*, IEEE Transactions on Instrumentation and Measurement **48** (2), 618–621 (1999).

[112] E. M. Bridge, J. Millen, C. S. Adams and M. P. A. Jones, *A vapor cell based on dispensers for laser spectroscopy.*, The Review of scientific instruments **80** **1** 013101 (2009).

[113] I. R. Hill, *Development of an Apparatus for a Strontium Optical Lattice Optical Frequency Standard*. Ph.D. thesis, Imperial College London (2012).

[114] *Alfavakuo.eu.Alvatec source datasheet*, (2016). `https://alfavakuo.eu/products/mvs/dimensions/`.

[115] M. Schioppo, N. Poli, M. Prevedelli, S. Falke, C. Lisdat, U. Sterr and G. M. Tino, *A compact and efficient strontium oven for laser-cooling experiments*, Review of Scientific Instruments **83** (10), 103101 (2012).

[116] V. G. Paĺchikov, Y. S. Domnin and A. V. Novoselov, *Black-body radiation effects and light shifts in atomic frequency standards*, Journal of Optics B: Quantum and Semiclassical Optics **5** (2), S131–S135 (2003).

[117] L. L. Smith, *A transportable strontium optical lattice clock towards space*. Ph.D. thesis, University of Birmingham (2016).

[118] *Working with turbo pumps - Introduction to high and ultrahigh vacuum production.*. Pfeiffer vacuum.
`http://www.pfeiffer-vacuum.com/know-how/container.action`.

[119] B. O. Kock, *Magneto-Optical Trapping of Strontium for use as a Mobile Frequency Reference*. Ph.D. thesis, University of Birmingham (2013).

[120] H. Katori, T. Ido, Y. Isoya and M. Kuwata-Gonokami, *Magneto-Optical Trapping and Cooling of Strontium Atoms down to the Photon Recoil Temperature*, Phys. Rev. Lett. **82** 1116–1119 (1999).

[121] T. H. Loftus, T. Ido, M. M. Boyd, A. D. Ludlow and J. Ye, *Narrow line cooling and momentum-space crystals*, Phys. Rev. A **70** 063413 (2004).

[122] I. R. Hill, Y. B. Ovchinnikov, E. M. Bridge, E. A. Curtis and P. Gill, *Zeeman slowers for strontium based on permanent magnets*, Journal of Physics B: Atomic, Molecular and Optical Physics **47** (7), 075006 (2014).

[123] N. Ramsey, *Molecular beams*, vol. 20. Oxford University Press (1956).

[124] P. Cheiney, O. Carraz, D. Bartoszek-Bober, S. Faure, F. Vermersch, C. M. Fabre, G. L. Gattobigio, T. Lahaye, D. Gury-Odelin and R. Mathevet, *A Zeeman slower design with permanent magnets in a Halbach configuration*, Review of Scientific Instruments **82** (6), 063115 (2011).

[125] Y. B. Ovchinnikov, *A Zeeman slower based on magnetic dipoles*, Optics Communications **276** (2), 261 – 267 (2007).

[126] Y. B. Ovchinnikov, *Longitudinal Zeeman slowers based on permanent magnetic dipoles*, Optics Communications **285** (6), 1175 – 1180 (2012).

[127] V. Lebedev and D. M. Weld, *Self-assembled Zeeman slower based on spherical permanent magnets*, Journal of Physics B: Atomic, Molecular and Optical Physics **47** (15), 155003 (2014).

[128] G. Voulazeris, *Portable atom interferometry: investigation on magnetic shielding techniques for compact quantum sensors.* Ph.D. thesis, University of Birmingham (2018).

[129] E. R. Eliel, W. Hogervorst, T. Olsson and L. R. Pendrill, *High resolution laser spectroscopy of low-lyingp-states in Sr I and Ba I*, Zeitschrift fr Physik A Atoms and Nuclei **311** (1), 1–6 (1983).

[130] K. Jooya, N. Musterer, K. W. Madison and J. L. Booth, *Photon-scattering-rate measurement of atoms in a magneto-optical trap*, Phys. Rev. A **88** 063401 (2013).

[131] W. He, *Towards Miniaturized StrontiumOptical Lattice Clock.* Ph.D. thesis, University of Birmingham (2017).

[132] R. W. Boyd, *Nonlinear optics.* No. 978-0-12-121682-5. Academic press, second Ed. (2003).

[133] G. He and S. Liu, *Physics of Nonlinear Optics.* No. 978-981-02-3319–8. World Scientific (1999).

[134] M. Falkenau, *Chromium atoms in a deep optical dipole trap.* Ph.D. thesis, Universitat Stuttgart (2008).

[135] P. E. Powers, *Fundamentals of Nonlinear Optics.* No. 9781420093513. CRC Press, Taylor and FrancisGroup, second Ed. (2011).

[136] S. Hannig, J. Mielke, J. A. Fenske, M. Misera, N. Beev, C. Ospelkaus and P. O. Schmidt, *A highly stable monolithic enhancement cavity for second harmonic generation in the ultraviolet*, Review of Scientific Instruments **89** (1), 013106 (2018).

[137] R. Le Targat, J.-J. Zondy and P. Lemonde, *75%-Efficiency blue generation from an intracavity PPKTP frequency doubler*, Optics Communications **247** (4), 471–481 (2005).

[138] E. D. Black, *An introduction to Pound–Drever–Hall laser frequency stabilization*, American Journal of Physics **69** (1), 79–87 (2001).

[139] R. Paschotta, *article on 'finesse'*, (2008). `https://www.rp-photonics.com/encyclopedia.html`.

[140] Y. Li, Y. Zhao, Y. Peng, T. Yang, J. Cao, Z. Fang and E. Zang, *More than 200 mW blue light source from an integrative ring cavity*, in *Precision Electromagnetic Measurements Digest, 2008. CPEM 2008. Conference on*, 190–191 (2008).